Novel magnetic and electronic properties of kagomé-lattice cobalt-shandites

Mohamed Abdelkareem Ali Ahmed Kassem

2016

Novel magnetic and electronic properties of kagomé-lattice cobalt-shandites

A dissertation submitted as a partial fulfillment of the degree of

Doctor of Philosophy in physics,

Kyoto University

By

Mohamed Abdelkareem Ali Ahmed Kassem

(Mohamed A. Kassem)

2016

ACKNOWLEDGEMENTS

Here I should offer my deep appreciation to whose supervision, guidance and recommendations made this thesis appears in its current form. Also I should reflect on the people who have supported and helped me throughout the period of this study.

Firstly, I would like to express my special appreciation and thanks to my supervisor **Professor Hiroyuki Nakamura**, a materials scientist who have been my tremendous mentor. Many thanks for giving me the opportunity to study in his lab among its outstanding group. His advices in research, patience in face of my impatient aspiration at the beginning, and his careful consideration of my future research continuity in my home county, all are quite appreciated. Also I would like to thank him for the continuous support and interest in a safe and comfortable life for me in- and out-side the campus.

I here also express my deep appreciation to my advisor, **Professor Yoshikazu Tabata**, a pioneer in physics whose discussions impressed me so much. Actually I am grateful for many chances starting from my accommodation in the lab close to him. I would like to thank Professor Tabata for the trust, the insightful discussion, offering valuable advice, and for his support during the whole period of the study. Especially I thank him for his patience and guidance during the writing process of manuscripts and thesis.

My sincere thanks also go to the third member in my advisory committee, **Dr. Takeshi Waki**, Assistant professor, for the warm welcome I have received, teaching about the lab facilities, freeing time whenever I wanted to consult with samples preparation and characterization, and for the friendly interaction and continuous support.

My deep thanks to **Dr. C. Michioka**, Assistant professor of Solid State Chemistry and Physics Lab of Kyoto University for the specific heat measurements, **Dr. Sasaki** and **Mr. Kazumi** from Dept. of materials science and Engineering of Kyoto University for the assistance by WDS measurements. I would like to thank the lab colleagues, **Mr. K. Itou** for his assistance in the Hall resistivity measurements, **Mr. K. Takao** for his assistance in planned NMR measurements, and other colleagues for fruitful discussions in the regular seminars and lab events. Thanks very much to our lab secretary **Mrs. Machiko Ishizuka**.

Thanks to Professor **K. Yoshimura** and **Professor A. Sakai** for critical reading of the thesis manuscript.

I acknowledge my financial support from the **Ministry of Higher Education, Egypt** during this study.

Many thanks should also be sent to **my family, wife, daughter and son** for support and happiness.

Finally, I dedicate my PhD thesis to my son “Omar” on his 4th birthday, PhD that started with his birth.

Mohamed A. Kassem

2016, Nov.

ABSTRACT

Co-based shandites $Co_3M_2S_2$ (M = Sn and/or In) are candidates of quasi-two-dimensional (Q2D) strongly correlated electron systems showing exotic magnetic and electronic properties. The interest is implied by its layered crystal structure that contains 2D-kagomé networks of magnetic Co atoms. The kagomé lattice, a corner-sharing triangular lattice, is a representative frustrated lattice where a thermodynamic stable state of the antiferromagnetic-coupled spin system is not trivially determined due to the geometric-origin competitions of spin-spin interactions. The Co-based shandites have been investigated mainly using polycrystalline samples and some interesting properties were found: the half-metallic ferromagnetic state in $Co_3Sn_2S_2$, the magnetic instability controlled by electron number in $Co_3Sn_{2-x}In_xS_2$, high thermoelectric properties of Co_3SnInS_2. However, investigations from the above-mentioned viewpoint, Q2D kagomé system, have not been carried out. For this purpose, investigations using single crystals are essential. In this work, we tried to grow single crystals of two series-compounds of Co-based shandites, $Co_3Sn_{2-x}In_xS_2$ and $Co_{3-y}Fe_ySn_2S_2$, to investigate them as the Q2D kagomé system and we found novel and exotic properties using the successfully grown single crystals, namely, (i) highly Q2D itinerant electron magnetism, (ii) emergence of a chiral spin state in the vicinity of the ferromagnetic-nonmagnetic quantum critical point (QCP), (iii) low-field anomalous phase very close to T_C, and (iv) emergence of exotic Q2D electronic state, which may be a Dirac semimetal state.

Single crystals of two series-compounds of Co-based shandites $Co_3Sn_{2-x}In_xS_2$ ($0 < x \leq 2$) and $Co_{3-y}Fe_ySn_2S_2$ ($y \leq 0.5$) were successfully grown by flux method and modified Bridgeman method. Using the flux method, sufficiently large hexagonal plate-shaped single crystals were obtained. $Co_3Sn_{2-x}In_xS_2$ single crystals were grown out of stoichiometric Sn and In self-flux, and/or Pb flux while $Co_{3-y}Fe_ySn_2S_2$ crystals were grown out of the Sn self-flux. Much larger single crystals of $Co_3Sn_{2-x}In_xS_2$ (~ 5 cm in length and 1 cm in diameter) were grown by using a modified Bridgeman method of slow cooling of vacuum-sealed polycrystalline powders in a vertical temperature-gradient furnace. The shandite structure with $R\bar{3}m$ symmetry was confirmed by powder x-ray diffraction and the crystal structure parameters were refined by the Rietveld analysis. Wavelength-dispersive x-ray spectroscopy indicated the successful growth of $Co_3Sn_{2-x}In_xS_2$ in the whole range of x and the growth of $Co_{3-y}Fe_ySn_2S_2$ up to $y = 0.5$.

Comprehensive magnetization measurements were performed using the grown single crystals of Co-based shandites. In consistence with literature, $Co_3Sn_2S_2$ exhibits a ferromagnetic transition at Curie temperature T_C ~173 K with a strong uniaxial anisotropy. The ferromagnetic order is suppressed by In- and Fe-substitutions and the ferromagnetic-nonmagnetic quantum phase transition was found at around x_c (y_c) ~ 0.8. The obtained magnetic parameters of both systems; the Curie temperature T_C, effective moment p_{eff} and spontaneous moment p_s; exhibit almost identical variations against the In- and Fe-concentrations, indicating significance of the electron count on the magnetism in the Co-based shandite. Analyses of the magnetizations based on the extended Q2D spin fluctuation theory clearly reveals a highly Q2D itinerant electron character of the magnetism in $Co_3Sn_{2-x}In_xS_2$ and $Co_{3-y}Fe_ySn_2S_2$. It is a natural consequence of the layered crystal structure of the Co-based shandites.

A chiral spin state was observed in the vicinity of the quantum critical point (QCP) of $Co_3Sn_{2-x}In_xS_2$ through a combined work of the magnetization and magneto-transport measurements. A distinct positive topological Hall effect (THE) was observed at low temperature (T < ~ 7 K) and low field (H < ~ 0.2 T) regions, indicating an emergence of the non-trivial spin state with finite uniform chirality. This chiral spin state is interpreted as a consequence of the combination of the inherent Dzyaloshinskii-Moriya (DM) interaction in the kagomé Co-network built in the shandite structure, ferromagnetic order, and in-plane spin fluctuations enhanced near the QCP.

Furthermore, an anomalous phase (A-phase) in the vicinity of T_C and at very low fields ($\lesssim$ 0.04 T) was discovered within the ferromagnetic ordered phase of $Co_3Sn_{2-x}In_xS_2$. Precise magnetization and ac susceptibility measurements at very low magnetic fields (below the saturating field of ~ 1kOe) were performed and extremely slow dynamics, its characteristic relaxation time is longer than 10 sec, was found near the phase transition temperatures/fields between the anomalous phase and ferromagnetic/paramagnetic phases. These characteristic slow dynamics are very similar to those observed in the magnetic skyrmion materials such as (Fe,Co)Si and Cu_2OSeO_3, where the 2D triangular arrangement of large-scaled objects of topologically-protected vortex-like spin texture (magnetic skyrmion) is stabilized. With considering the possible DM interaction and similarity to the known magnetic skyrmion systems, the experimental results suggest the presence of a skyrmion-like topologically protected spin texture in the A-phase of $Co_3Sn_{2-x}In_xS_2$.

Exotic electronic state in $Co_3Sn_{2-x}In_xS_2$ for $x \sim 1.0$ were also discovered by resistivity and heat capacity measurements using single crystals. The Fermi level of $Co_3Sn_{2-x}In_xS_2$ is tuned by the In-substitution and it changes from the electron-band to hole band at around $x \sim 1.0$. An exotic semimetallic behavior, a logarithmic divergence of the resistivity against temperature, was observed in a very narrow x-region at $x \sim 1.0$, accompanying an anomalously enhanced anisotropy of the *ab*-plane- and *c*-axis-resistivities. Simultaneously, an absence of the T-linear term of the specific heat, and a strongly enhanced T^3-term instead, were found. All indicate an unconventional electronic state with anomalously small Fermi surface very close to $x \sim 1.0$. With considering the enhanced T^3-term of the specific heat, that is a T^3-term of electronic specific heat, a linear dispersive electron state and an emergent Dirac electron state in this layered kagomé system is suggested.

Table of Contents

ACKNOWLEDGEMENTs.....i
ABSTRACT.....ii

CHAPTER 1

Introduction

1.1 Magnetism in Metals 1
1.1.1 Spin fluctuation theory 1
1.2 Physics at Low-dimensions 2
1.3 Topological Phenomena in Condensed Matter 3
1.3.1 Spin frustration and Dzyaloshnskii-Moriya interaction 3
1.3.2 Spin chirality and its related topological phenomena 5
1.3.3 Magnetic skyrmions 7
1.3.4 Topological electronic states 8
1.4 Co-based Shandites 9
1.4.1 Metal-rich chalcogenides 9
1.4.2 Shandites and Parkerites: Variations and Structural relation 10
1.4.3 Shandite structure 12
1.4.4 Known properties of Co-based shandites 14
1.5 Aim of the Present Study 18
1.6 Outline of the Present Dissertation 18

CHAPTER 2

Experimental Procedures

2.1 Outline 19
2.2 Synthetic Methods 19
2.2.1 Crystals growth by a flux method 19
2.2.2 Solid state reaction 21
2.2.3 Crystals growth by a modified Bridgeman method 22
2.3 Characterization and Measurements 23
2.3.1 Wavelength-dispersive x-ray spectroscopy 23
2.3.2 Powder X-ray Diffraction and Rietveld analysis 24
2.3.3 Laue X-ray photography 25
2.3.4 Magnetization and ac susceptibility 25
2.3.5 Longitudinal and transverse resistivities 26

2.3.6 Specific heat 27

CHAPTER 3

Crystal Growth and Structure of $Co_3Sn_{2-x}In_xS_2$ and $Co_{3-y}Fe_ySn_2S_2$

3.1 Motivations and Purpose 28
3.2 Outline 28
3.3 Results and Discussion 28
3.3.1 Crystal growth and chemical composition 28
3.3.2 Powder X-ray diffraction and crystal structure analysis 32
3.4 Conclusion 40

CHAPTER 4

Magnetic Properties I: Quasi-Two-Dimensional Magnetism in Co-based Shandites

4.1 Motivations and Purpose 41
4.2 Outline 41
4.3 Results and Discussion 41
4.3.1 Anisotropic magnetic properties 42
4.3.2 Analysis and discussion of the Q2D itinerant electron magnetism 50
4.4 Conclusion 53

CHAPTER 5

Magnetic Properties II: Topological Hall Effect in $Co_3Sn_{2-x}In_xS_2$ Ferromagnets

5.1 Motivations and Purpose 54
5.2 Outline 54
5.3 Estimation of Topological Hall Effect 54
5.4 Experimental Results 56
5.5 Analysis Results 57
5.6 Discussion 60
5.7 Conclusion 63

CHAPTER 6

Magnetic Properties III: Low-field Magnetic Phase Diagram of $Co_3Sn_2S_2$ Inferred from Magnetization and ac Susceptibility

6.1 Motivations and Purpose 64

6.2 Outline 64

6.3 Results and Discussion 64

6.3.1 Magnetization 64

6.3.2 ac susceptibility of $Co_3Sn_2S_2$ 66

6.3.3 Relaxation phenomena and frequency dependence of χ' and χ''. 68

6.3.4 Magnetic phase diagrams 72

6.4 Conclusion 74

CHAPTER 7

Transport Properties of Co-shandites: Emergent Unconventional Electronic State of $Co_3Sn_{2-x}In_xS_2$

7.1 Motivations and Purpose 75

7.2 Outline 76

7.3 Experimental Results 76

7.3.1 Electrical resistivity 76

7.3.2 Specific heat 80

7.4 Discussion 84

7.5 Conclusion 89

CHAPTER 8

Concluding Remarks

References: 92

List of Publications……..……..……99

CHAPTER 1

1 Introduction

1.1 Magnetism in Metals

As a part of the more general problem of understanding the complex electronic structure of the transition metal compounds, magnetism is a typical many-body problem that cannot be treated straightforwardly in condensed matter physics. For instance, a truly unified theory of *ferromagnetism in metals* is not established yet and when achieved, it is not likely to be a simple theory, as the experimental facts to be explained are so diverse. Instead, a long controversy between the strong-coupling approach from the *local* moment model and weak-coupling approach from the *itinerant* electron model has launched repeatedly in the field of metallic magnetism in strongly correlated *d*- and *f*-electron systems.

According to the localized moment model, the electrons responsible for the magnetism are attached to the atoms and cannot move about the crystal due to the strong electron correlation, i.e. the principal part of the magnetism is appeared as the orientational average of magnetic moments with fixed magnitudes. In the strong-coupling approach, magnetic electrons adopt itinerancy by hopping mechanism which acts as a quantum fluctuation of localized moments. On the other hand, weak-coupling approach based on the itinerant electron model, magnetism arises as a perturbation of electron correlation. The strong- and weak-coupling approaches can describe magnetism in the systems with strong and weak electron correlation. For instance, *d*-electron metals and intermetallic compounds are considered to be within the range of the weak-coupling approach. On the other hand, transition metal oxides are considered to be within the strong-coupling approach. However, the magnetism in strongly correlated *d*- and *f*-electron systems is frequently observed in a widely distributed intermediate range between the two extreme conditions where the strong- and weak-coupling approaches are appropriate.

1.1.1 Spin fluctuation theory

Here, I introduce one of the most successful theory of itinerant electron magnetism by the weak-coupling approach, so-called spin fluctuation theory.

The first theory of itinerant magnetism that associated the magnetism in metals to the splitting of the conduction electrons band was proposed by Stoner and developed by Wohlfarth and co-workers (SW)[1,2]. SW theory succeeded to derive the condition of spontaneous

magnetization appearance in a metal, i.e. the Stoner criterion, which qualitatively describes an electron-correlation mechanism of magnetic ordering in metals. However, the SW theory failed to derive the observed Curie-Weiss (CW) law satisfaction of the temperature dependence of susceptibility above the magnetic ordering temperature T_C, because of its neglect of the effects of thermal spin fluctuations.

A new theoretical development now well known as the self-consistent renormalized spin fluctuation (SCR) theory was proposed by Moriya and his co-workers. The SCR theory succeeded to reproduce the CW behavior above T_C in itinerant electron magnets by mainly emphasizing the effects of collective magnetic excitations, i.e. thermal spin fluctuations, at finite temperatures[3–6]. Takahashi developed a new coherent framework of the SCR theory by assuming the total amplitude conservation spin fluctuations (TAC) and global self-consistency of magnetization curve (GSC)[7]. Many experimental results observed in metallic magnets, such as MnSi, $ZrZn_2$, and $Y(Co_{1-x}Al_x)_2$, are well-described by Takahashi's spin fluctuation theory[8]. The spin fluctuation theory is also extended to quasi-two dimensional (Q2D) magnetic systems, which can be applied to materials with layered crystal structures. such as LaCoAsO, LaCoPO, and $(Cr_{1-x}Mn_x)_2GeC$[8,9].

1.2 Physics at Low-dimensions

Low-dimensionality is a key to enhance the effects of correlations and disorder. For instance, the Landau's Fermi liquid picture is completely broken down in correlated one-dimensional electron systems. The Landau's Fermi liquid picture is quite common and valid to describe conventional 3D metals, where fermion-like quasiparticle excitations are dominant. On the other hand, in truly one-dimensional systems, bosonic excitations, spinon and holon, dominate the low-energy excitations instead of fermion-like excitations, called as the Tomonaga-Luttinger (TL) liquid. The TL liquid picture can be extended to two-dimensional systems.

Ideal low-dimensional systems cannot be realized in real materials, nevertheless, low-dimensional characters emerge in weakly-coupled chain and layered compounds, corresponding to quasi-one-dimensional (Q1D) and quasi-two-dimensional (Q2D) systems, respectively. The strongly enhanced thermal and quantum fluctuations is an important aspect of the physics at low-dimensions that give rise to exotic phenomena[10]. For instance, The TL liquid and Peierls instability in Q1D metals[11], high temperature superconductivity in layered cuprates and iron-based superconductors[12–16], unconventional quantum-criticality in heavy fermion systems[17,18], the successive phase transitions and electronic instability in Layered

transition metal dichalcogenides[19–21] and Q2D itinerant electron magnetism in layered-structural compounds[8,9].

More ideal low dimensional systems can be realized in surfaces and interfaces between different materials. The electronic states on such surfaces and interfaces can be completely different from those inside the bulk materials and can be recognized as ideal two dimensional systems. Furthermore, mono-layered materials, such as graphene, were also substantiated, which enabled us to study novel phenomena in low dimensional systems, such as topological electronic states[22–24] The physics in low dimensional systems is in the midst of a movement right now.

1.3 Topological Phenomena in Condensed Matter

Recently, topological phenomena in condensed matters have been paid much attention from viewpoints of fundamental physics and application. In this section, I introduce several topics of topological phenomena related with my study.

1.3.1 Spin frustration and Dzyaloshinskii-Moriya interaction

Here representative mechanisms of topological phenomena emergence due to nontrivial spin textures: *spin frustration* and *Dzyaloshinskii-Moriya* (DM) interaction, are described.

In contrast to the ferromagnetic interactions that are easily satisfied by parallel alignment of the atomic moments, antiferromagnetic interactions may be not. The most common spin-spin interaction in condensed matters is a symmetric type given by a scalar product of spins, so-called Heisenberg-type exchange interaction, as $\mathcal{H}_0 = -2J_{ij}(\vec{S}_i.\vec{S}_j)$, where $\vec{S}_{i,j}$ is a spin operator at the atomic site $\vec{R}_{i,j}$. When the exchange constant J_{ij} is positive, the two spin align parallel (ferromagnetic case), whereas, they align antiparallel if J_{ij} is negative (antiferromagnetic case). In structures of odd-membered rings with antiferromagnetic coupling, it is impossible to satisfy all the antiferromagnetic interactions simultaneously. For instance, possible stable spin arrangements on a triangular are shown in Figs. 1.1(a) for $J > 0$ and $J < 0$. In the antiferromagnetic case, the direction of spins cannot be settled. This type of spin frustration is due to a geometry of site-arrangement, and thus, is called as geometric frustration. Many geometrically frustrated lattice consisting of triangular units; triangular, kagomé, fcc and pyrochlore lattices; are well known. Examples of frustrated lattices, triangular and kagomé lattices are shown in Figs. 1.1(c) and (d), respectively[25].

The frustration introduces low energy scales in comparison to the interaction energy, making the system unstable with numerous degeneracy and in general suppresses the ordering. If spins have a continuous degree of freedom, such as XY- and Heisenberg-spins, spin frustration can be avoided by forming non-collinear or non-coplanar spin textures. For instance, the stable 120-degree spin textures on a triangular is shown in Fig. 1.1(b). This spin texture has a nontrivial degree of freedom, called as *spin chirality*. The spin chirality is one of the most significant sources of topological phenomena and one of the key concepts of this study, which will be introduced in more detail in the next subsection.

The concept of frustration was initially proposed for local moment systems, however it is also significant in itinerant electron systems, and many attractive phenomena, such as heavy fermion behavior in (Y,Sc)Mn_2[26] and LiV_2O_4[27] and topological transport phenomena[28], have been discovered.

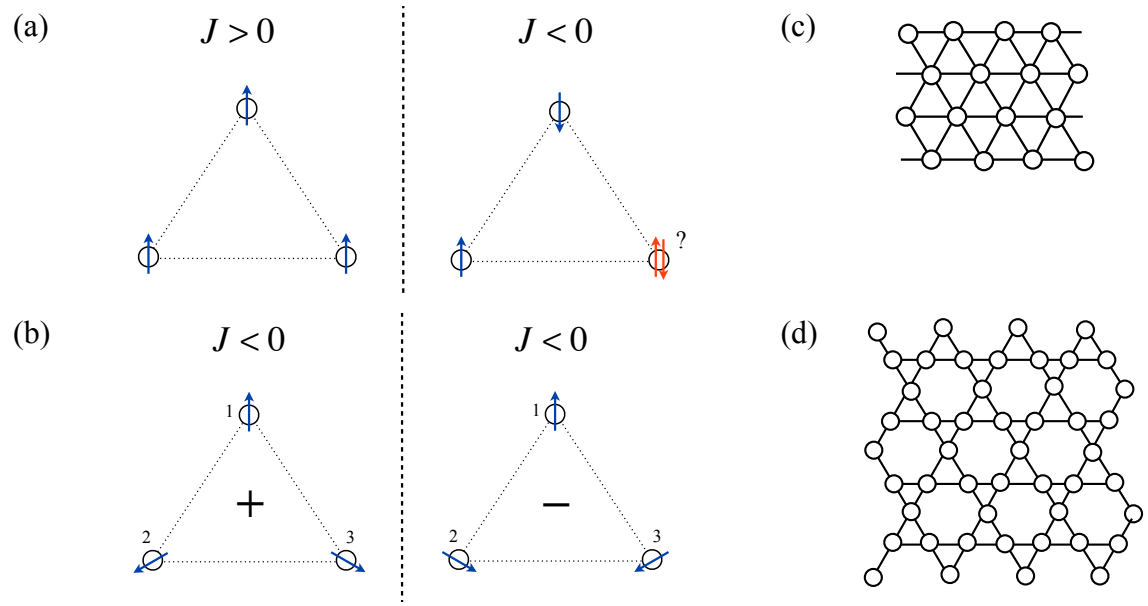

Figure 1.1: (a) Schematic illustration explaining spin frustration on a triangular lattice. (b) Stable 120-degree spin textures in the XY- or Heisenberg spins on a triangular lattice. Two (left and right) figures in (b) correspond to a degree of freedom of spin chirality.

Another possible mechanism inducing nontrivial spin textures is the antisymmetric Dzyaloshinskii-Moriya (DM) interaction[29,30]. The antisymmetric DM exchange between two neighboring magnetic spins, $\vec{S}_i$ and $\vec{S}_j$ has the form $\mathcal{H}_{DM} = -\boldsymbol{D}_{ij}.(\vec{S}_i \times \vec{S}_j)$, where the DM vector $\boldsymbol{D}_{ij}$ is a vector of the axis that is determined by the symmetry of the crystal. Because the DM interaction energy changes its sign by the inversion operation between sites $\vec{R}_i$ and $\vec{R}_j$, it is finite when the inversion symmetry at the center of magnetic atom sites is lack. In non-

centrosymmetric crystals, such as chiral and polar crystal structures[31,32], the DM interaction can be uniform. In some other cases, the DM interaction exits but changes its magnitude and sign site by site.

The DM interaction favors a spin arrangement where spins are aligned perpendicularly to each other (see Fig. 1.2(a)). Consequently, non-collinear spin textures with finite spin chirality are appeared due to competition between the asymmetric DM interaction and symmetric Heisenberg-type interaction. The ferromagnetic spin arrangement is modified by the DM interaction to a long-periodic helical spin texture, as shown in Fig. 1.2(b). The antiferromagnetic one is, in a similar manner, modified to a weak-ferromagnetic (canting antiferromagnetic) one (see Fig. 1.2(c)). The canting angle θ is given by $\theta = \tan^{-1}(D/J)$. Furthermore, a topologically-protected spin texture, called as magnetic skyrmion, can be realized in chiral and polar crystals, which is paid much attention in the recent ten years.

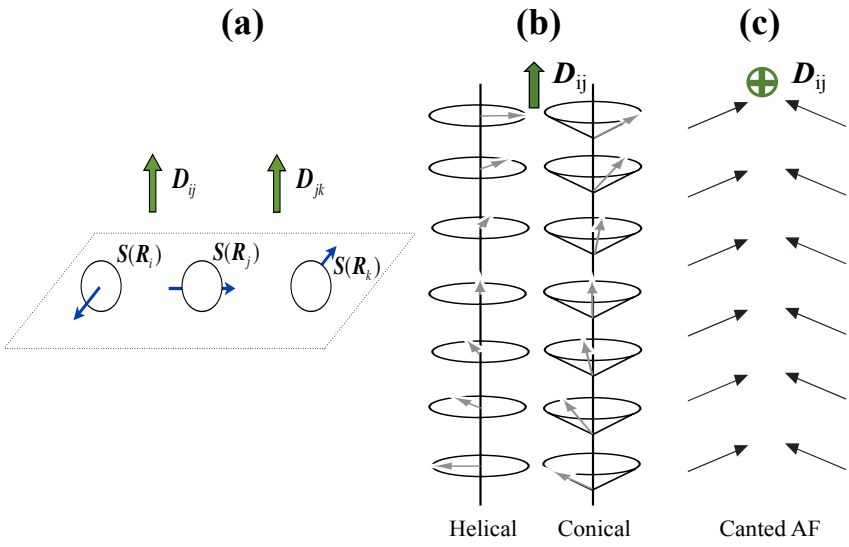

Figure 1.2: (a) Schematic illustration of the antisymmetric DM exchange. (b) and (c) show the spiral spin texture and canting antiferromagnetic spin texture resulted from a competing DM interaction with symmetric ferromagnetic and antiferromagnetic exchanges, respectively.

1.3.2 Spin chirality and its related topological phenomena

Chirality, a quantity being finite when the reflection symmetry is broken, is a very common property in nature, for instance, in chiral molecules (optical isomers). In magnets, "spin chirality", defined as $\chi_{ijk} = \boldsymbol{S}_i \cdot (\boldsymbol{S}_j \times \boldsymbol{S}_k)$ (scalar chirality) or $\boldsymbol{\chi}_{ij} = \boldsymbol{S}_j \times \boldsymbol{S}_k$ (vector chirality), is emergent when non-coplanar and/or non-collinear spin textures are realized. Recently, many attractive phenomena induced by the emergence of spin chirality, such as topological Hall effect[33] and multiferroicity[34], have been extensively studied.

Non-collinear and/or non-coplanar spin textures with finite spin chiralities can be stabilized by, for instance, spin frustration effects and DM interaction as described in the previous subsection. In case of geometric frustrated spin systems with only symmetric exchange interactions, the spin textures with finite chiralities appear as spontaneous chiral-symmetry-breaking (chiral phase transitions), since the systems themselves are chiral-symmetric[35–39]. On the other hand, in non-centrosymmetric crystals, the chiral symmetry is trivially broken due to the crystal symmetry, that is, the direction of the DM interaction when the magnetic orders with non-collinear and/or non-coplaner spin textures are emergent[40]. As consequences, muli- and mono-chiral-domain systems take place with and without the DM interaction, respectively.

One of the most striking phenomena related with spin chirality is the chirality-driven *topological Hall effect* (THE). When a local scalar chirality χ_{ijk} is finite, a conduction electron captures a finite Berry phase proportional to χ_{ijk} by circulating through the i-, j-, and k-sites. This represents that the scalar chirality plays a role of fictitious magnetic field, as schematically illustrated in Figure 1.3, for conduction electrons and modify their path "topologically". This fictitious magnetic field causes a Hall effect without (real) magnetic field and magnetization, so-called the topological Hall effect. However, the topological Hall effect vanishes in most cases because the Berry phase is canceled out by summation throughout the lattice. In some special cases, magnets with the kagomé or pyrochlore lattice or random magnets such as spin glasses, the Berry phase, and consequently the topological Hall effect, is expected to survive.

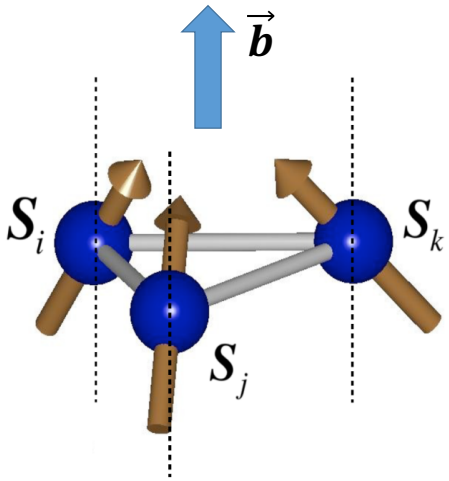

Figure 1.3: Schematic view of the scalar spin chirality and the corresponding fictitious magnetic field $\vec{b}$ in chiral ordered system[33,41].

Experimentally, the topological Hall effect was observed in some pyrochlore magnets[42,43] and spin glasses[44,45]. Especially, the pyrochlore magnet $Pr_2Ir_2O_7$ shows a spontaneous Hall effect without any magnetic orders, indicating presence of a purely chiral-ordered state[43].

1.3.3 Magnetic skyrmions

Recently, objects of topological nature consisting of non-trivially-arranged spins, magnetic skyrmions, have been extensively investigated in condensed matters. Magnetic skyrmion is a topologically-protected defect in a conventional ferromagnetic spin arrangement and is a particle-like nanometric vortex spin texture. In one single skyrmion, the constituting spins cover all directions in 3D space. Hence, the skyrmion has a topological charge, a topological skyrmion number, $N_S = 1$. Since the skyrmion is protected topologically, it can be extremely stable against extrinsic defect, for instance crystallographic defects, and have no intrinsic pinning effect. New generation of low power-consumption magnetic memory devices using skyrmions as information carriers is highly promoted[46].

In non-centrosymmetric chiral magnets such as MnSi[47], $Fe_{1-x}Co_xSi$[48], FeGe[49], Cu_2OSeO_3[50] and β-Mn-type Co-Zn-Mn[51], the magnetic skyrmion lattice phase, where the magnetic skyrmions spontaneously form a 2D triangular lattice, were observed. In these systems, the antisymmetric DM interaction destabilizes the collinear ferromagnetic order and induces helical spin textures. The skyrmion lattice emerges as a multi-q state of the helical spin texture, which is categorized into two types in terms of relationship between the spin-rotating plane and the helical propagation vector: the Bloch- and Néel-types. In the former-type skyrmion lattice, the spin-rotating plane is perpendicular to the helical propagation vector. On the other hand, the helical propagation vector is within the spin-rotating plane in the Néel-type one. The type of a skyrmion, that is helical spin texture, is determined by the crystal symmetry: the Bloch- and Néel-type skyrmions appears in chiral and polar crystals, respectively. Most of skyrmion materials, all examples above-mentioned for instance, show the Bloch-type ones. Recently, the Néel-type skyrmions was firstly observed in the non-centrosymmetric polar magnet GaV_4S_8[52]. Both Bloch- and Néel-type skyrmions are schematically shown in Fig. 1.4.

Moreover, magnetic biskyrmions with $N_S = 2$ (each is formed by two skyrmions of opposite spin helicities, Fig. 1.5) can be realized even in centrosymmetirc magnets because the biskyrmion is a chiral-symmetric object. Indeed, the magnetic biskyrmions were observed in thin plates of Sc-doped barium ferrite[53] and bilayered manganite[54] and recently in the hexagonal MnNiGa magnet using polycrystalline samples[55]. In these systems, the biskyrmions

are likely stabilized by the dipolar interaction combined with the low crystal symmetry[54]. In addition to the DM and dipolar interactions, other two origins of the skyrmions formation in thin plate magnets have been theoretically proposed as the frustrated exchange interactions[56] and the four-spin exchange interactions[57], which can lead to atomic-sized skyrmion structures[32]. The strength of one or combination of the above four interactions determines the emergence and extension of skyrmion structure in the magnetic phase diagram. In general, the skyrmion phases are only found very close to T_C and in presence of certain magnitude magnetic field, as revealed by the small angle neutron scattering (SANS), spin-polarized scan tunneling microscopy (STM) or Lorenz TEM.

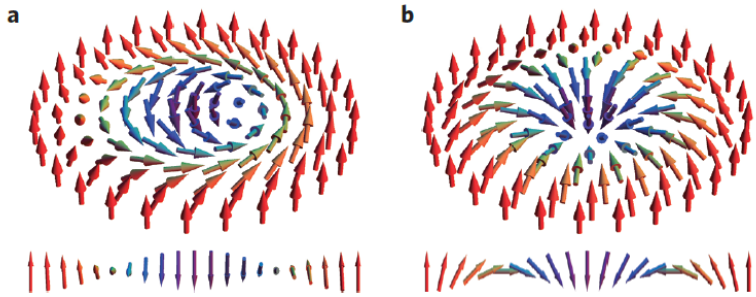

Figure 1.4: Individual magnetic skyrmions: (a) In a Bloch-type skyrmion, the spins curl in tangential planes (**b**) In a Néel-type skyrmion, the spins curl in radial planes. The out-of-plane cross-section of the vortex is also depicted at the bottom in each case[52].

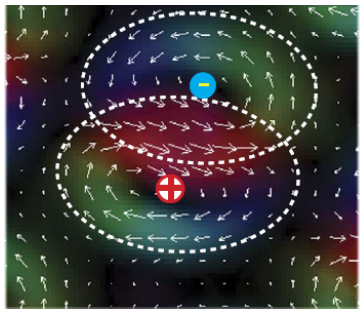

Figure 1.5: **Magnetic biskyrmions,** two single skyrmions of opposite spin helicities, stabilize in centrosymmetric skyrmions materials[54].

1.3.4 Topological electronic states

Electronic states with odd-parity electron-wave-functions are topologically different from the vacuum and conventional electronic states, where the electron wave functions have even-parity, because the parity is invariant against continuous transformations of wave functions. The so-called "topological electronic states" can be found in non-centrosymmetric crystals, for instance mono- or odd-number-layered honeycomb carbon network (graphene). In the graphenes, the electron-band has linear dispersion between the energy (E) and momentum (p), in contrast to quadratic dispersion in conventional electronic states. The effective mass approximation, which is valid in conventional electronic states, is collapsed in the linear-dispersive electronic states, where the effective mass $m^* = [\partial^2 E/\partial p^2]^{-1}$diverges. Instead, the linear-dispersive electrons can be effectively described by the relativistic Dirac equation of massless fermions, called as "Dirac electrons". Such Dirac electrons emerge on surfaces of

topological insulators, i.e. on interfaces between topologically different insulators (vacuum and topological insulators).

Further topologically nontrivial phases of matter that broaden the topological classification beyond topological insulators are the Dirac and Weyl semimetals, semimetallic materials with 3D Dirac or Weyl fermions that can be described by Dirac or Weyl-like equation, respectively. The Weyl fermion is one-half of a charged Dirac fermion of a definite chirality[58]. 3D Dirac electronic states have recently observed in many materials such as MoS_2[59], $Bi_{1-x}Sb_x$[60,61], A_3Bi (A = Na, K, Rb)[62], BiO_2[63], Cd_3As_2[64,65] and some distorted spinels[66]. The 3D Dirac point, where two Weyl points overlap in momentum space, is protected by crystal symmetry and symmetry breaking drive this 3D Dirac semimetal to a topological insulator or Weyl semimetal. As a 3D analogue to graphene with huge mobility of electrons, the 3D Dirac semimetal is anticipated to be important for future device applications of electronics and computing.

The topological electronic state can be predicted by band structure calculations and directly observed by experiments such as angle-resolved photoemission spectroscopy (ARPES) or scanning tunneling microscopy (STM). The bulk transport measurements also provide important evidences of the Dirac electronic states. One is that the linear energy dispersion of the massless Dirac fermions should manifest a linear magnetoresistance (MR) at the quantum limit, where all of the carriers occupy the lowest Landau level[67] . Another is the nontrivial π Berry phase which the electrons capture by circulating around the Dirac points. This Berry phase can be estimated from the Shubinikov de Haas (SdH) oscillation in magnetoresistance. The SdH oscillation, the peak position of magnetoresistance, is described as $1/B \propto 2\pi(n + 1/2 - \phi_B/2\pi)$, where ϕ_B is the Berry phase that should be 0 and π in conventional and topological Dirac electronic states, respectively. Thus, the Berry phase can be experimentally accessed by analyzing these oscillations[68], which is a striking topological feature of the massless Dirac fermions.

1.4 Co-based Shandites

1.4.1 Metal-rich chalcogenides

Compounds having a metal to chalcogen ratio greater than one form a class within the metal chalcogenides that show peculiarities regarding bonding and physical properties. The increased metal to chalcogen ratio implies that metal atoms become closer in this class and enriches the metal-metal bonding chemistry. A lot of research work to understand the origin of

many interesting properties based on metal-metal interactions has been carried out by the groups of A. Simon and J. Corbett [69–72]. Both binary and ternary metal-rich compounds form a wide variety of heterometallic bonds ranging from isolated clusters in Ni_9S_8[73], one-dimensional (1D) metal chains in Ti_5Te_4[74] and in $Sc_{14}M_3Te_8$ (M = Ru, Os)[75], two-dimensional (2D) metal slabs in Sc_9Te_2[76] and Ni_6SnS_2, $Ni_9Sn_2S_2$[77] to three-dimensional (3D) networks in Dy_2Te[78] and $Ta_9M_2S_6$ (M = Fe, Co, Ni)[79]. Many functional properties that make these compounds promising candidates for applications have been observed. For instance, many of these compounds show high thermoelectric performance[80–83] and compounds such as Ag_8MQ_6 (M = Si, Ge, Sn, Q = S, Se) are semiconductors showing high photosensitivity, high ionic conductivity and phase transitions[84–86].

Most of the ternary metal-rich chalcogenides contain a transition metal and occur by adding a second metal: alkali or alkaline earth, another transition, rare-earth or main group metal. In general, alkali or alkaline earth metal-rich chalcogens should be difficult to find due to the extra supply of electrons provided by the most electropositive metal and if so they will show a significant reduction of dimensionality. For instance, the structures of the polychalcogenides $Na_2Zn_3S_4$, Na_2ZnS_2 and Na_6ZnS_4 show respectively a 2D, 1D and 0D character while ZnS shows a 3D one[87]. On the other hand, transition metal atoms play a more important role in terms of bonding, creating new types of structures. The unusually strong bonding existing between early and late transition metals gives rise to the occurrence of two transition metal-rich chalcogenides such as $Ta_9M_2S_6$ (M = Fe, Co, Ni) [79] and Sc_6MTe_2 (M = Mn, Fe, Co, Ni)[88]. Furthermore, rare-earth metals share many common features with early transition metals originating a similar type of chemistry when combined with late transition metals, for example, in $Er_7Ni_2Te_2$[89] and $Lu_7Z_2Te_2$ (Z = Ni, Pd, Ru)[90]. Ternary metal-rich chalcogenides contain a transition and main group metal, however, remain quite unexplored. The well-known compound of this kind are the families of the M-Sb-Q systems (M = transition metal atoms; Q = S, Se, Te)[82], Ni-Sn-Q (Q = Se, Te)[77,91] and those with the formula $T_3M_2X_2$ (T = Co, Ni, Rh, Pd; M = In, Tl, Sn, Pb, Bi)[92,93] belonging to the parkerite (M = Bi)[94] or the shandite structure[95].

1.4.2 *Shandites and Parkerites: Variations and Structural relation*

The minerals $Ni_3Pb_2S_2$ and $Ni_3Bi_2S_2$ are the two archetypes of a family of ternary compounds with the general formula $T_3M_2X_2$ (T = Ni, Co, Rh, Pd or Pt; M = In, Sn, Pb, Tl or Bi; and X = S, Se or Te as shown in table 1.1). The former is known as shandite (in honour of Professor S. J. Shand,1882-1957)[95] while the later was named parkerite by Scholtz in 1936[94].

Only when M = Bi, ternary compounds $T_3M_2X_2$ crystallize in the parkerite structure, otherwise shandite structure occurs. $Ni_3Pb_2S_2$ crystallizes in the trigonal space group $R\bar{3}m$ where the Ni atoms occupy 9*d* Wyckoff sites, S atoms at 6*c* positions and Pb atoms are split between two positions: Pb(1) in 3*a* and Pb(2) in 3*b*.

Despite having the same stoichiometry as the mineral shandite, $Ni_3Bi_2S_2$ crystallizes in a different structure but still related. The parkerite $Ni_3Bi_2S_2$ crystallizes in the monoclinic structure of the space group C_2/m, in which Ni atoms occupy three crystallographic

Table 1.1: Shandites and parkerites of the general formula $T_3M_2X_2$ are made up of a lately transition metal T (red) from groups 9 or 10 with limited substitutions from group 8 (green) in the periodic table, an element M from the main groups (shown in blue) and a chalcogen S or Se (yellow).

	3	4	5	6	7	8	9	10	11	12		13	14	15	16
												B	**C**	**N**	**O**
											3*p*	**Al**	**Si**	**P**	**S**
3*d*	**Sc**	**Ti**	**V**	**Cr**	**Mn**	**Fe**	**Co**	**Ni**	**Cu**	**Zn**	4*p*	**Ga**	**Ge**	**As**	**Se**
4*d*	**Y**	**Zr**	**Nb**	**Mo**	**Tc**	**Ru**	**Rh**	**Pd**	**Ag**	**Cd**	5*p*	**In**	**Sn**	**Sb**	**Te**
5*d*	**Lu**	**Hf**	**Ta**	**W**	**Re**	**Os**	**Ir**	**Pt**	**Au**	**Hg**	6*p*	**Tl**	**Pb**	**Bi**	**Po**
6*d*	**Lr**	**Rf**	**Db**	**Sg**	**Bh**	**Hs**	**Mt**	**Ds**	**Rg**	**Cn**	7*p*	**Uut**	**Fl**	**Uup**	**Lv**

independent positions corresponding to the Wyckoff sites 4*g*, 4*e* and 4*i*. Bi and S atoms occupy two 4*i* and one 8*j* positions, respectively. Table 1.2 presents the hitherto experimentally possible shandites and parkerites by substituting Ni and Pb/Bi with the appropriate atoms. $Pd_3Bi_2S_2$ and $Pt_3Bi_2Se_2$, however, are reported recently as parkerites aberrantly crystallize in a cubic unit cell of the space group $I2_13$, isostructural to the corderotite $Hg_3Cl_2S_2$, and do not crystallize in the monoclinic system of other perkerites[96,97]. The structural relation between the shandite and parkerite (monoclinic and cubic) structures has been comprehensively studied by means of powder and single crystal X-ray diffraction and DFT modeling by the group of R. Weihrich[96,98–101]. The cubic potassium oxoplumbate (II), $K_2Pb_2O_3$ and the trigonal potassium oxostannate (II) $K_2Sn_2O_3$ were introduced as oxygen deficient perovskites resembling the peroveskite $CaTiO_3$ with half occupied sites of O atoms (expressed by the formulas $KPbO_{3/2}$ and $KSnO_{3/2}$)[102–104]. R. Weihrich et. al. discussed the type-anitype relations of the aforesaid oxometallates (II) to the trigonal shandite and monoclinic and cubic parkerite and classified them in a wider group of compounds called half antiperovskites (HAP), with the general formula $T_{3/2}MX$; a sub-group of the antiperoveskites group includes the superconductor Ni_3MgC[98,99]. This HAP group has a primitive unit cell that can be extracted from a superstructure of 8 cubelets in which only half of the T sites are occupied following a certain

Table 1.2: Experimentally possible shandites and parkerites.

T	*X* \ *M*	Shandite Pb	Shandite Sn	Shandite In	Shandite Tl	Parkerite Bi
Ni	**S**	$Ni_3Pb_2S_2$	$Ni_3Sn_2S_2$	$Ni_3In_2S_2$	$Ni_3Tl_2S_2$	$Ni_3Bi_2S_2$
	Se	$Ni_3Pb_2Se_2$		$Ni_3In_2Se_2$		$Ni_3Bi_2Se_2$
Co	**S**		$Co_3Sn_2S_2$	$Co_3In_2S_2$		
	Se					
Rh	**S**	$Rh_3Pb_2S_2$	$Rh_3Sn_2S_2$	$Rh_3In_2S_2$	$Rh_3Tl_2S_2$	$Rh_3Bi_2S_2$
	Se	$Rh_3Pb_2Se_2$				$Rh_3Bi_2Se_2$
Pd	**S**	$Pd_3Pb_2S_2$			$Pd_3Tl_2S_2$	$Pd_3Bi_2S_2$
	Se	$Pd_3Pb_2Se_2$			$Pd_3Tl_2Se_2$	$Pd_3Bi_2Se_2$
	Te	$Pb_2Pd_3Te_2$				
Pt	**S**	$Pt_3Pb_2S_2$				
	Se	$Pt_3Pb_2Se_2$				$Pt_3Bi_2Se_2$

ordering scheme. The *T* atoms occupation and ordering results in variations in the *T*-*X* networks form 3D framework of the cubic parkerites to a 2D ones in the trigonal shandites and monoclinic parkerites[97,105,106]. The structure of 3D framworks explains the absence of superconductivity in cubic pakerites, whereas superconducting behavior was only found for the monoclinic parkerites that may be related to the layered structure analogously to cuprates and the novel oxopnictides[107–109]. However, superconductivity has never been reported in shandite phases, implying a crucial role of the ordering or bonding of *T* site. Bonding and antibonding states of Bi-6*p*, Pd-4*d* and Se-4*p* contributing to the flat and steep bands at the Fermi level are reported for the superconductor $Pd_3Bi_2Se_2$[106].

1.4.3 Shandite structure

Figure 1.6, illustrated by the VESTA software[110], shows the shandite type crystal structure of $T_3M_2X_2$. As shown in Fig. 1.6(a), the *T* and *X* atoms occupy the unique Wyckoff positions 9*e* (1/2,0,0) and 6*c* (0,0,z), respectively, while the *M* atoms are distributed between two positions, 3*b* (0,0,1/2) and 3*a* (0,0,0). The shandite-type crystal can be considered to consist of metallic layers stacked in ABC fashion along *c*-direction in a hexagonal notation. The layers are arranged in the kagomé network of corner-sharing triangles of the *T* atoms and triangular one of the intra-layer *M* atoms on 3*a*-site (*M*2), see Fig. 1.6(b). Each *T* triangle is alternately caped above and below by an S atom. *X* and *M* atoms on 3*b* (*M*1) locate at interlayer positions and the *T*-*M*2 layers are connected via the interlayer *M*1 atoms.

The shandite structure can also assumed as a build of layers of face-sharing octahedra formed by the coordination of each *T* atom; surrounded by two *M*1, two *M*2 and two *X* atoms; as seen in Fig. 1.6(c). The *M*1virtices of such octahedra lie on 3-fold axes perpendicular to the layers, i.e. the octahedra are related by 120° rotations forming triangular arrays within each layer, the *T*-kagomé lattices. On the other hand, each *M*2 atom lies in the center of a planer 6 *T*-hexagon and in the middle of a 3D hexagonal bipyramid along with two sulphur atoms (Fig. 1.6(d)), while the inter-layers *M*1 atoms locate in trigonal antiprismatic sites generated by the *T* atoms triangles in adjacent layers (Fig. 1.6(e)).

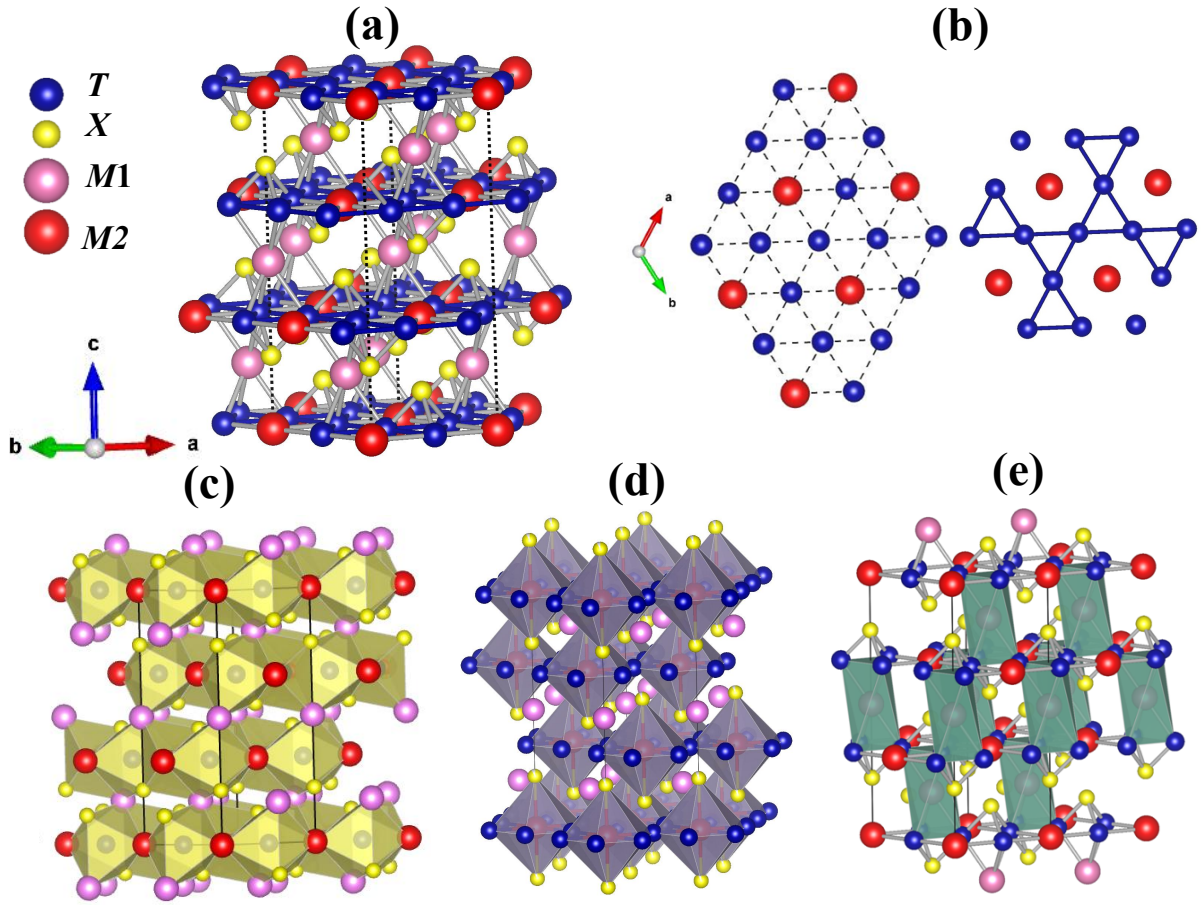

Figure 1.6: (a) Crystal structure of $T_3M_2X_2$ shandite showing atoms stacking metallic layers along the *c*-direction in the hexagonal notation. (b) Metallic layer consisting of the 2D kagomé lattice of *T* and triangular lattice of *M*2 atoms. The crystal structure showing (c) the face-sharing *T* atoms polyhedra, in each *T* atom is octahedrally surrounded by two *M*1, two *M*2 and two *X* atoms (d) the intra-layers *M*2 atoms in the center of polyhedra of hexagonal bipyramids along with two sulphur atoms. (e) the inter-layers *M*1 atoms locate in trigonal antiprismatic polyhedra of 6 *T* atoms. These structures were drawn using the VESTA software[110].

All atoms in the shandite compounds are fixed by symmetry excepting the *z* coordination of the *X* atom, which varies as well as the lattice parameters between different compounds and by chemical substitutions. Table 1.3 presents the positions and coordinates of

atoms in the shandite trigonal structure. The *z* coordinate shows the displacement of the *X* atoms along the hexagonal *c*-axis and determines the metal chalcogen distances. For instance, the structure of the $Co_3Sn_2S_2$ shandite was determined using powder and single crystal diffraction by many groups showing the characteristic kagomé lattice of cobalt atoms with short Co-Co distances (2.68 Å), slightly longer than those found in Co metal (2.50 Å), and is isopointal to $Ni_3Pb_2S_2$. A value of ~ 0.2828 was found for the sulphur *z* coordinate giving rise to remarkably short Co-S distances (2.18 Å) compared to Co-S bonds in other binary or ternary sulphides[101].

Table 1.3 Positions and coordinates of atoms in the shandite trigonal structure of the space group $R\bar{3}m$ (hexagonal setting).

Atom	Wyckoff Site	*x*	*y*	*z*
T	9*d*	1/2	0	1/2
*M*1	3*a*	0	0	0
*M*2	3*b*	0	0	1/2
X	6*c*	0	0	*z*

As the only compounds show a magnetic ordering with 2D spin-frustrated Co-kagomé networks, $Co_3Sn_2S_2$ and its possible solid solutions[111–113], are candidates of exotic magnetic, as well as electronic, properties.

1.4.4 Known properties of Co-based shandites

Among the shandite and parkerite compounds, Co-based shandite $Co_3Sn_2S_2$ and its related compounds have been investigated extensively in recent years because of the rich variety of their observed and theoretically-predicted magnetic and electronic properties: half-metallic ferromagnetism[100,101,114], magnetic-nonmagnetic phase transition[101,115], high thermoelectronic properties[83,116], and anisotropic conductivity[117].

$Co_3Sn_2S_2$ lonely shows a magnetic (ferromagnetic) order within all compounds crystallize in shandite or parkerite structures, with a Curie temperature T_C ~ 172 K[100,115]. Strong uniaxial anisotropy of magnetization with spontaneous magnetic moment at 2 K of ~ 0.3 μ_B/Co along the easy axis have been recently observed using single crystals prepared out of Sn-flux[118] and by a modified Bridgman method[119], as shown in Fig. 1.7(a). The observed spontaneous magnetic moment is much smaller than the effective moment, ~ 0.6 μ_B/Co, at higher temperatures than T_C, indicating weakly itinerant electron ferromagnetism. Specific heat measurements showed a possible second order ferromagnetic transition at 172 K with

pronounced λ-type anomaly in the specific heat and no significant magnetostructural coupling was observed. The reported specific heat results are shown in Fig. 1.7(b). Results of DFT electronic band calculations[100,119] shown in Fig. 1.7(c and d), supported by results of photoemission spectroscopy experiment [120], indicated a half-metallicity of the ferromagnetic state in $Co_3Sn_2S_2$, which is classified as a type I_A half-metallic ferromagnet[121]. The electronic band structure calculation shown in Fig. 1.7(c) indicates that $Co_3Sn_2S_2$ has a pseudo-gap just below the Fermi level, which locates between the bands 23 and 24, for only one spin-channel. In $Co_3Sn_2S_2$ of 47 valence electrons per formula unit, the band 23 is fully occupied according to the LCAO counting scheme, whereas, the band 24 is half occupied. The spin polarized state

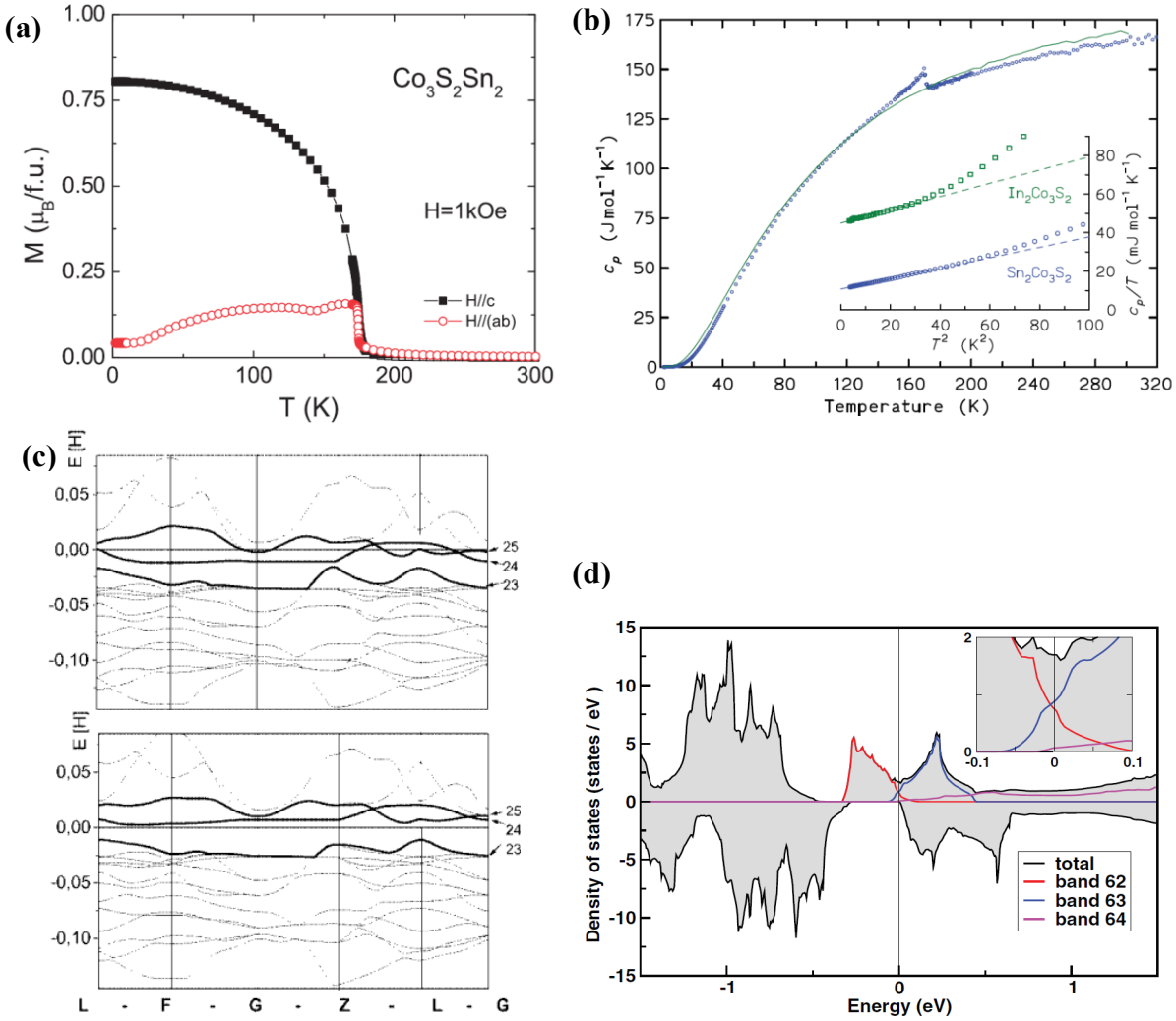

Figure 1.7: (a) Anisotropic temperature dependent magnetic susceptibility of $Co_3Sn_2S_2$[118], (b) Molar heat capacity of single crystalline $Co_3Sn_2S_2$ compared to that of a polycrystalline $Co_3In_2S_2$[119], (b) Electronic band structures for spin polarized $Co_3Sn_2S_2$: up (top) and down (bottom) spin channels[101] and (d) Spin-polarized DOS per formula unit of $Co_3Sn_2S_2$ show the contributions of the individual bands. The inset in (d) is a magnification around E_F[119].

attributes to a lift of the spin degeneracy of the half-filled band 24, which is occupied only in the up-spin channel. Typically compensated metallic state was reported in the ferromagnetic state of $Co_3Sn_2S_2$ based on the DFT calculations, shown in Fig. 1.7(d).

The ferromagnetic order in $Co_3Sn_2S_2$ is suppressed by the chemical substitution, especially for Co- and Sn-sites. For instance, the Ni- and Fe-substitution for Co and the In-substitution for Sn suppress the ferromagnetic order and a ferromagnetic instability was observed in the In-substituted system[101,111,112,122,123], while the Se-substitution for S causes slight reduction of T_C[124,125]. According to a LCAO counting simple scheme, the electron number is anticipated to be a significant factor controlling magnetism of $Co_3Sn_2S_2$[101,126]. For that Co_3SnInS_2 of 46 electrons per unit cell is a paramagnet. In opposite to Ni-substitution, In- and Fe-substitution correspond to electron count reduction. Figures 1.8(a) and (b) show the previously reported calculations of the electronic band structures of selected compositions of $Co_3Sn_{2-x}In_xS_2$[117] and $Co_{3-y}Fe_ySn_2S_2$[123], respectively. A narrow gap opening has been predicted based on these calculations for $x = y = 1.0$ in both $Co_3Sn_{2-x}In_xS_2$ and $Co_{3-y}Fe_ySn_2S_2$. Although $Fe_3Sn_2S_2$ is unstable, polycrystalline samples of $Co_{3-x}Fe_xSn_2S_2$ with limit solubility of $y \sim 0.6$ at ambient pressure was recently prepared by the group of M. Matoba[123]. They reported that the solubility can be extended to $x \sim 1.0$ by employing the high temperature (HT) and high pressure (HP) technique. The reported lattice structural effects of In- and Fe-substitutions are shown in Figs. 1.8(c) and (d). Large trigonal distortion, metallic layers' separation, and kinks in the compositional variations of the lattice parameters around $x = 1.0$ have been observed in $Co_3Sn_{2-x}In_xS_2$. On the other hand, Fe-substitution for Co results in relatively much small crystal distortion in $Co_3Sn_2S_2$ lattice.

The counterpart to $Co_3Sn_2S_2$ half metallic ferromagnet in $Co_3Sn_{2-x}In_xS_2$, $Co_3In_2S_2$ is expected based on the electronic structure calculations to be a nonmagnetic metal locates at the edge of magnetic instability and shows an anisotropic conductivity[117]. Furthermore, the semiconducting (or semimetallic-like) behavior that can be tuned by In or Se chemical substitutions to obtain promising thermoelectric properties have been reported in Co_3SnInS_2 based on experimental measurements of the transport properties using polycrystalline samples[83,101,114,116,127]. Figures 1.8(e) and (f) show the transport properties of $Co_3Sn_{2-x}In_xS_2$ measured at temperatures above 100 K using sintered polycrystalline samples[127]. The results show that the Fermi level can be tuned by In-substitution with sign change of the Seebeck coefficient and large increase of resistivity around $x \sim 1.0$ with enhanced thermoelectric properties.

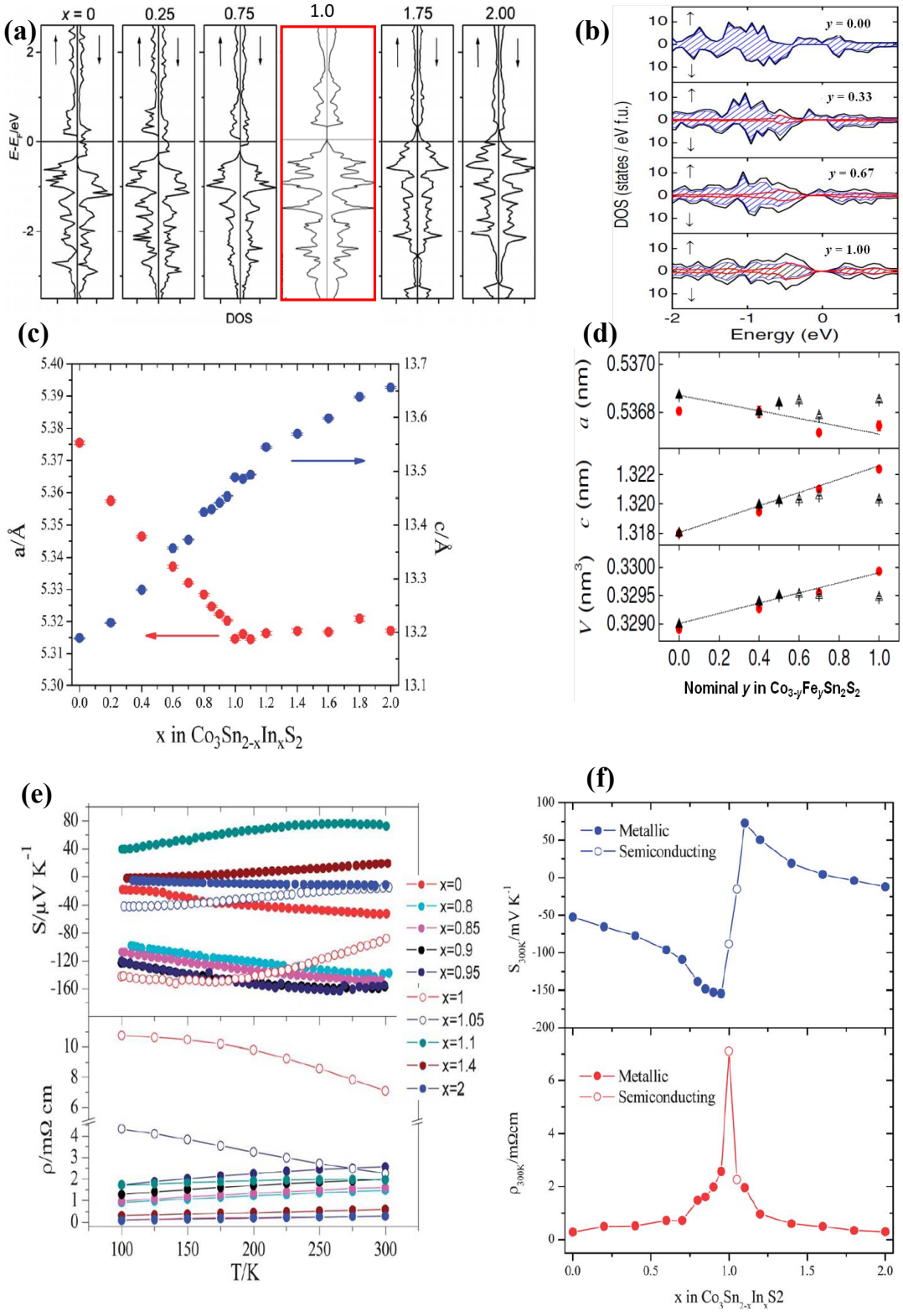

Figure 1.8: Compositional variation of (a), (b) spin polarized DOS[117,123], and (c), (d) lattice parameters[123,127] of $Co_3Sn_{2-x}In_xS_2$ and $Co_{3-y}Fe_ySn_2S_2$, respectively. (c) and (d) Seebeck coefficient (top) and electrical resistivity (bottom) at varying and room temperature, respectively, for $Co_3Sn_{2-x}In_xS_2$[127].

1.5 Aim of the Present Study

The previously reported results of band structures calculations and investigations using solid solution polycrystalline samples indicate that the layered Co-based shandites are of much interest as good candidates for further exotic properties due to an expected Q2D electronic state. Furthermore, the highly spin-frustrated Co-kagomé networks are of good interest in the viewpoint of magnetism. Single crystals of the Co-shandites and its solid solutions would be strongly required to investigate for these intriguing properties in further detail.

In the present study, successful growth of single crystals of $Co_3Sn_2S_2$ and $Co_3Sn_{2-x}In_xS_2$ ($0 < x \leq 2$) and $Co_{3-y}Fe_ySn_2S_2$ ($y \leq 0.5$) solid solutions using two molten methods, the flux-method and a modified Bridgman method, was targeted. Optimal conditions to obtain large single crystals are discussed in this chapter 2 of the thesis. Characterization results of the grown crystals using WDS, XRD and magnetization measurements are presented. The effects of the substitutions on the crystal structure are followed by the Rietveld refinement using the XRD experimental data. The anisotropic magnetic and transport properties of these layered compounds were carefully measured using single crystals oriented by the Laue XRD spectroscopy. The magnetic ground states of $Co_3Sn_2S_2$ was carefully investigated via magnetization and ac susceptibility. Further investigations of the magnetic and electronic states of $Co_3Sn_2S_2$ and $Co_3Sn_{2-x}In_xS_2$ ($0 < x \leq 2$) and $Co_{3-y}Fe_ySn_2S_2$ ($y \leq 0.5$) were performed by measuring the longitudinal and transverse resistivities and the specific heat of many compositions.

1.6 Outline of the Present Dissertation

In the present chapter, a brief introduction to magnetism in metals in general and several topics of topological phenomena related with my study in particular has been presented. General survey of Co-based shandites and related compounds has also been briefly introduced. In chapter two; the experimental procedures: synthesis and crystal growth methods, used characterization techniques and the magnetic and transport measurements are described. The experimental results of the crystal growth and the structural properties of $Co_3Sn_{2-x}In_xS_2$ ($0 < x \leq 2$) and $Co_{3-y}Fe_ySn_2S_2$ ($y \leq 0.5$) are detailed in chapter three. Chapter four, five and six are devoted for the magnetic properties of $Co_3Sn_2S_2$, $Co_3Sn_{2-x}In_xS_2$ ($0 < x \leq 2$) and $Co_{3-y}Fe_ySn_2S_2$ ($y \leq 0.5$) based on the magnetization, ac susceptibility and Hall resistivity measurements. The electronic transport properties investigated by resistivity and specific heat at zero magnetic field are presented and discussed in chapter seven. Finally, chapter eight concludes the present study.

CHAPTER 2

2 Experimental Procedures

2.1 Outline

In the present chapter, the experimental techniques employed for the crystal growth, characterization and subsequent measurements of the magnetic and electronic transport properties of Co-based shandites are described. The crystals were synthesized by the flux method and furtherly by a modified Bridgeman method from the polycrystalline molten. The procedure of the former is detailed in subsect. 2.2.1 of this chapter. Stoichiometric polycrystalline samples required for the later were synthesized by the solid state reaction as briefly described in subsect. 2.2.2. The Bridgeman crystal growth is described in details in the subsects. 2.2.3. The experimental procedures of the characterization and properties measurements of the grown crystals are detailed in sect. 2.3. The grown $Co_3Sn_{2-x}In_xS_2$ ($0 \leq x \leq 2$) and $Co_{3-y}Fe_ySn_2S_2$ ($0 \leq y \leq 0.53$) crystals were characterized by powder x-ray diffraction (XRD) and the crystal structure parameters were refined by the Rietveld analysis. The chemical compositions were investigated by wavelength-dispersive x-ray spectroscopy (SEM-WDS) and the crystals quality as well as crystal axes were identified by a Laue X-ray camera. The magnetic properties were measured systematically by magnetization and ac susceptibility as described in subsect. 2.3.4. The anisotropic transport properties of Co-shandites crystals were studied by resistivity, magnetoresistance, Hall resistivity and specific heat measurements, described in later subsects.

2.2 Synthetic Methods

2.2.1 Crystals growth by a flux method

Synthesis of sulfide crystals out of a solid solution is challenging due to the low boiling point and polymeric nature of S. However, some sulfur bearing single crystals have been grown by the group of P. C. Canfield out of binary sulfur-metal solutions[118]. The single crystals of Co-based shandites used in the current study were grown by a flux method[128–132], by initially following the precautions in their recent report for the synthesis of sulfur bearing crystals[118].

Raw materials of lumps of Co (99.9 % HIGH PURITY CHEMICALS) and Fe (99.95 % Alfa Aesar), Grains of Sn and In (99.999 % HIGH PURITY CHEMICALS), grains of Pb (99.99 % RARE METALLIC CO., LTD.) and grinded crystals of S (99.999 % nacalai tesque) were used in these reactions.

For $Co_3Sn_{2-x}In_xS_2$ single crystals growth, we found that Sn/In self flux is available only for the single crystals of pure Sn/In shandites, $Co_3Sn_2S_2$ and $Co_3In_2S_2$, and solid solutions containing low In concentration up to $x \sim 0.35$, as indicated by WDS results presented below in subsect. 3.3.1 of chapter 3. Crystals of these compositions were grown by using the initial molar ratios Co: S: (Sn+In) = 8: 6: 86. The stoichiometric Sn-In binary self-flux is not available for the solid solution crystals with higher In concentration. Instead of it, we successfully grew the crystals of $x > 0.35$ by using mixture-flux of Sn, In and Pb with an initial composition of Co: S: Sn: In: Pb = 6: 6: 36-18x_{nom}: 18 x_{nom}: 52, where x_{nom} is the nominal In concentration initially used. We should note that $Co_3Pb_2S_2$ is not a stable phase and cannot be synthesized even if Pb flux is used[133,134].

Single crystals of $Co_{3-y}Fe_ySn_2S_2$ ($0 \leq y \leq 0.53$) were grown by a flux-method[128–132] similar to the growth of $Co_3Sn_2S_2$ single crystals[111] by employing Sn as a self-flux. The constituents were mixed in an initial mixture of molar ratios (Co + Fe): S: Sn = 8: 6: 86. The Pb-flux which was found to be available for growing single crystals of $Co_3Sn_{2-x}In_xS_2$[111], was also employed in an initial composition of (Co + Fe): S: Sn: Pb = 6: 6: 36: 52 in a trial to extend the solubility of $Co_{3-y}Fe_ySn_2S_2$. However, the actual Fe-concentration in the crystals grown out of Pb-flux was found to be largely reduced

Two Al_2O_3 crucibles were used to provide the growth environment. The constituent elements were placed in one crucible which was used as a growth crucible while the other one filled with quartz wool was put on the growth crucible upside down to reduce the flow-out of the evaporated sulfur and furthermore to filter and immobilize the excess flux at the end of the growth as explained below. Both were sealed in an evacuated quartz ampoule, as shown in Fig. 2.1(a). By making use of the available phase diagrams of the constituents, the temperature sequence in the growth process has been set. Fig. 2.2 shows the binary phase diagram of Sn-S and Co-Sn[135,136]. The quartz ampoule was put in an electric box-furnace and was initially heated to 400 °C over 2 hours where it was held for extra 2 hours to avoid an evaporation of sulfur by making it reacts with Sn-In flux. Then it was heated up to 1050 °C, being higher than the melting temperature of the mixture, over 6 hours. After keeping at 1050 °C for extra 6 hours to wait for the constituent melts homogeneously, the molten was cooled slowly to 700 °C over 70 hours. The ampoule was removed from the electric furnace at 700 °C to remove the flux via rapid decanting and subsequent spinning of the ampoule in a centrifuge. Hexagonal plate-shaped crystals up to 7 mm in size were obtained, see Fig. 2.1(b).

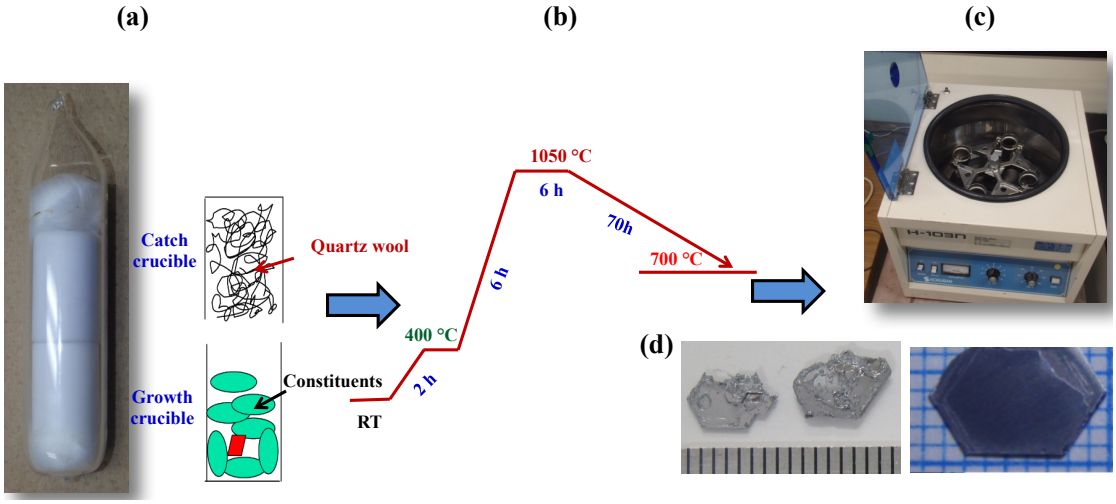

Figure 2.1: (a) Configuration of the flux-growth environment in side a sealed quartz ampoule after evacuation, (b) a diagram of the followed temperature sequence, and (c) the used centrifuge to separate the flux molten from solid crystals in a decanted ampoule. (d) images of the flux-grown single crystals of Co-based shandites. The division in (d) is 1 mm.

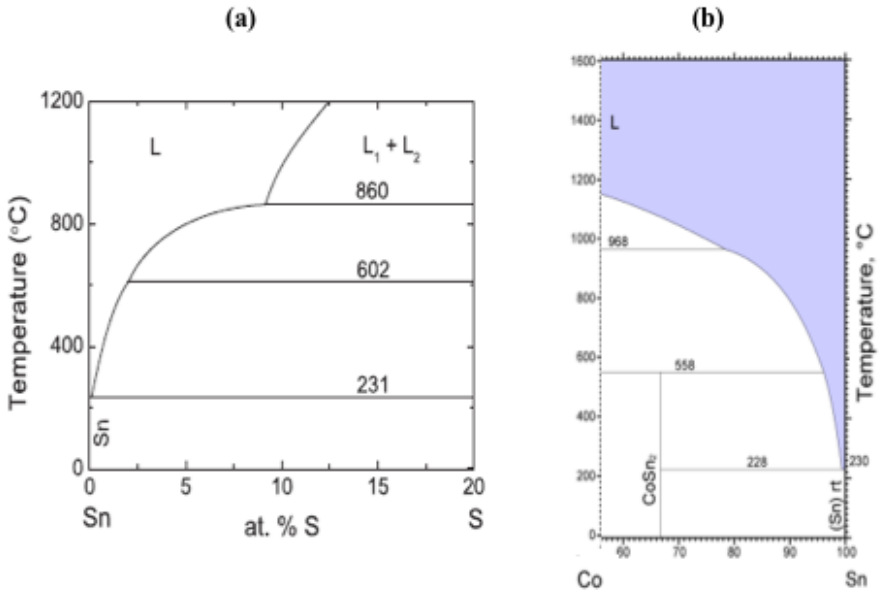

Figure 2.2: Binary phase diagrams of (a) S-Sn and (b) (a) Co-Sn.

2.2.2 Solid state reaction

A simple method to synthesis polycrystalline solid is by mixing the powder elements prior to a reaction at much lower temperature than the melting point of the desired phase, the so called solid state reaction. This lower temperature is to avoid local deviations from the initial stoichiometry and the formation of unwanted impurities.

To synthesis polycrystalline samples of Co-based shandites, stoichiometric quantities of the starting elements (Co of 99.9 % HIGH PURITY CHEMICALS, Sn and In of 99.999 % HIGH PURITY CHEMICALS and grinded crystals of S of 99.999 % nacalai tesque) were used. The Co powder was first reduced in a hydrogen atmosphere for 12 hours at 600° C. The constituents were mixed in an agate mortar before being put into a quartz tube and sealed under vacuum (10^{-5} torr). Following the polycrystalline previously reported procedure[127], $Co_3Sn_2S_2$ was prepared by heating the mixture at 500°C for 48 h and then at 700° C for 48 h with regrinding and pressing to pellets in between and cooling rate 0f 0.5 deg./min. $Co_3In_2S_2$ was prepared by firing the powder mixture at 800ºC for 96 h for three times with intermediate re-grinding and pressing to pellets with a heating and cooling rates of 0.5 ºC min^{-1}. The solid solutions $Co_3Sn_{2-x}In_xS_2$ and $Co_{3-y}Fe_ySn_2S_2$ were prepared by firing twice at 900 °C and 600 °C, respectively, for 48 h with regrinding in between. Finally, powdered samples were pressed in pellets shape to be sintered at 700 °C for 24 h for $x = 0.0$, at 800 °C for $0 < x \leq 2$ and at 600 °C for $Co_{3-y}Fe_ySn_2S_2$, $y > 0$. The product phase of all compositions was followed by powder x-ray diffraction (XRD) at room temperature.

2.2.3 Crystals growth by a modified Bridgeman method

Single crystals of $Co_3Sn_2S_2$ and its solid solutions $Co_3Sn_{2-x}In_xS_2$ have been grown successfully by a modified Bridgeman method by following a previously described details for $Co_3Sn_2S_2$ synthesis[120] with extra modification. For this purpose, stoichiometric polycrystalline samples were placed in a tipped glassy carbon crucible. The crucible was simply inserted into a quartz tube and sealed under vacuum. The tube was suspended by a Kanthal thread from the top to the hot zone of a vertical tube furnace. The sample was slowly heated over 30 hours up to 1000 °C (for $Co_3Sn_2S_2$) and 1050 °C (for $Co_3Sn_{2-x}In_xS_2$), kept there for 6 h, and slowly cooled within 72 h to 800 °C. Note that the furnace is vertically temperature-gradient and the bottom of the ampoule is targeted at lower temperature. After these steps the furnace was turned off and the samples were cooled down to ambient temperature by air quenching. Figure 2.3 summarizes the above described procedure of the modified Bridgman growth. The finally removed crystals from the glassy carbon tube has the tipped cylindrical shape of its crucible frame, with typical lengths of ~ 5 cm and 1 cm in diameter. The grown crystals exhibit cleavage plans that are randomly oriented with respect to the crucible axis. Laue X-ray investigations indicated (001) cleavage planes. By carful mechanical fragmentation the crystal, bright and flat surface of the (001) planes shown in Fig. 2.3(c) can be easily obtained.

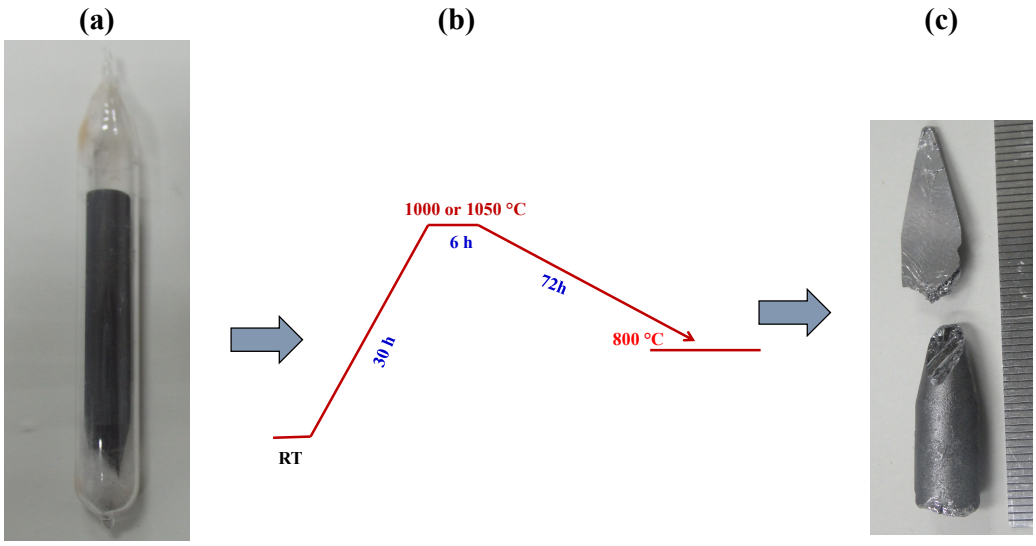

Figure 2.3: The modified Bridgman procedure in which (a) a sealed quartz ampoule after evacuation includes a tipped glassy carbon crucible that contains the polycrystalline sample, (b) a diagram of the followed temperature sequence. (c) Images of the flux-grown single crystals of Co-based shandites. The division in (c) is 1 mm.

2.3 Characterization and Measurements

2.3.1 Wavelength-dispersive x-ray spectroscopy

When a beam of electrons of sufficient energy interacts with a sample target it generates characteristic X-rays, discovered and named by Wilhem Röntgen in 1895. As electromagnetic waves with a wavelength in the range between 0.01 and 10 nm, which is the order of magnitude of interatomic distances, they make possible nondestructive testing of materials as well as a probe of the order at the atomic level. For instance, the chemical composition can be investigated by energy- and/or wavelength-dispersive X-ray spectroscopies (EDS and WDS), the crystallography can be identified using the powder and/or single crystal X-ray diffraction (XRD) and Laue X-ray spectroscopy. X-ray radiation is diffracted by crystalline solid structures giving rise to a very definite pattern that acts as the structure fingerprint. Constructive interference of n order, caused by the atoms lying in the (hkl) planes that are at a distance d from each other, takes place only if the incident and diffracted beams of wavelength λ and angle θ between them fit the criteria of Bragg's law:

$$2d_{hkl} \sin\theta = n\lambda \qquad (2.1)$$

Wavelength-dispersive X-ray spectroscopy (WDS) is a technique used to count the number of X-rays of a specific wavelength diffracted by analytical crystal(s) with specific lattice spacing(s), unlike the related technique of energy-dispersive X-ray spectroscopy (EDS)

which produce and detect a broad spectrum of wavelengths or energies simultaneously. WDS is mainly used in chemical analysis, in an X-ray fluorescence spectrometer or in transmission or scanning electron microprobes. Based on the superior peak resolution of constituents and sensitivity of trace elements, a wavelength-dispersive spectrometer enables quantitative analyses of the individual elements at spot sizes as small as a few micrometers.

The chemical compositions (presented in chapter 3) of the grown crystals of $Co_3Sn_{2-x}In_xS_2$ and $Co_{3-y}Fe_ySn_2S_2$ were investigated by SEM-WDS (Hitachi, S-3500H) to obtain the actual In and Fe concentrations in the solid solution grown crystals and to investigate for the stoichiometry within the crystals.

2.3.2 Powder X-ray Diffraction and Rietveld analysis

In the field of crystallography, monochromatic radiation produced by electrons collision against a metallic target is highly desirable. The electrons are accelerated by high voltages and superimposed radiation of the two intense wavelengths K_α (corresponding to 2p → 1s transition) and K_β (corresponding to 3p → 1s transition) is typically emitted at 20 - 50 kV. The K_β radiation is eliminated by means of monochromators or nickel filters before passing through the sample. In fact, the wavelength K_α is actually a doublet of $K_{\alpha1}$ and $K_{\alpha2}$, with slightly different energies due to the splitting of 2p orbital by spin-orbit interaction (Zeeman effect). In high precise diffractometers, also $K_{\alpha2}$ is eliminated. The diffracted radiation pattern is then recorded and analyzed. Depending on whether this pattern has been reflected from the sample or has gone through it, the diffraction geometries can be classified as Bragg-Brentano (flat plate geometry) or Debye-Scherrer (transmission geometry), respectively. The target metal most commonly used is copper both for being cheap and with an intermediate wavelength while molybdenum is the most common target for single crystal X-ray diffraction, given that its shorter wavelength radiation produces diffraction spots that are closer together.

To identify the phase of the grown crystals of $Co_3Sn_{2-x}In_xS_2$ and $Co_{3-y}Fe_ySn_2S_2$, powder XRD patterns presented in chapter 3 were measured at room temperature using X-ray diffractometer (X'Pert Pro, PANalytical) with Cu $K_{\alpha1}$ radiation monochromated by a Ge (111)-Johansson-type monochromator, in the Bragg-Brentano geometry. Further refinement of the structure, lattice constants and other crystal structure parameters, has performed by the Rietveld method using the RIETAN-FP software[137] and/or TOPAS software Version 5 (from Bruker AXS)[138].

2.3.3 Laue X-ray photography

Another X-ray based technique used to determine the orientation of single crystals is known as Laue x-ray method. White radiation is reflected from, or transmitted through, a fixed crystal. The diffracting planes in the crystal are determined by knowing that the normal to the diffracting plane bisects the angle between the incident beam and the diffracted beam. A Greninger chart can be used to interpret the back reflection Laue photograph[139]. The crystal axes of our grown single crystals were identified using a Shimadzu Laue camera XD-3A.

2.3.4 Magnetization and ac susceptibility

The magnetic properties of single crystals (and for powder polycrystalline samples in emphasis measurements) of $Co_3Sn_{2-x}In_xS_2$ ($0 \leq x \leq 2$) and $Co_{3-y}Fe_ySn_2S_2$ ($0 \leq y \leq 0.53$) were studied via magnetization and ac susceptibility measurements using a SQUID magnetometer (MPMS, Quantum Design) installed in the Research Center for Low Temperature and Materials Science (LTM) of Kyoto University, in a temperature range of 2 –350 K and magnetic fields up to 7 T. The MPMS facility is schematically described in Fig. 2.4(a). For the ac susceptibility measurements, 1 Oe drive ac field of different frequencies was supercomposed on the bias field and both were applied along the *c*-direction.

Two experimental regimes have been followed in the measurement of temperature-scans of magnetization and ac susceptibility:

(i) Zero-field-cooled (ZFC) scans, after resetting the magnetometer to zero field, the sample was brought to 5 K (and then to the temperature of interest in case of frequency scans) under

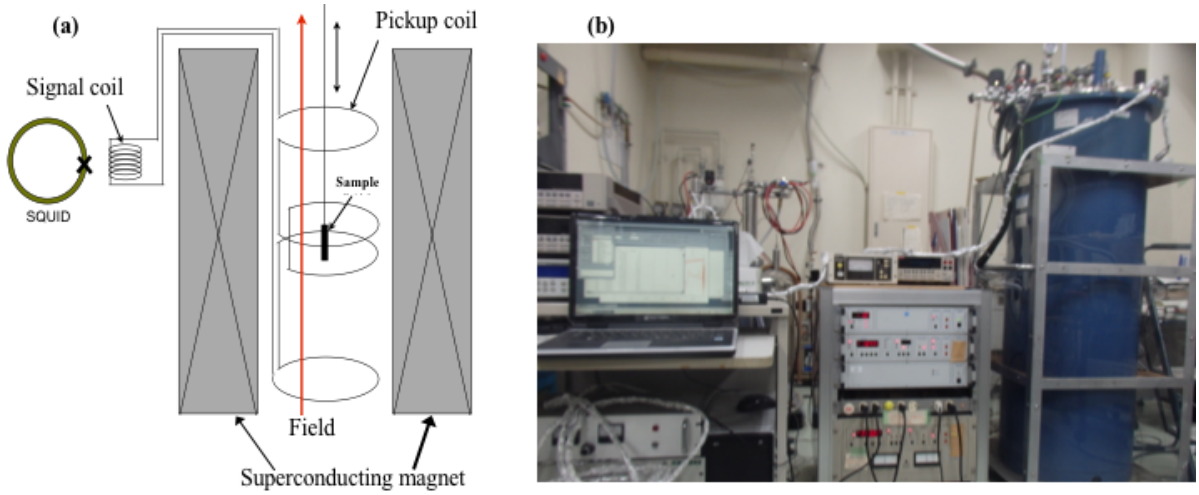

Fig 2.4: (a) Description of MPMS measurements and (b) the helium-4 refrigerator used for transport properties measurement in magnetic fields up to 5 T.

zero field. The magnetic fields were applied at 2 K and the measurement were performed by increasing stepwise the temperature, after thermal equilibrium was reached at each temperature. (ii) Field-cooled (FC) scans, in which the sample was cooled from 250 K, where the dc and/or ac magnetic fields were applied, and the measurement was performed with decreasing stepwise the temperature. At each temperature the sample was brought to thermal equilibrium before the measurement.

The spin relaxation processes of $Co_3Sn_2S_2$ at selected temperatures were systematically studied by measuring the ZFC ac susceptibility for different magnetic fields in a frequency range of five orders of magnitude from 0.01 to 1000 Hz.

2.3.5 Longitudinal and transverse resistivities

For further confirmation of previously reported transport properties using polycrystalline samples of Co-shandites, the temperature dependences of the electrical resistivity at zero magnetic fields were measured in a temperature range of 4 – 300 K by employing the conventional four-probe method using pellets sintered from powders.

The in- and out-of-plane longitudinal electrical resistivity at zero magnetic fields of well-polished single crystals were successively measured via the Van der Pauw and the modified Montgomery method, respectively[140,141]. The crystal settings for resistivity measurements are shown in Fig. 2.5. The in-plane and out-of-plane electrical resistivity in these settings are given by Eqs. (2.2) and (2.3), respectively:

$$\rho_{ab} = \frac{\pi d}{\ln 2}\frac{R_1 + R_2}{2} f\left(\frac{R_1}{R_2}\right), \tag{2.2}$$

$$\rho_c = \rho_{ab}\left[A\left(\frac{R_3}{R_4}\right)\frac{l}{d}\right]^2, \quad A\left(\frac{R_3}{R_4}\right) \cong \frac{1}{2}\left[\frac{1}{\pi}\ln\frac{R_3}{R_4} + \sqrt{4 + \left[\frac{1}{\pi}\ln\frac{R_3}{R_4}\right]^2}\right], \tag{2.3}$$

where l and d are the samples dimensions shown in Fig. 2.5 and R_i is the resistance given from the shown voltage V_i and current I_i by Ohm's law. $f(R1/R2)$ in Eq. (2.2) is the Van der Pau factor[16]. The electrical resistivity at zero magnetic field was measured by using a Cryomini refrigerator (Iwatani Co. Ltd.)

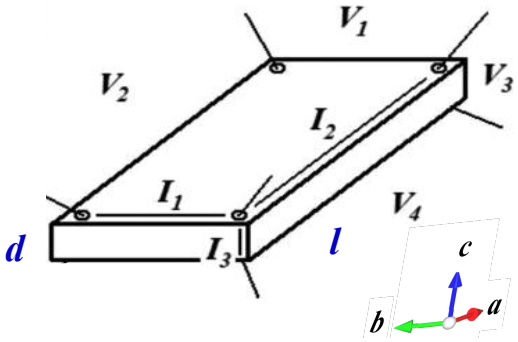

Fig. 2.5: Van der Pauw and the modified Montgomery setting

The transverse in-plane resistivity (Hall resistivity) and longitudinal in-plane resistivity (magnetoresistance) were simultaneously measured by applying the current in the *ab*-plane of the Van der Pauw setting in Fig 2.5 in magnetic fields up to 5 T applied parallel to *c*-direction. Low currents (around 1 mA) were used to avoid the thermo-electric voltages emerge and add to the intrinsic high resistances of the sample. The transverse and longitudinal resistivities were measured using a complementary homemade helium-4 refrigerator with a superconducting magnet of fields up to 5 T, displayed in Fig. 2.4(b).

2.3.6 Specific heat

The heat capacity of $Co_3Sn_{2-x}In_xS_2$ ($0 \leq x \leq 2$) was measured at zero magnetic field down to 2 K, by using crystalline samples of different In concentrations (x). The measurements were performed by the relaxation method using PPMS (Quantum Design), installed in the laboratory of Solid State Chemistry and Physics, Graduate School of Science, Kyoto University, Japan.

CHAPTER 3

3 Crystal Growth and Structure of $Co_3Sn_{2-x}In_xS_2$ and $Co_{3-y}Fe_ySn_2S_2$

3.1 Motivations and Purpose

The exotic magnetic and transport properties of Co-based shandites predicted by band structure calculations have been hitherto investigated at magnetic fields above 1kOe using polycrystalline solid solution samples[83,101,114,116,127], as introduced in chapter 1. No experiment using single crystals of the Co-shandite solid solutions had been reported. In this chapter the firstly successful growth of well-characterized single crystals of the Co-shandite solid solutions of $Co_3Sn_{2-x}In_xS_2$ ($0 \leq x \leq 2$) and $Co_{3-y}Fe_ySn_2S_2$ ($0 \leq y \leq 0.5$) by both flux- and a modified-Bridgman methods is detailed. The obtained crystals are useful to study the anisotropy in the magnetic and transport properties and further expected magneto-transport properties of great interest for these layered Co-shandite of 2D Co-kagomé lattice.

3.2 Outline

The optimum conditions to synthesize large crystals of high quality, as indicated by characterization results, are detailed above in the sect. 2.2 of chapter 2. The grown crystals were characterized using the powder XRD, SEM-WDS and magnetization measurements. The results of crystal growth and SEM-WDS are presented in subsect. 3.3.1 of this chapter. The crystal structure of the grown Co-shandites crystals investigated by powder XRD and the structure parameters refinement using the Rietveld analysis of the measured XRD patterns are presented in the subsect. 3.3.2. Section 3.4 concludes the characterization results.

3.3 Results and Discussion

3.3.1 Crystal growth and chemical composition

Single crystals of $Co_3Sn_{2-x}In_xS_2$ were successfully grown in the whole range of x ($0 \leq x \leq 2$) by a flux method[128–132] and furthermore by the modified Bridgman method[120] . Plate-shaped crystals up to ~ 7 mm in size were obtained by the flux-growth, as shown in Fig. 3.1 (a). However, large crystals of about ~ 5 cm in length and 1 cm in diameter showing cleavage planes, as indicated by WDS results displayed below, were successfully obtained by the Bridgman method, as seen in Fig. 3.1(d).

Although $Fe_3Sn_2S_2$ is unstable phase, single crystals of the shandite-phase solid solution $Co_{3-y}Fe_ySn_2S_2$ were successfully grown out of Sn self-flux with the starting Fe concentration up to $x_{nom} = 0.7$ in the molten. We found that single crystals of the shandite-phase are not grown with higher starting Fe concentrations. Instead, other phases such as SnS sheets, CoSn rods, FeS and $CoSn_2$ were found to be synthesized. It is consistent with a recent work to synthesis polycrystalline $Co_{3-y}Fe_ySn_2S_2$, where large amounts of by-products were found for $x_{nom} > 0.6$[123]. On the other hand, it was difficult to synthesis single crystals of $Co_{3-x}Fe_xSn_2S_2$ from the powders using the Bridgman method of similar conditions of the $Co_3Sn_{2-x}In_xS_2$ crystals synthesis. For that, experimental results that compare the effects of *p*- and *d*-atoms substitutions in $Co_3Sn_{2-x}In_xS_2$ and $Co_{3-y}Fe_ySn_2S_2$, respectively, are henceforward presented for crystals synthesized using the same route, flux-method.

The flux-grown single crystals have a hexagonal sheet shape, see Figs. 2.1(d) and 3.1(a), reflecting the crystal structure. Sn flux is found to remain on the surface of the grown single crystals. To use the grown crystals for further investigations of physical properties of Co-based shandites, mechanical polishing is required to remove the remaining flux on the surface. A back reflection Laue image taken from the large flat plane of $Co_3Sn_2S_2$ single crystal is shown in Fig. 3.1(b). It accords the calculated Laue pattern of the (001) plane under the $R\bar{3}m$ symmetry shown in Fig. 3.1(c), indicating the large flat plane of the grown single crystal is the

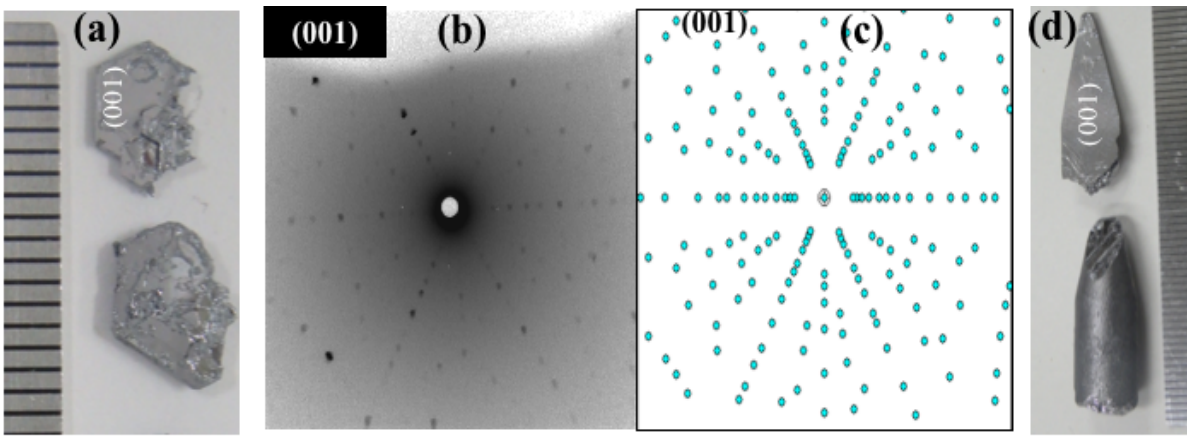

Figure 3.1: (a) Images of grown single crystals of Co-shandites out of Sn flux on a mm scale, (b) experimental back-reflection Laue image taken from the large flat plane of a sheet-shaped single crystal, (c) the corresponding calculated Laue image of the (001) plane, and (d) images of typically grown single crystals of $Co_3Sn_{2-x}In_xS_2$ by the modified Bridgman method on a mm scale, showing (001)-cleavage plane.

c-plane, (001), of the hexagonal crystal. The clear spots in the Laue image indicate high crystalline quality of the grown crystals. The same patterns were obtained from the cleavage planes of the crystals synthesized by Bridgman method.

Chemical compositions of the grown crystals of $Co_3Sn_{2-x}In_xS_2$ and $Co_{3-y}Fe_ySn_2S_2$ were measured by WDS and are listed in Tables 3.1 and 3.2, respectively. The homogeneous compositions of the grown crystals were confirmed by measuring the composition for each crystal at several locations on the surface. The listed compositions were obtained by averaging the WDS data for each crystal of $Co_3Sn_{2-x}In_xS_2$ and $Co_{3-y}Fe_ySn_2S_2$ and were normalized by (Sn+In) and (Co + Fe) concentrations to 2 and 3, respectively.

In $Co_3Sn_{2-x}In_xS_2$, we note that the measured Co and S concentrations are in the ranges of 2.96 ± 0.08 and 1.97 ± 0.08, respectively, and in $Co_{3-y}Fe_ySn_2S_2$ the measured Sn and S concentrations in the solid solution are of 2.00 ± 0.06 and 1.90 ± 0.09, respectively, indicating that mostly stoichiometric single crystals were successfully synthesized. Figure 3.2 shows a comparison of the actual In concentration to nominal one in the solid solution crystals $Co_3Sn_{2-x}In_xS_2$. The actual In concentration, except high In-rich crystals, is approximately two thirds of the starting concentration used in the molten.

The actual Fe-concentration y is higher than the nominal y_{nom} for the low Fe-concentration crystals, whereas, actual y is saturated at about 0.5 for $y_{nom} > 0.5$. The maximum Fe concentration in the grown $Co_{3-y}Fe_ySn_2S_2$ crystals out of Sn self-flux is $y = 0.53$. It is

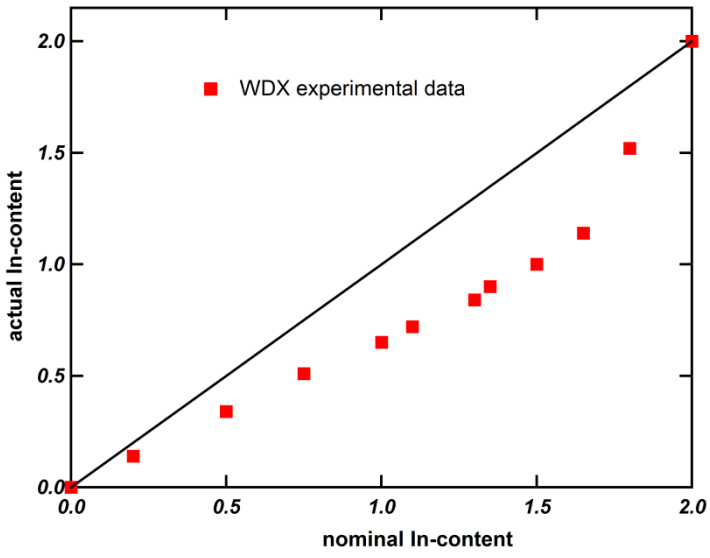

Figure 3.2: Actual concentrations of In versus starting compositions for preparation of $Co_3Sn_{2-x}In_xS_2$ single crystals.

Table 3.1. Flux used for crystals growth out of as well as average chemical configuration based on WDS measurements for $Co_3Sn_{2-x}In_xS_2$ single crystals. Actual x considered is that when (In+Sn) is normalized to 2.

Nominal x	Flux	Chemical configuration	Actual x
0.00	Sn	$Co_{2.87}Sn_2S_{1.97}$	0.00
0.20	$Sn_{90}In_{10}$	$Co_{2.96}Sn_{1.86}In_{0.14}S_{1.92}$	0.14
0.50	$Sn_{75}In_{25}$	$Co_{2.92}Sn_{1.66}In_{0.34}S_{1.89}$	0.34
0.75	$Sn_{22.5}In_{13.5}Pb_{52}$	$Co_{2.95}Sn_{1.49}In_{0.51}S_{1.92}$	0.51
1.00	$Sn_{18}In_{18}Pb_{52}$	$Co_{3.04}Sn_{1.35}In_{0.65}S_{1.89}$	0.65
1.10	$Sn_{16.2}In_{19.8}Pb_{52}$	$Co_{3.01}Sn_{1.28}In_{0.72}S_{1.93}$	0.72
1.30	$Sn_{12.6}In_{23.4}Pb_{52}$	$Co_{2.90}Sn_{1.16}In_{0.84}S_{1.92}$	0.84
1.35	$Sn_{11.7}In_{24.3}Pb_{52}$	$Co_{2.92}Sn_{1.10}In_{0.90}S_{2.04}$	0.90
1.5	$Sn_9In_{27}Pb_{52}$	$Co_{2.96}Sn_{1.00}In_{1.00}S_{1.97}$	1.00
1.65	$Sn_{6.3}In_{29.7}Pb_{52}$	$Co_{3.00}Sn_{0.86}In_{1.14}S_{1.92}$	1.14
1.80	$Sn_{3.6}In_{32.4}Pb_{52}$	$Co_{2.88}Sn_{0.48}In_{1.52}S_{1.90}$	1.52
2.00	In	$Co_{2.94}In_{2.00}S_{1.95}$	2.00

Table 3.2: The used flux; chemical configuration and actual Fe concentration based on WDS measurements for the grown $Co_{3-y}Fe_ySn_2S_2$ crystals.

Nominal y	Flux	Chemical configuration	Actual y
0.00	Sn	$Co_3Sn_{2.09}S_{2.06}$	0.00
0.10	Sn	$Co_{2.86}Fe_{0.14}Sn_{2.01}S_{1.83}$	0.14
0.25	Sn	$Co_{2.61}Fe_{0.39}Sn_{1.96}S_{1.81}$	0.39
0.50	Sn	$Co_{2.51}Fe_{0.49}Sn_2S_{1.84}$	0.49
0.60	Sn	$Co_{2.51}Fe_{0.49}Sn_{2.06}S_{1.99}$	0.49
0.70	Sn	$Co_{2.47}Fe_{0.53}Sn_{2.05}S_{1.94}$	0.53
0.75	Pb	$Co_{2.68}Fe_{0.32}Sn_{1.96}S_{1.83}$	0.32
1.00	Pb	$Co_{2.51}Fe_{0.49}Sn_2S_{1.84}$	0.29

quantitatively consistent with the solubility limit of $y \sim 0.6$ in the polycrystalline sample at ambient pressure. By using Pb flux, the shandite-phase crystals were grown with the starting Fe concentration up to $y_{nom} = 1$, however, the actual Fe-concentration was found to be largely reduced as shown in Table 3.2.

3.3.2 Powder X-ray diffraction and crystal structure analysis

The crystal structure of the grown Co-shandites single crystals synthesized by both flux- and the modified Bridgman method, as well as for the prepared polycrystalline samples, was investigated by powder XRD and the structure parameters were refined using the Rietveld analysis of the measured XRD patterns. Powder samples prepared by crushing single crystals were used. Figure. 3.3 compares the observed and calculated powder XRD patterns of $Co_3Sn_2S_2$ single crystals grown out of Sn-flux to that of crystals grown from a polycrystalline $Co_3Sn_2S_2$-molten by the modified Bridgman method. Although small traces of the binary compound $CoSn_2$ appear as a by-product in the observed patterns of the flux-grown $Co_3Sn_2S_2$ crystals, the Bridgman crystals show the solitary shandite phase of $Ni_3Pb_2S_2$-structure. However, the observed by-products in the flux-crystals patterns only exist in the remaining flux on the crystals surface, as described below.

(i) XRD results of $Co_3Sn_{2-x}In_xS_2$ single crystals

Figure. 3.4 shows the observed and calculated powder XRD patterns of $Co_3Sn_{2-x}In_xS_2$ flux-grown crystals with selected In concentrations at room temperature. The main phase of the obtained crystals for all In concentrations is the shandite. Small traces of the used flux, In and Pb, emerge in those of the $Co_3In_2S_2$ and crystals of the solid solutions due to the tendency of these fluxes to coat crystals grown out of them[22]. Removing the excess flux from the surface of grown crystals is necessary to avoid extrinsic contributions in further study, which is incomplete here to obtain precise data sufficient for the Rietveld analysis using the limited size flux-grown crystals. In order to confirm that the observed by-products only exist in the remaining flux on the surface of crystals, the powder XRD pattern using a well-polished $Co_3Sn_2S_2$ crystal was examined, which is shown in the inset of the lowest panel of Fig. 3.4 and is compared to the pattern shown in the main figure. The absence of $CoSn_2$ traces after polishing the crystals surface is clearly found.

The lattice parameters, *M* (Sn or In) occupancies at *M*1- and *M*2-sites, and atomic position parameter of the S-site (0,0,*z*), were refined by the Rietveld method for the selected In concentration samples shown in Fig. 3.4. For the other concentration samples, only the lattice parameters were refined. The observed diffraction patterns are reasonably fitted using the structure parameters of the $Co_3M_2S_2$ shandite structure of the space group $R\bar{3}m$ with considering the extrinsic phases mentioned above. In our analysis, the *M*-occupancies were refined with the initial condition of the completely random occupations. The best fitting results

are shown by blue solid lines in Fig. 3.4. The low *R*-factors and goodness-fit-indicator *S* demonstrate the satisfactory refinements. The refinement results are summarized in table 3.3.

The lattice parameters, *a* and *c*, plotted against In concentration *x* are shown in Fig. 3.5. The concentration dependences of *a* and *c* are anisotropic and do not obey the Vegard's law of solid solutions. *c* increases monotonically with *x*, whereas *a* shows a linear decrease until *x* ~ 0.8 and almost remains constant for a higher In concentration region. Our results are in good

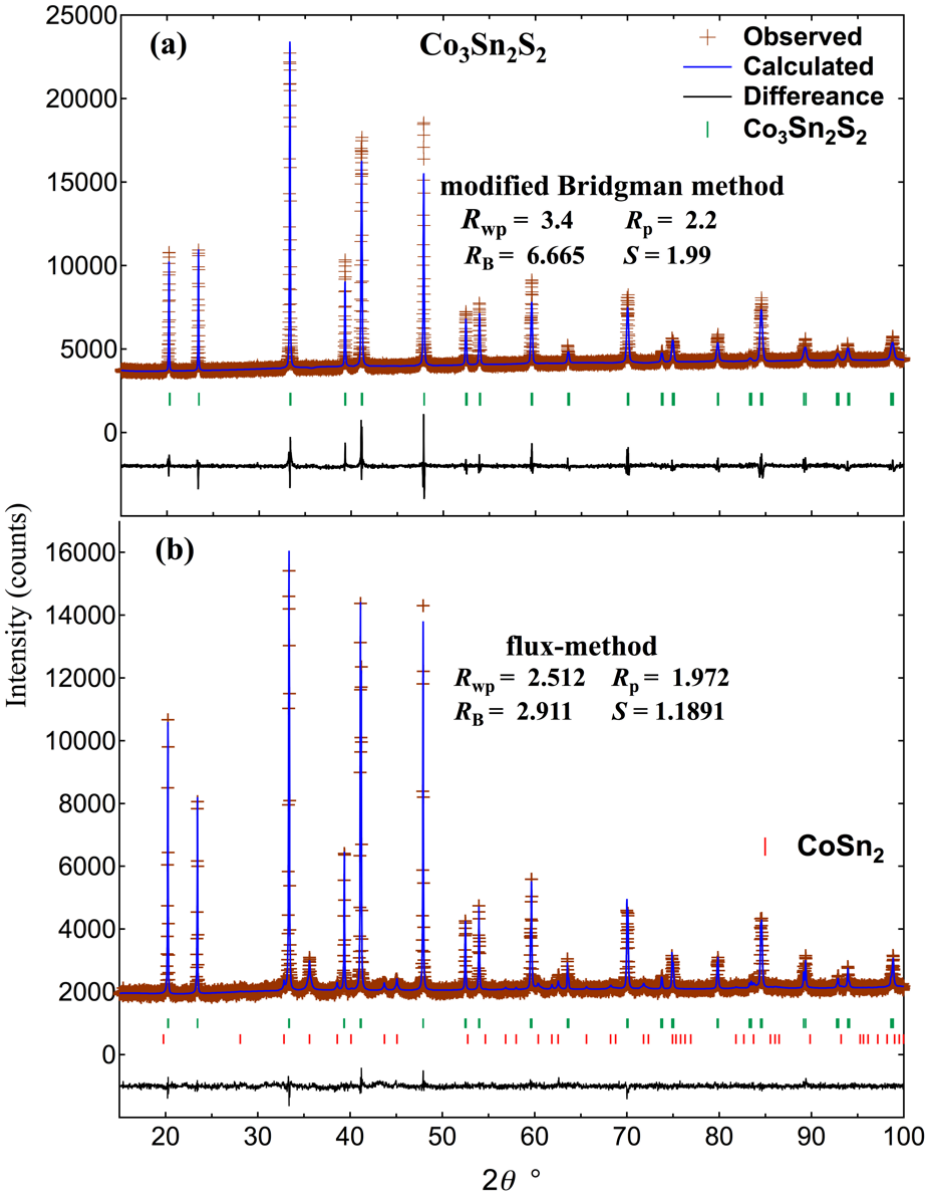

Figure 3.3: Powder XRD diffraction patterns measured at RT for $Co_3Sn_2S_2$ single crystals synthesized by (a) the modified Bridgman method and (b) the flux-method. Observed, refined patterns using the Rietveld method and differences between them are shown in crosses, blue solid lines and black solid lines, respectively. Bragg reflection angles are indicted as vertical bars. The reliability *R*-factors as well as the goodness-fit-indicator *S* are indicated for each pattern.

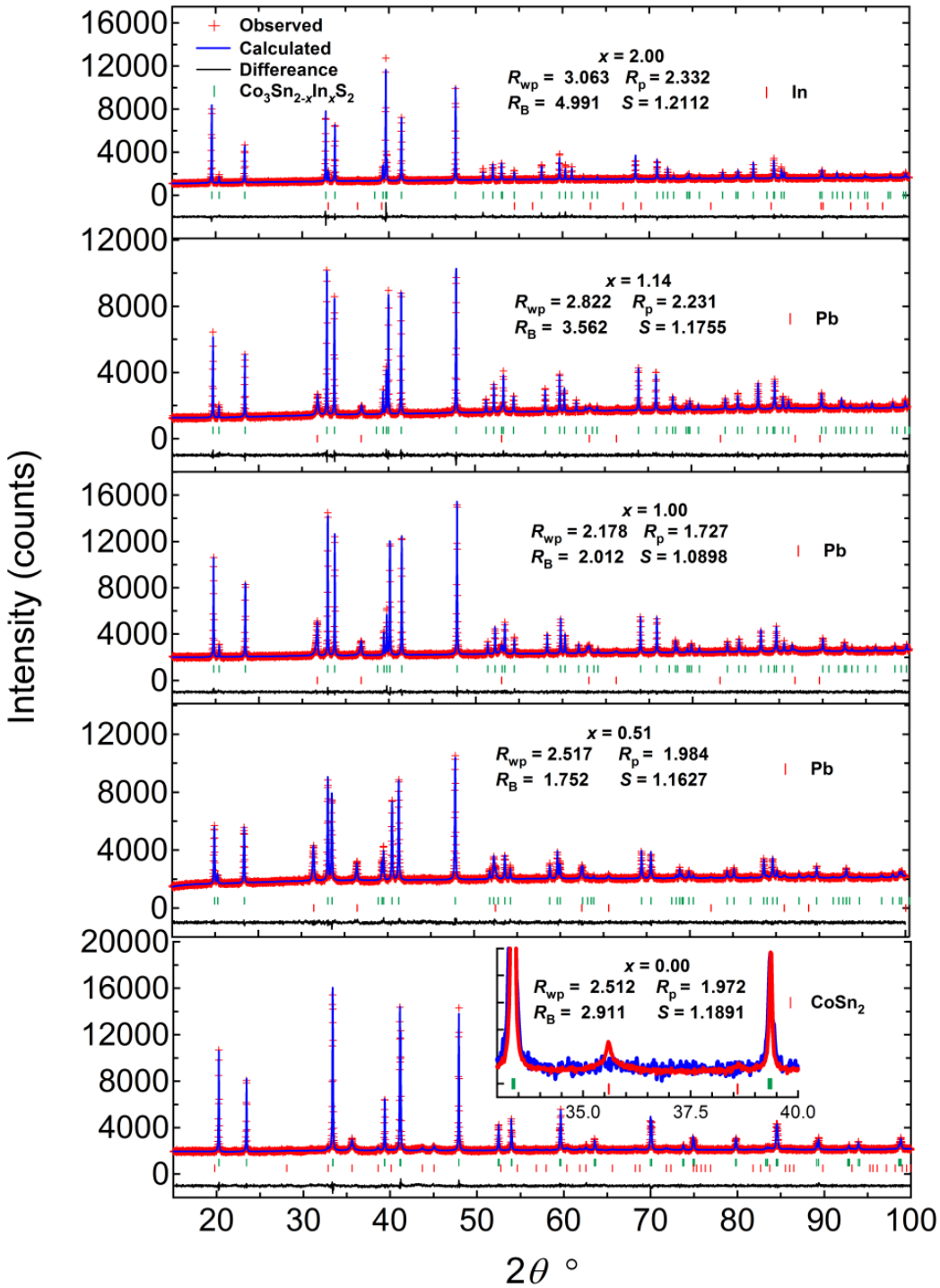

Figure 3.4: Powder XRD diffraction patterns of $Co_3Sn_{2-x}In_xS_2$ single crystals measured at RT. Observed, refined patterns using the Rietveld method and differences between them are shown in crosses, blue solid lines and black solid lines respectively. Bragg reflection angles are indicted as vertical bars. The reliability *R*-factors as well as the goodness-fit-indicator *S* are indicated for each pattern. Inset in the lowest panel shows the absence of the highest peak of $CoSn_2$ in normalized patterns of well-polished single crystals of $Co_3Sn_2S_2$, blue solid lines (not enough for refinement) compared to the patterns of single crystals of $Co_3Sn_2S_2$ used in the Rietveld analysis (red solid lines).

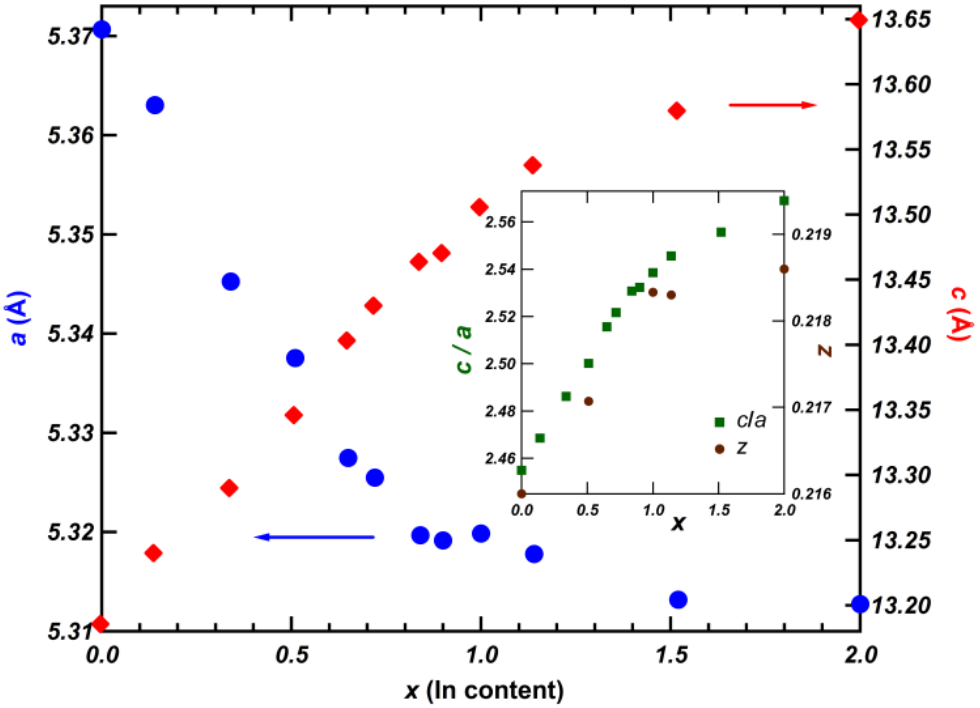

Figure 3.5: Composition dependence of lattice parameters *a* (on left) and *c* (on right) as well as *c*/*a* ratio and atomic position parameter of the S-site *z* (shown in the inset on left and right respectively) of $Co_3Sn_{2-x}In_xS_2$ single crystals.

agreement with previously reported results using polycrystalline samples[101,117,127], if considering of the reduction of the actual In concentration from the nominal ones in the grown single crystals (sec. 3.3.1). In the polycrystalline samples, the change of the concentration dependence of *a* was found around $x = 1.0$. Probably, the actual In concentration of polycrystalline samples was also lower than the nominal one, as well as our single crystals.

The inset of Fig. 3.5 shows the ratio of *c* to *a* against *x*, indicating a monotonic enhancement of the trigonal distortion by the In-substitution. The trigonal distortion enhanced by the In-substitution was explained based on the *ab* initio calculations by the different bonding-contributions of Sn- and In-5p states[117]. The slope of the increase of *c*/*a* apparently changes around $x \sim 0.8$ as well as the concentration dependence of *a*. The estimated atomic bond lengths are listed in table 3.3. Corresponding to the anisotropic behavior of lattice parameters against *x*, the bond lengths between atoms of different layers, *d*(Co-*M*1), *d*(*M*2-S), and *d*(*M*1-*M*2), increase with the In concentration, while those within the kagomé layers, *d*(Co-Co) = *d*(Co-*M*2) = *a*/2, shrink first and then remain almost constant. The position parameter of the S site, *z*, exhibits a similar behavior to *c*/*a* as shown in the inset of Fig. 3.5, and consequently, *d*(Co-S) shows a non-monotonic behavior with a minimum around $x \sim 1.0$. The

bond lengths between Co and *M* atoms are almost equal, *d*(Co-*M*1) ≃ *d*(Co-*M*2), in the pure Sn compound, and split to *d*(Co-*M*1) > *d*(Co-*M*2) by the In-substitution as a manifestation of the enhancement of the trigonal distortion. It suggests that the electronic state of the Co-shandite changes from 3D- to 2D-like one by the In-substitution. The anisotropy of the electronic transport properties should be investigated using the grown single crystals.

The change of the In concentration dependence of the lattice parameter *a* suggests a site-preference of In atoms among the *M*1- and *M*2-sites. Indeed, the refined In occupancies at the *M*1- and *M*2-sites, g_{In1} and g_{In2}, listed in table 3.3 are inconclusive to indicate that In-atoms may occupy the *M*1-site in preference to the *M*2-site or vice versa. According to reported band calculations[114], the site preference of Sn/In atoms affects the electronic properties of $Co_3Sn_{2-x}In_xS_2$ significantly and the metal-semiconducting transition related with the Sn-In ordering is predicted. Because XRD is not sensitive enough to distinguish the Sn and In atoms, the refined Sn/In occupancies have large ambiguity and the site-preference of In atoms is not conclusive. Further investigations by neutron diffraction and NMR experiments, for instance, would be

Table 3.3: Lattice parameters, atomic position parameters, occupancy *g* of Sn and In atoms and atomic bond lengths of $Co_3Sn_{2-x}In_xS_2$ refined by the Rietveld analysis of XRD patterns at RT using the RIETAN-FP software. The shandite phase with space group $R\bar{3}m$ and atomic positions of Co at 9*e*(½,0,0), *M*1 at 3*b*(0,0, ½), *M*2 at 3*a*(0,0,0) and S at 6*c*(0,0,*z*) is assumed. Complete disorder of Sn and In is initially considered in the refinement (see text).

	***x* = 0.0**		***x* = 0.51**	***x* = 1.0**	***x* = 1.14**	***x* = 2.0**
	Bridgman-	flux-method				
a	5.3689(1)	5.37066	5.33754(8)	5.31986(6)	5.31779	5.31273
c	13.1747(2)	13.1843(1)	13.3448(2)	13.5045(1)	13.5367(0)	13.6419(1)
z	0.2134(3)	0.2160(2)	0.2170(3)	0.2183(2)	0.2183(3)	0.2186(2)
g_{In1}*	0.0	0.0	0.4103	0.1121	0.5358	1.0
g_{In2}*	0.0	0.0	0.109(6)	0.887(1)	0.604(8)	1.0
g_{Sn1}*	1.0	1.0	0.5897	0.8879	0.4642	0.0
g_{Sn2}*	1.0	1.0	0.8903	0.1121	0.3958	0.0
***d*(Co-*M*1) Å**	2.68769	2.68927	2.70572(3)	2.72475(2)	2.729(5)	2.7426(9)
***d*(Co-*M*2/Co) Å**	2.68445(3)	2.68533	2.66877(4)	2.65993(3)	2.659(4)	2.65636
***d*(Co-S) Å**	2.213(3)	2.19015	2.187(3)	2.184(3)	2.187(4)	2.186(3)
***d*(*M*2-S) Å**	2.812(4)	2.84782	2.897(4)	2.948(3)	2.955(7)	2.990(4)
***d*(*M*1-*M*2) Å**	3.79866(3)	3.80079(3)	3.80043(3)	3.80782(2)	3.810(5)	3.8181(7)

* g_{In1} and g_{In2} are occupancies of In at *M*1 (3*b*) and *M*2 (3*a*) sites while g_{Sn1} and g_{Sn2} are occupancies of Sn at *M*1 (3*b*) and *M*2 (3*a*) sites, respectively.

useful. Recently reported powder neutron diffraction results have revealed that indium preferentially occupies the interlayer site (*M*1) over the alternative intralayer site (*M*2)[83].

(ii) XRD results of $Co_{3-y}Fe_ySn_2S_2$ single crystals

The crystal structure effects of the Fe-substituted $Co_{3-y}Fe_ySn_2S_2$ system is investigated by powder XRD. The observed diffraction patterns are fitted using the structure parameters of the $Co_3Sn_2S_2$ shandite structure of $R\bar{3}m$ symmetry. The observed and calculated powder XRD patterns of $Co_{3-y}Fe_ySn_2S_2$ at room temperature with representative Fe concentrations are shown in Fig. 3.6. Powder XRD patterns exhibit the shandite-phase as the main phase of the obtained crystals for all Fe concentrations. Again relative small traces of the used flux as well as by-products such as $CoSn_2$, CoSn and/or SnS, exist only on the crystals surface, emerge in the XRD patterns.

The lattice parameters and atomic position parameter of the S-site, *z*, refined by the Rietveld method are listed in table 3.4, as well as lengths of *T* (Co/Fe) related bonds for all Fe concentrations. In the analysis, we considered the extrinsic phases of the by-products mentioned above. The Co/Fe occupancies were confined based on the WDS results. The best fitting results are shown by red solid lines in Fig. 3.6. The low reliability *R*-factors and goodness-fit-indicator *S* indicate the satisfactory refinement for each Fe-concentration sample.

Fig. 3.7 shows the refined lattice parameters, *a* and *c*, plotted against Fe concentration, *y*. The unit cell volume, *V*, as well as the *c* to *a* ratio against *y* are shown in the inset. The error bars of both *V* and *c*/*a* are in the range of the representative symbols. Whereas *a* decreases upon Fe-substitution, *c* and *V* increase monotonically with *y*. The lattice parameters show linear concentration dependences and well obey the Vegard's law of solid solutions. Our results are qualitatively in agreement with the previously reported results using polycrystalline samples obtained by HP and HT technique[123], and also agree well with the theoretically predicted lattice parameters of the hypothetical compound $Fe_3Sn_2S_2$ of shorter *a* (5.343 Å) and longer *c* (13.479 Å)[126]. It should be noted that the variation of the lattice parameters of our single crystals is rather steeper than that of the polycrystalline samples. The difference in the Fe-concentration dependences between our results and previous ones using polycrystalline samples are more clearly found in the magnetic properties described in chapter 4.

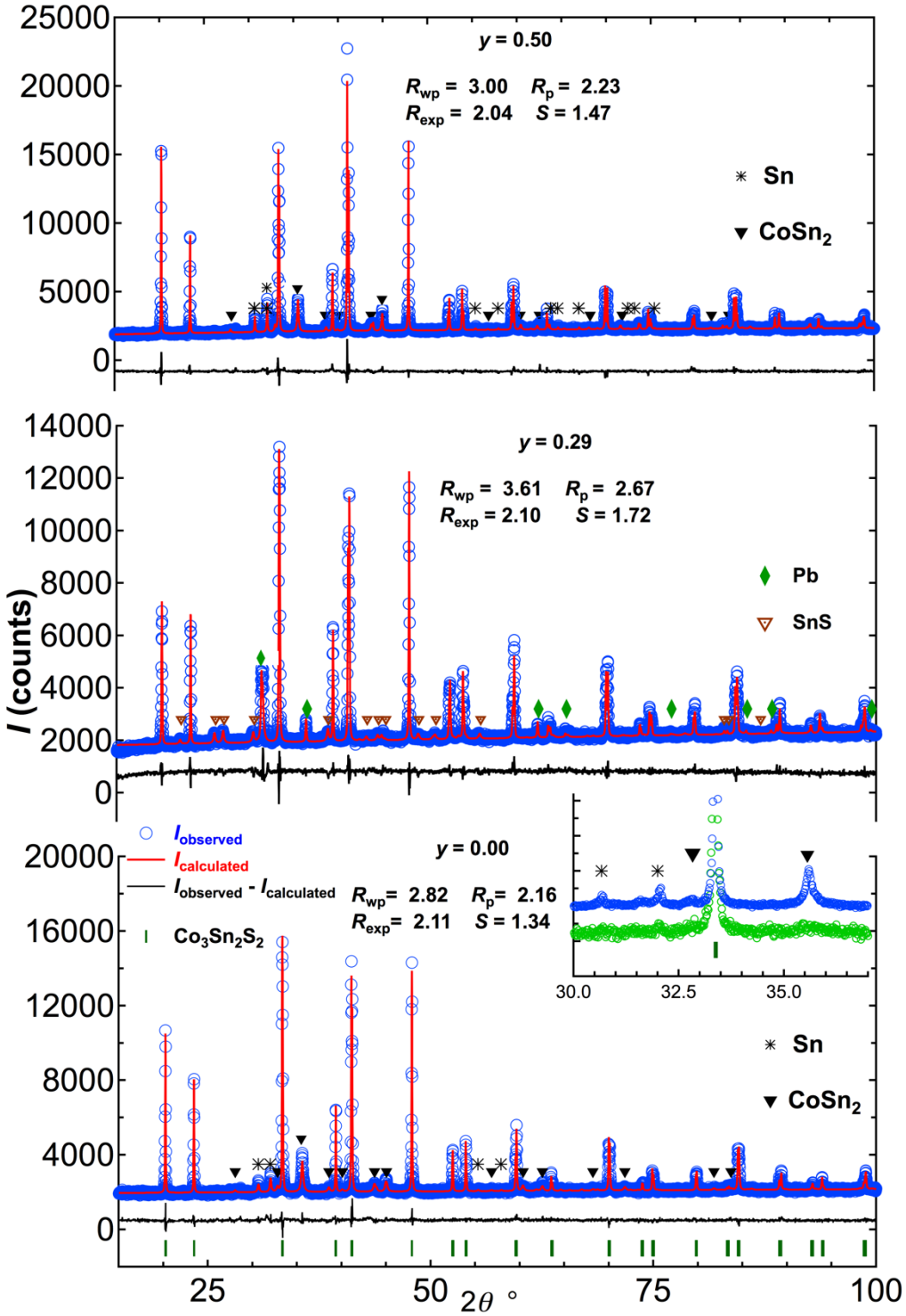

Figure 3.6: Powder X-ray diffraction patterns of $Co_{3-y}Fe_ySn_2S_2$ single crystals with representative y measured at room temperature. Observed, refined patterns using the Rietveld method and differences between them are shown in open circles, red solid lines and black solid lines, respectively. Bragg reflection angles of $Co_3Sn_2S_2$ phase are indicted as vertical bars in the lowest panel. The reliability R-factors, as well as the goodness-fit-indicator S, for each pattern are indicated. Inset shows the absence of the by-products peaks in a normalized patterns of well-polished crystals of $Co_3Sn_2S_2$ (green circles) compared to the patterns used in the Rietveld analysis shown in the main figure (blue circles).

The increase of the ratio of c to a against y indicates an enhancement of the trigonal distortion by the Fe-substitution. Indeed, corresponding to the opposite behavior of lattice parameters against y, the interlayer $d(T\text{-Sn1})$ bond length increases while $d(T\text{-Sn2}) = d(T\text{-}T) = a/2$, within the kagomé layers, shrinks upon Fe-substitution. The bond lengths between T and Sn atoms at the two different sites Sn1 and Sn2 which are almost equal $d(T\text{-Sn1}) \simeq d(T\text{-Sn2})$ for $y = 0$, slightly split to $d(T\text{-Sn1}) > d(T\text{-Sn2})$ by the Fe-substitution as a manifestation of the enhancement of the trigonal distortion.

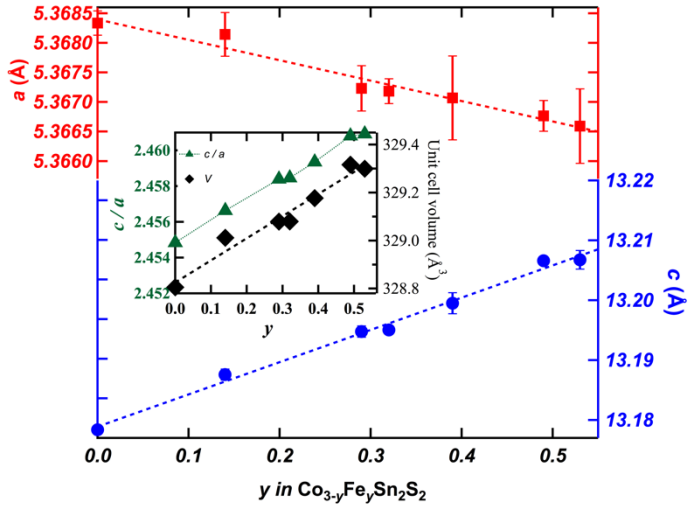

Figure 3.7: Fe concentration dependence of the lattice parameters a and c. Inset shows the c/a ratio (on left) and unit cell volume (on right) against x of $Co_{3-y}Fe_ySn_2S_2$ single crystals.

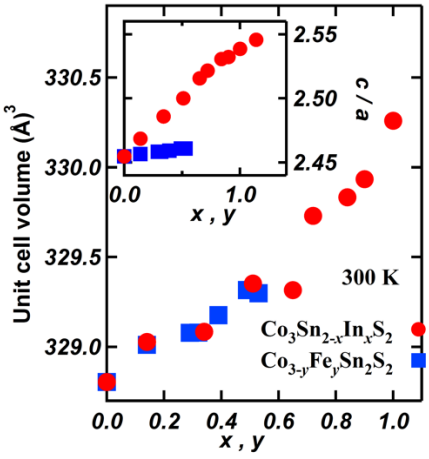

Fig. 3.8: Lattice effects of In- and Fe-substitution on the unit cell volume of $Co_3Sn_2S_2$ and its c to a ratio (inset).

Table 3.4: Lattice parameters, atomic position parameter of sulfur, z, and atomic bond lengths of $Co_{3-y}Fe_ySn_2S_2$ refined by the Rietveld analysis of PXRD patterns at room temperature using the TOPAS software. The shandite phase with space group $R\bar{3}m$ and atomic positions of Co/Fe at 9e(½,0,0), Sn1 at 3b(0,0, ½), Sn2 at 3a(0,0,0) and S at 6c(0,0,z) is assumed (see text).

y	a /Å	C /Å	z	d(T-Sn1) /Å	d(T-Sn2/T) /Å	d(T-S) Å
0.00	5.3683(2)	13.1783(5)	0.2161(3)	2.68807	2.68417	2.188(3)
0.14	5.3681(4)	13.18758(9)	0.2134(5)	2.68958	2.68439	2.215(4)
0.29	5.3672(4)	13.1947(9)	0.2155(3)	2.69012	2.68361	2.195(3)
0.32	5.3671(2)	13.1950(5)	0.2142(2)	2.69016	2.68359	2.206(2)
0.39	5.3670(7)	13.199(2)	0.2167(3)	2.69074	2.68353	2.184(2)
0.49	5.3667(3)	13.2065(6)	0.2161(3)	2.69169	2.68341	2.190(3)
0.53	5.3665(6)	13.206(2)	0.2170(3)	2.69165	2.6833	2.182(3)

It should be noted that the increase of c/a, equivalently the further trigonal distortion, by the Fe-substitution is much smaller than that caused by the In-substitution[83,111,117]. Fig. 3.8 compares the structural effects of the two substitutions. The unit cell volume shows identical *x*- and *y*- dependences, however, large enhancement in *c/a* is observed for In-substitution. The DFT calculations predicted the energy gap opening and the significant enhancement of the trigonal distortion in the In-substituted systems caused by the In-Sn ordering: the In atoms occupy only the interlayer Sn1-site[114]. Indeed, the partial ordering of the In-Sn atoms, the prefer of In- substitution to the Sn1-site, was found by a recent neutron diffraction experiment[142]. On the contrary, a weak further structure distortion was predicted in the Fe-substituted systems[126]. In both systems, the main effect of the substitution is a reduction of electron number: one electron in 3*d*- and 5*p*-orbitals are reduced in the Fe- and In-substituted systems, respectively. The enhancement of the trigonal distortion in the In-substituted $Co_3Sn_{2-x}In_xS_2$ was explained by the anisotropy of the In 5*p*-orbitals in DFT model calculations[117], which can also explain the smallness of the enhancement of trigonal distortion in $Co_{3-y}Fe_ySn_2S_2$.

3.4 Conclusion

Single crystals of the shandite solid solutions $Co_3Sn_{2-x}In_xS_2$ ($0 \leq x \leq 2$) and $Co_{3-y}Fe_ySn_2S_2$ ($0 \leq y \leq 0.5$) of stacked metallic layers, consist of Co/Fe kagomé network permeated by Sn/In triangular lattice, have been successfully grown by a flux-method. Much larger single crystals of $Co_3Sn_{2-x}In_xS_2$ have also been grown by a modified Bridgman technique. The grown crystals were characterized by means of the WDS, Laue X-ray photography and powder XRD measurements. The chemical composition and solubility limit (of Fe in $Co_{3-y}Fe_ySn_2S_2$), structural and magnetic properties observed in the grown single crystals are qualitatively in good agreement with the reported results using polycrystalline samples. The Rietveld analyses of the XRD data exhibits a much smaller enhancement of the trigonal distortion in the Fe-substituted crystals than that in the In-substituted ones, although identical degrees of the corresponding lattice expansion are observed. The different structural effects imply possible variations in the magnetic and the electronic states of $Co_3Sn_{2-x}In_xS_2$ and $Co_{3-y}Fe_ySn_2S_2$.

CHAPTER 4

4 Magnetic Properties I: Quasi-Two-Dimensional Magnetism in Co-based Shandites

4.1 Motivations and Purpose

As low dimensional itinerant electron magnets have received a lot of interest due to the exotic phenomena usually observed near a magnetic instability, the search for new weakly-coupled chain or layered compounds showing that magnetic instability is highly promoted. Co-based shandite of the layered structure described in subsect. 1.4.3 of chapter 1 are candidates of Q2D systems due to their layered crystal structure. Moreover, $Co_3Sn_2S_2$, exhibits a ferromagnetic instability that is controlled by several chemical substitutions and worth investigations for novel phenomena. In this chapter, the Q2D magnetism of the weakly itinerant electron ferromagnets of Co-shandites, $Co_3Sn_{2-x}In_xS_2$ and $Co_{3-y}Fe_ySn_2S_2$, is studied through static magnetization measurement. The phenomenological spin fluctuation theory developed by Takahashi[8,9] can be nicely utilized to discuss the Q2D nature of the magnetic and electronic states of itinerant electron magnets, as introduced in subsect. 1.1.1 of chapter 1. In the theory, the spatial anisotropy of electronic states is considered by introducing a new parameter ε which is the ratio of the effective mass of in-plane and out-of-plane electron motions.

4.2 Outline

The static magnetization results of $Co_3Sn_{2-x}In_xS_2$ and $Co_{3-y}Fe_ySn_2S_2$ of anisotropic magnetic properties are presented and discussed in sect. 4.3. Systematic investigations for the In- and Fe-substitution effects on the magnetism of $Co_3Sn_2S_2$ are presented and discussed here in the two subsects. 4.3.1 and 4.3.2. The magnetization data are analyzed based on the phenomenological spin fluctuation theory developed by Takahashi[8,9] and several spin fluctuation parameters are obtained, as discussed in subsect. 4.3.3. The analytical results clearly indicate strong Q2D nature of magnetism in the Co-based shandites. Sect. 4.4 concludes the magnetic properties of Co-shandites presented in this chapter.

4.3 Results and Discussion

The significance of the electron number to the magnetic stats of $Co_3Sn_2S_2$ indicated previously by DFT calculations and observed using polycrystalline samples, was again emphasized here first by using polycrystalline samples before the measurements using single crystals. Figure 4.1 shows the temperature dependences of M/H of polycrystalline samples of

$Co_3Sn_{2-x}In_xS_2$ ($0 \leq x \leq 2$, x is the nominal concentration initially used) with applied field H = 0.1 T, where M and H are magnetization and applied magnetic field, respectively. In consistent with previous studies, the ferromagnetic order is suppressed by In-substitution and collapses at the nominal concentration of $x \sim 1.0$ in polycrystalline samples.

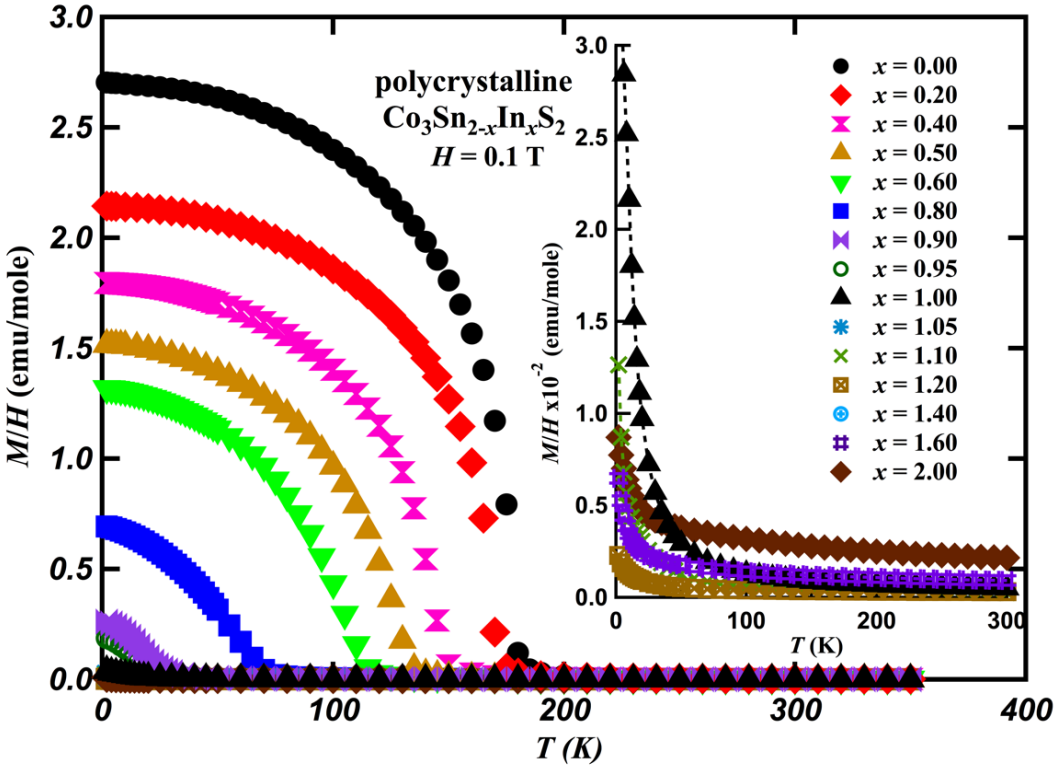

Figure 4.1: Temperature dependences of M/H of polycrystalline samples of $Co_3Sn_{2-x}In_xS_2$ ($0.0 \leq x \leq 2.0$) measured at H = 0.1 T.

4.3.1 Anisotropic magnetic properties

Figure 4.2 shows the temperature dependence of the magnetization M of $Co_3Sn_2S_2$ at two different magnetic fields H applied along and perpendicular to the c-axis. A ferromagnetic transition around $T_C \sim 174$ K (at H = 1 kOe) is clearly observed, as previously reported for single crystals[118,119]. However, T_C shows a field-dependence as seen in the figure for 1 and 10 kOe. Strong axial anisotropy is observed below the transition temperature, where the ratio of the magnetizations along and perpendicular to the c-axis is $M_c/M_{ab} \sim 30$ at H = 1 kOe. The inset shows the temperature dependence of the inverse susceptibility H/M along and perpendicular to the c-axis. Above T_C, the susceptibility shows the Curie-Weiss (CW) type paramagnetic behavior. In contrast to the ferromagnetic state, isotropic magnetic behavior is found in the paramagnetic regime.

The temperature dependences of the magnetization measured by applying a magnetic field of 1 kOe along and perpendicular to the *c*-axis of single crystals of the solid solutions of $Co_3Sn_{2-x}In_xS_2$ and $Co_{3-y}Fe_ySn_2S_2$ are presented in details in Figs. 4.3 and 4.4, respectively. As

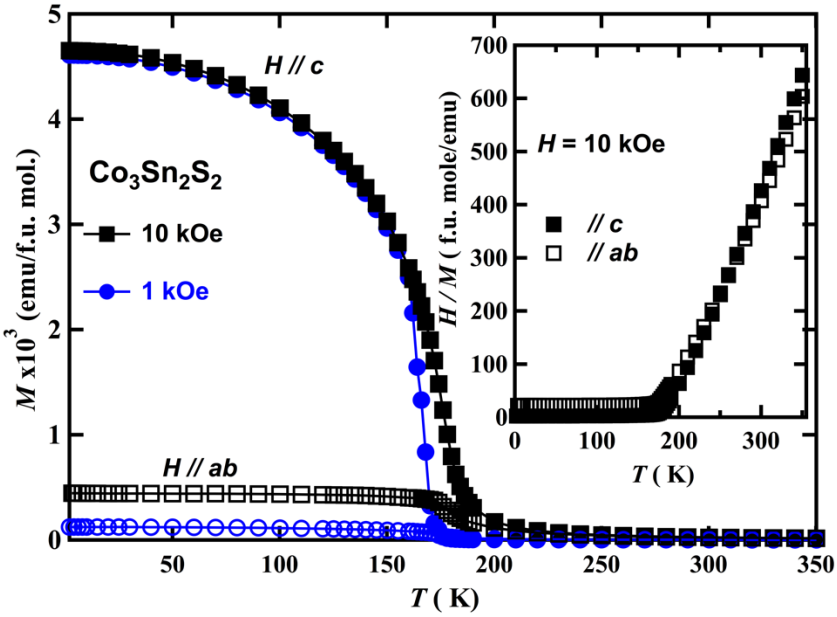

Figure 4.2: Temperature dependences of the magnetization, $M(T)$, of $Co_3Sn_2S_2$ at two different fields, H = 1 and 10 kOe. The closed and open symbols represent the magnetization with applying magnetic field along and perpendicular to the *c*-axis, respectively. The inset shows the inverse susceptibility H/M as functions of T.

presented above for powder samples, the ferromagnetic order is suppressed by In- or Fe-substitutions. In $Co_3Sn_{2-x}In_xS_2$, the ferromagnetic order is collapsed around $x_c \sim 0.8$. The x = 0.84 sample exhibits a divergent behavior of M/H down to 0 K (Fig. 4.3(e)), which is attributed to the ferromagnetic quantum criticality. Above x = 0.84, the low temperature increase of M/H disappears and the Pauli paramagnetic behavior was observed (Fig. 4.3(f)).

On the other hand, in $Co_{3-y}Fe_ySn_2S_2$ solid solution, the ferromagnetic order is also suppressed upon Fe-substitution but is not collapsed until the solubility limit, $y_{max} \sim 0.5$. Nevertheless, similar (virtual) critical concentration ($y_c \sim 0.8$) is expected because of the similarity of the suppression of the ferromagnetism below y_{max} to that in $Co_3Sn_{2-x}In_xS_2$, as shown below by the magnetic phase diagram in Fig. 4.7(a). Details of the suppression of the ferromagnetism will be discussed later.

The magnetization data shows a preservation of the strong magnetic anisotropy in the ferromagnetic regime of $Co_3Sn_{2-x}In_xS_2$ and $Co_{3-y}Fe_ySn_2S_2$. The temperature dependences of the magnetizations along the easy axis and in the *ab*-plane of single crystals of the solid solutions of $Co_3Sn_{2-x}In_xS_2$ and $Co_{3-y}Fe_ySn_2S_2$, are presented in Figs. 4.3(a), (b) and Figs. 4.4(a),

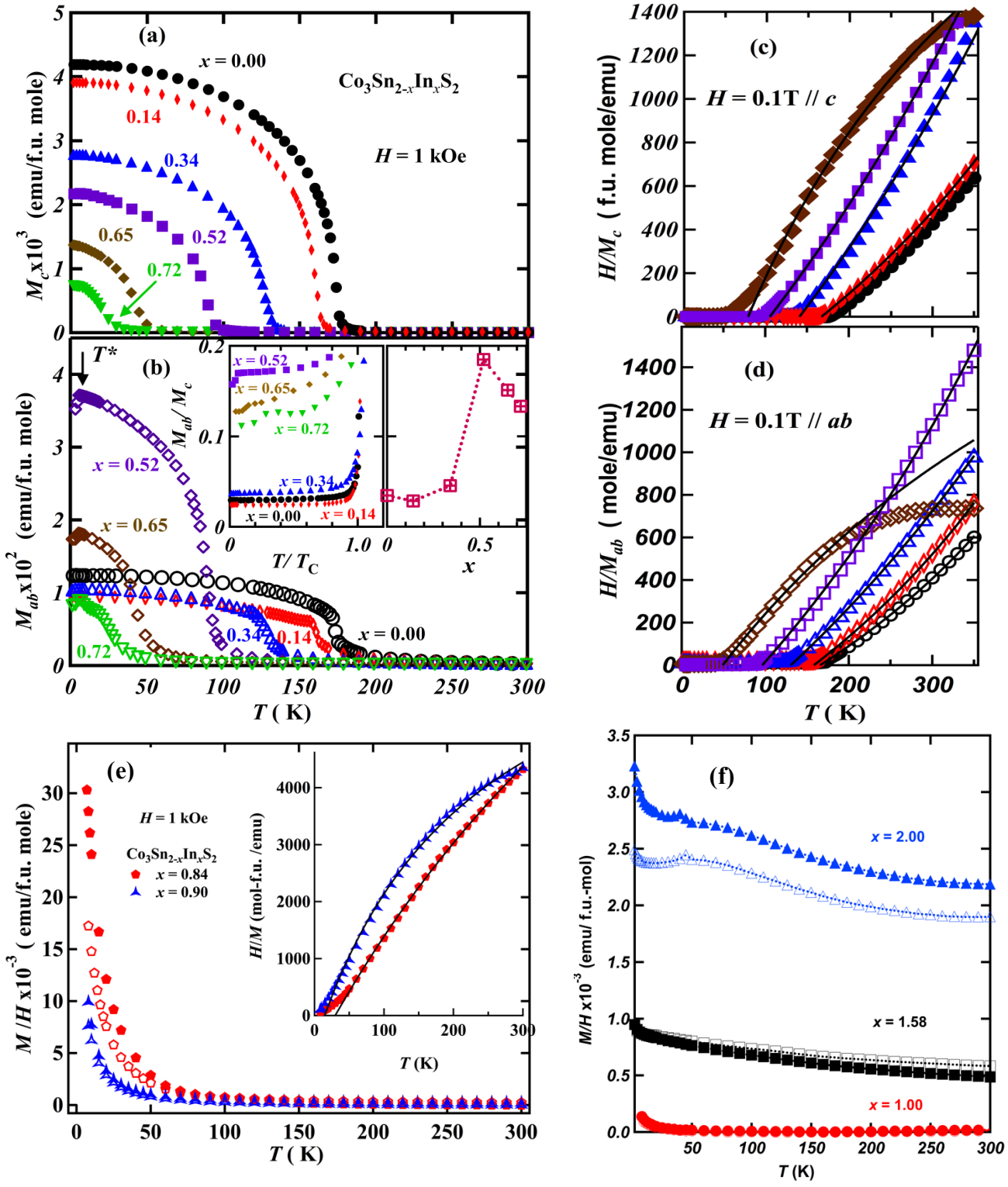

Figure 4.3: Temperature dependences of the static magnetization, $M(T)$, for $Co_3Sn_{2-x}In_xS_2$ of indicated x, at magnetic field H = 1 kOe, presented as $M(T)$ vs. T for (a), (b), (e) and (f) and as $H/M(T)$ vs. T for (c) and (d) for indicated x and H directions. Solid lines in (c) and (d) are fits to Eq. 4.1 in the text. The inset of (b) shows M_{ab} to M_c ratio against the normalized temperature, T/T_C, where T_C is the Curie temperature (left inset) and M_{ab} to M_c ratio against In concentration x (right inset). T^* in (b) indicates the observed anomalies at 7 - 10 K for $0.5 \lesssim x < 0.8$, discussed in chapter 5.

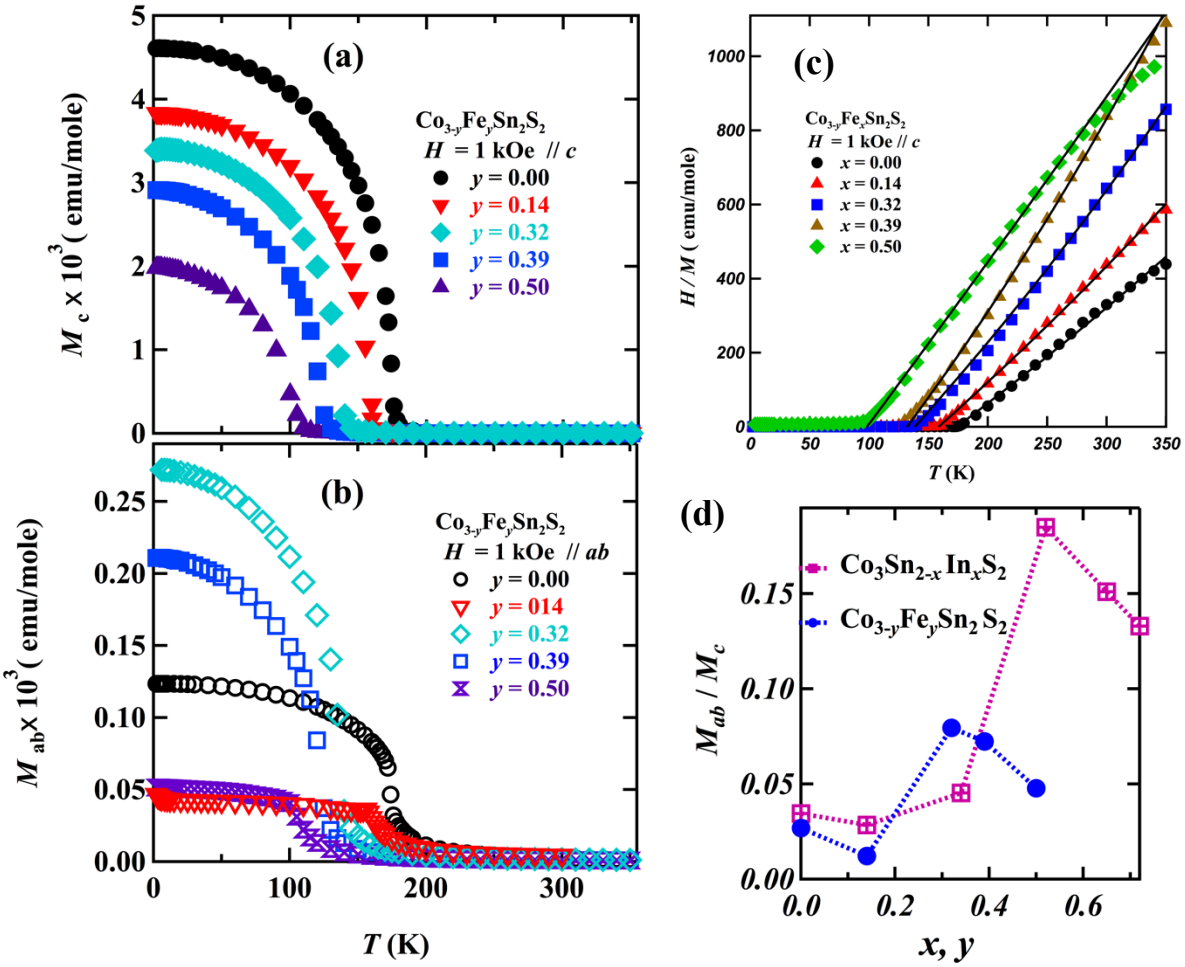

Figure 4.4: Temperature dependences of the static magnetization, $M(T)$, for $Co_{3-y}Fe_ySn_2S_2$ of indicated y, at magnetic field H = 1 kOe, presented as $M(T)$ vs. T for (a) H // c (b) H // ab and (c) as H /$M(T)$ vs. T for H // c. Solid lines in (c) are fits to Eq. 4.1 in the text. (d) Compares M_{ab} to M_c ratio of against x and y in $Co_3Sn_{2-x}In_xS_2$ and $Co_{3-y}Fe_ySn_2S_2$, respectively.

(b), respectively. The magnetization in the easy axis is averagely more than one order of magnitude higher than that in the *ab* plane in both In- and Fe-substituted Co-shandite ferromagnets.

For $Co_3Sn_{2-x}In_xS_2$, while M_c exhibits a monotonic behavior with In-concentration at all temperatures, M_{ab} does not, see Figs. 4.3(b). M_{ab} abruptly increases at $x \sim 0.52$, i.e. the magnetic anisotropy is obviously decreased for $0.5 \lesssim x < 0.8$ as shown in the insets of Fig. 4.3 (b). The anomalously increased in-plane component of the magnetic moment above $x \sim 0.5$ indicates a spin canting from the ferromagnetic order and fluctuating in-plane component as approaching x_c of $Co_3Sn_{2-x}In_xS_2$. Moreover, a cusp anomaly at $T^* \sim 7 - 10$ K are observed in the T-dependence of M_{ab} only for $0.52 \leq x \leq 0.8$ indicating that the fluctuating in-plane component may become fixed and nontrivial spin structure below these low temperatures is aired. These

anomalies in M_{ab}, spin canting and cusps at low temperatures, of $Co_3Sn_{2-x}In_xS_2$ near x_c will be discussed in details in chapter 5. On the other hand, relatively little increase in M_{ab} appears at $0.3 < y \lesssim 0.4$ in $Co_{3-y}Fe_ySn_2S_2$. The T-dependence of M_{ab} to M_c ratios in both systems are compared in Fig. 4.4(d).

Figs. 4.3(c), (d) and 4.4(c) show the inverse susceptibility, $H/M(T)$, along and perpendicular to the c-axis of $Co_3Sn_{2-x}In_xS_2$ and $Co_{3-y}Fe_ySn_2S_2$, of indicated x ($< x_c$) and y, measured at $H = 1$ kOe. The inset of Figs. 4.3(e) shows $H/M(T)$ just above x_c. The CW-like behavior is observed above T_C for both substituted systems. Solid lines in theses figs. are the fit to the modified CW law,

$$\chi = \chi_0 + \frac{C}{T-\theta_W}, \qquad (4.1)$$

where χ_0, C and θ_W represent a temperature independent Pauli paramagnetic term, the Curie constant and the Weiss temperature, respectively. The observed magnetic susceptibility behaviors above T_C well fit eq. (4.1) as shown in the figures. In both substituted systems, χ_0 is negligible for x and $y \lesssim 0.5$, and thus, χ_0 is fixed to be 0 in the fitting to the data of samples for $x, y < 0.5$. The effective magnetic moment in the paramagnetic state p_{eff} is estimated from $C = (N_A\mu_B^2 p_{eff}^2)/3k_B$, where N_A, μ_B and k_B are the Avogadro's number, Bohr magneton and Boltzmann constant, respectively. The fitting results are listed in table 4.1.

Table 4.1: Static magnetic parameters of $Co_3Sn_{2-x}In_xS_2$ and $Co_{3-y}Fe_ySn_2S_2$.

x	χ_0 (10^{-5} emu /f.u.-mol)	P_{eff} (μ_B/3d-atom)	θ_W (K)	T_C (K)	P_s (μ_B/3d-atom)
0	0	0.607	174	173.5	0.283
0.14	0	0.540	164.5	161	0.250
0.34	0	0.427	140	126	0.183
0.52	0	0.400	105	90	0.140
0.65	24	0.327	73	40	0.083
0.72	11	0.237	68	21	0.043
0.87	6.5	0.203	27	0	0
0.90	9.5	0.177	9	0	0
y					
0.00	0	0.607	174	173.5	0.283
0.14	0	0.560	158	156	0.230
0.32	0	0.5	144	136	0.203
0.39	0	0.463	130	121	0.177
0.50	2	0.453	99	101	0.117

The magnetic hysteresis loops of $Co_3Sn_{2-x}In_xS_2$ and $Co_{3-y}Fe_ySn_2S_2$, for representative x and y, measured with applying magnetic fields along the easy c-axis at 2 K, are presented in Figs. 4.5(a) and (b), respectively. The magnetization in the ferromagnetic regions ($x < 0.8$ and $y \leq y_{max} = 0.5$) saturates rapidly at very low fields. In consistence with the $M(H)$ curves of the Stoner-Wohlfarth (SW) model, square-shaped hysteresis-curves are observed, confirming that c-axis is the easy axis. The saturated magnetization corresponding to the ordered ferromagnetic moment is reduced monotonically with increasing the In and Fe concentrations. The coercive field of $Co_3Sn_2S_2$ at 2 K is only ~ 2 kOe, in agreement with reported results[119]. The coercivity is reduced upon the In- or Fe-substitution, for instance it is about 600 Oe for $x = 0.72$, as well as the saturation magnetization. The magnetic hysteresis curves in the two systems, with applying magnetic field perpendicular to the c-axis (in the ab plane), are shown the insets of Figs. 4.5(a) and (b). In the In-substituted system for $x < 0.5$ and the Fe-substituted system, the magnetization in the ab plane does not saturate up to fields of 7 T, unlike those along the c-axis. In consistence with the observed anomalies in the temperature-dependence shown in Fig. 4.3(b), saturation of M_{ab} is found in the samples for $0.52 \leq x \leq 0.8$. The samples of $x \geq 0.87$ do not show hysteresis behaviors both along and perpendicular to the c direction even at 2 K, convincing the absence of the ferromagnetic order indicated in the temperature dependence of the magnetization shown in Figs. 4.3(e), (f). On the other hand, the magnetization in the ab plane of $Co_{3-y}Fe_ySn_2S_2$ does not saturate up to fields of 7 T in the whole solubility range. The results of the ab plane magnetizations indicate that the magnetic anisotropy in the ferromagnetic state is moderately reduced only close to the magnetic instability.

The well-known Arrott plot, $M^2(T, H)$ vs. $H/M(T, H)$, is usually used to determine the onset of ferromagnetism, i.e., the Curie temperature T_C, and the spontaneous magnetization $M_s(T)$ precisely[143]. Figures 4.6(a) and (b) show the Arrott plots at various temperatures for $Co_3Sn_{1.48}In_{0.52}S_2$ and $Co_{2.5}Fe_{0.5}Sn_2S_2$, respectively. Nearly linear relations are observed and the values of T_C are determined as 90 and 101 K for $Co_3Sn_{1.48}In_{0.52}S_2$ and $Co_{2.5}Fe_{0.5}Sn_2S_2$, respectively. The values of T_C are determined for each concentration sample in the In- and Fe-substituted systems by the same way. Figures 4.6(c) and (d) show Arrott plots at 2 K, of the magnetically ordered samples of $Co_3Sn_{2-x}In_xS_2$ and $Co_{3-y}Fe_ySn_2S_2$, respectively. The spontaneous magnetic moment at 2 K, which can be considered to be that at $T = 0$ K, p_s, of each concentration sample can be estimated by extrapolating the Arrot plots to $H = 0$. The estimated T_C and p_s of $Co_3Sn_{2-x}In_xS_2$ and $Co_{3-y}Fe_ySn_2S_2$ are listed in tables 4.1.

The In- and Fe-concentration dependences of the magnetic parameters T_C, p_{eff} and p_s are shown in Figs. 4.7(a) and (b). All parameters show almost identical behavior against the In- and Fe-concentrations. Both the In- and Fe-concentrations correspond to the reduced number of electrons per one formula unit. Hence, the similarity of the magnetic parameters in

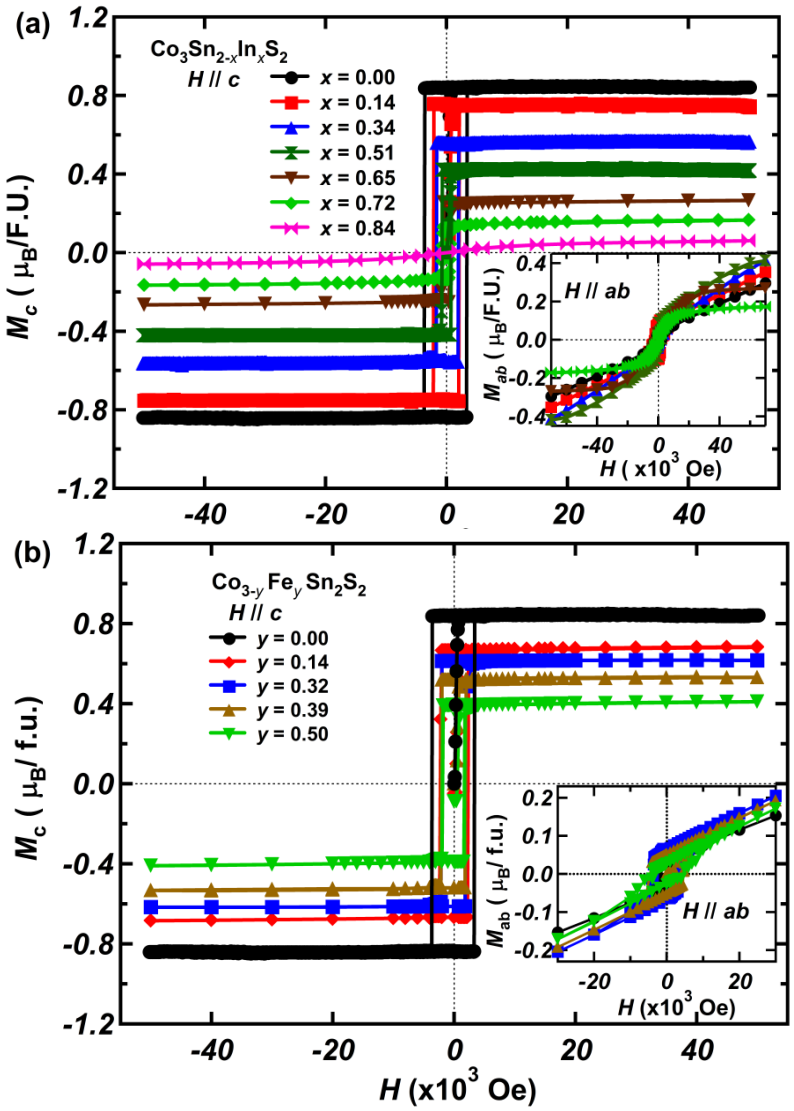

Figure 4.5: Magnetic hysteresis loops of (a) $Co_3Sn_{2-x}In_xS_2$ and (b) $Co_{3-y}Fe_ySn_2S_2$ at 2 K measured along the *c*-axis. Insets show hysteresis loops at 2 K measured perpendicular to the *c*-axis (in the *ab* plane).

the In- and Fe-substituted systems indicates that the electron number is the most dominant parameter to control the magnetism in the Co-shandites. The crystal structure effects by the substitutions should be less relevant to the magnetism of Co-based shandites. For instance, the itinerant electron magnetism is generally enhanced by the lattice expansion. In contrast the suppression of the magnetism is observed with the lattice expansion by In- and Fe-substitutions, previously shown in Fig. 3.8 of chapter 3. Moreover, the Fe- and In-substituted

systems show quite different c/a ratios as shown in the inset of Fig. 3.8. The significance of electron counts to the magnetism and the contribution of the 3d (Co) and 5p (Sn) atoms to DOS at the Fermi level in shandite compounds are predicted based on reported band structure calculations[83,114,117,126]. As seen in Figs. 4.7(a) and (b), T_C and p_s vanish as approaching the critical concentration $x_c \sim 0.8$. No sign of discontinuity is found, suggesting continuous (second order) quantum phase transitions. The In- and Fe-concentration dependences of p_{eff}/p_s are shown in Fig. 4.7(c). p_{eff}/p_s exhibits a divergent behavior as approaching x_c, with reflecting the moderate linear behavior of p_{eff} in the whole concentration and vanishing of p_s at x_c. The high values and strong enhancement of p_{eff}/p_s indicate the itinerant electron nature of the magnetism of the Co-based shandites.

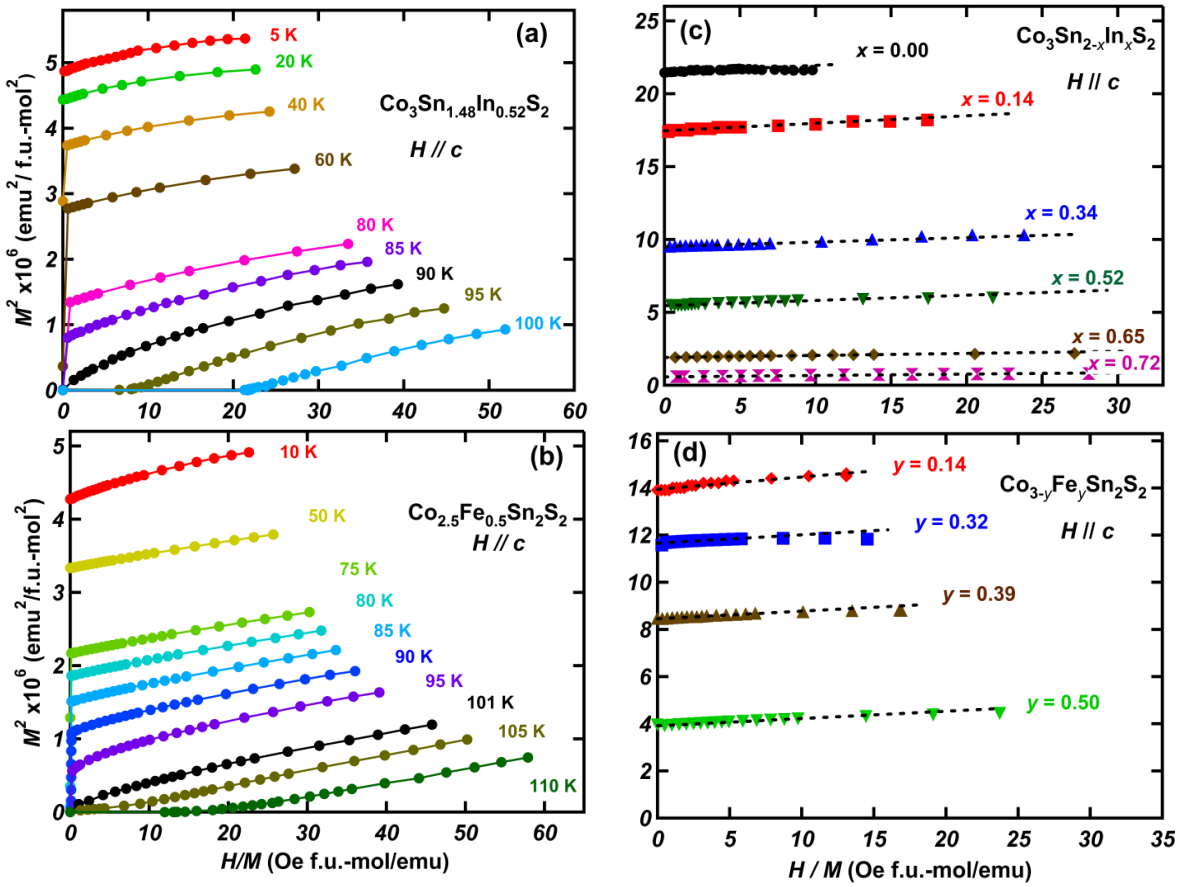

Figure 4.6: Magnetization isotherms along the c-axis in the form of M^2 versus H/M, the Arrott plot, for (a) $Co_3Sn_{1.48}In_{0.52}S_2$ and (b) $Co_{2.5}Fe_{0.5}Sn_2S_2$ at several representative temperatures. Arrott plots of (c) $Co_3Sn_{2-x}In_xS_2$ and (d) $Co_{3-y}Fe_ySn_2S_2$ at 2 K with applying magnetic field along the c-axis. Dashed lines in (c) and (d) are results of the linear fits.

4.3.2 Analysis and Discussion of the Q2D itinerant electron magnetism

Here, we try to analyze the magnetization data of the Co-based shandites based on the phenomenological spin fluctuation theory[8]. The theory describes the itinerant electron magnetism using a few phenomenological parameters: measures of the spin fluctuation spectrum in wave vector and energy spaces, T_A and T_0. In this theory, the zero temperature magnetization is derived in the form of the Arrott plot with the assumption of the total spin fluctuation conservation:

$$M^2(T,H) = M_0^2(T) + \xi\,[H/M(T,H)], \tag{4.2}$$

$$\xi = \frac{N_0^3(2\mu_B)^4}{F_1 k_B}, \tag{4.3}$$

$$F_1 = \frac{4T_A^2}{15T_0}, \tag{4.4}$$

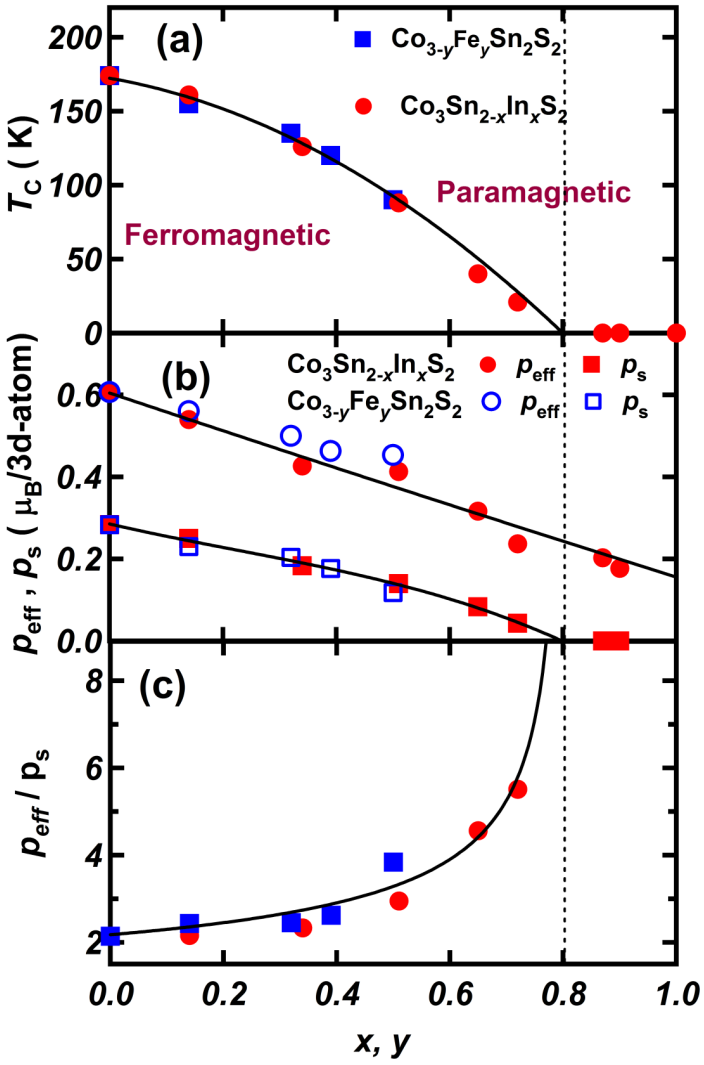

Figure 4.7: Fe- and In-concentration dependencies of (a) the Curie temperatures T_C, (b) the spontaneous moment p_s and effective moment p_{eff} per magnetic atom, (c) p_{eff}/p_s.

where M_0, N_0 and g are the magnetization at $H = 0$, number of the magnetic atoms (= $3N_A$ in Co-based shandites) and g factor, respectively. F_1 is the parameter related with the slope of the Arrott plot ξ through Eq. 4.3. When $T_C << T_0$, the following relations are also derived[7,8]:

$$p_S^2 = \left(\frac{20T_0}{T_A}\right) C_{4/3} (t_C)^{4/3}, \quad (4.5)$$

$$\frac{p_{eff}}{p_s} \cong 1.4\, t_C^{-2/3}. \quad (4.6)$$

where $t_C = T_C/T_0$ is a scaled Curie temperature and $C_{4/3} = 1.00608\ldots$. The equations (4.2) - (4.5) indicate that we can estimate the spin fluctuation parameters T_0 and T_A using experimentally-obtained ξ, p_s and T_C. The universal relation between p_{eff}/p_s and t_C in Eq. (4.6) was confirmed in several weak itinerant-electron ferromagnets (WIEF) such as $Y(Co_{1-x}Al_x)_2$[144] and $Fe_{1-x}Co_xSi$[145].

The estimated spin fluctuation parameters in $Co_3Sn_{2-x}In_xS_2$ and $Co_{3-y}Fe_ySn_2S_2$ by employing Eqs. (4.3) - (4.6) are listed in table 4.2. Both T_0 and T_A increase with increasing of the In- and Fe-concentrations. Figure 4.8 shows p_{eff}/p_s vs. t_C plot, the so-called the generalized Rhodes-Wohlfarth plot[7], for the Co-based shandites. The solid line represents the universal relation of Eq. (4.6) expected in the WIEF[7,8]. The values of p_{eff}/p_s and t_C of the Co-based shandites are much smaller than that expected from the universal curve. It indicates that the ferromagnetism in the Co-based shandites is much weaker than the conventional 3D WIEF. It can be a manifestation of the Q2D character due to their layered crystal structures.

Layered crystal structures can arise strong anisotropic electronic states and consequent Q2D characters in the electronic and magnetic properties. In general, dimensional reduction suppresses the long-range orders. Hence, the small p_{eff}/p_s and t_C in the generalized Rhodes-Wohlfarth plot of Fig. 4.8 implies the appearance of their Q2D nature in the layered Co-based shandites. Indeed, the reported data of several layered compounds, shown in Fig. 4.8, exhibit similar deviations from the universal curve of the 3D systems. To discuss on it, the comparison between the experimental results and calculated results based on the Q2D spin fluctuation theory[9] is presented. The phenomenological spin fluctuation theory was extended to consider the Q2D magnetic systems by introducing a new parameter $\varepsilon = \sqrt{m/m'}$ which is a measure of the ratio between the in-plane and out-of-plane effective masses, m and m', of the electronic motions, respectively. $\varepsilon = 1$ and 0 correspond to the ideal 3D and 2D cases, respectively. With considering this parameter, the universal relation (4.6) between p_{eff}/p_s and t_C is modified to the ε-dependent one[9],

$$\left(\frac{P_{\mathrm{eff}}}{P_{\mathrm{s}}}\right)^2 = \frac{3-\varepsilon^2}{20\, t_{\mathrm{c}}\, S(0,\ t_{\mathrm{c}}/\varepsilon^3)}\left(\frac{dY}{dt}\right)^{-1}. \qquad (4.7)$$

Here t and Y are the scaled temperature T/T_0 and scaled inverse susceptibility $N_o/2k_BT_A\chi$, respectively. $S(Y, t_C/\varepsilon^3)$ is related to the amplitude of the thermal spin fluctuation. The scaled temperature dependences of Y and S are evaluated from the self-consistent equations, described in Ref. 9 in detail, however, to distinguish from the symbols used here for Fe concentration and temperature as y and T, respectively, we introduce the scaled inverse susceptibility parameter and the parameter related with the amplitude of the thermal spin fluctuation as Y and S, respectively, instead of y and T used for the same parameters in the spin fluctuation theory presented in Ref. 9. Equation (4.7) asymptotes to Eq. (4.6) when ε approaching 1. Numerically

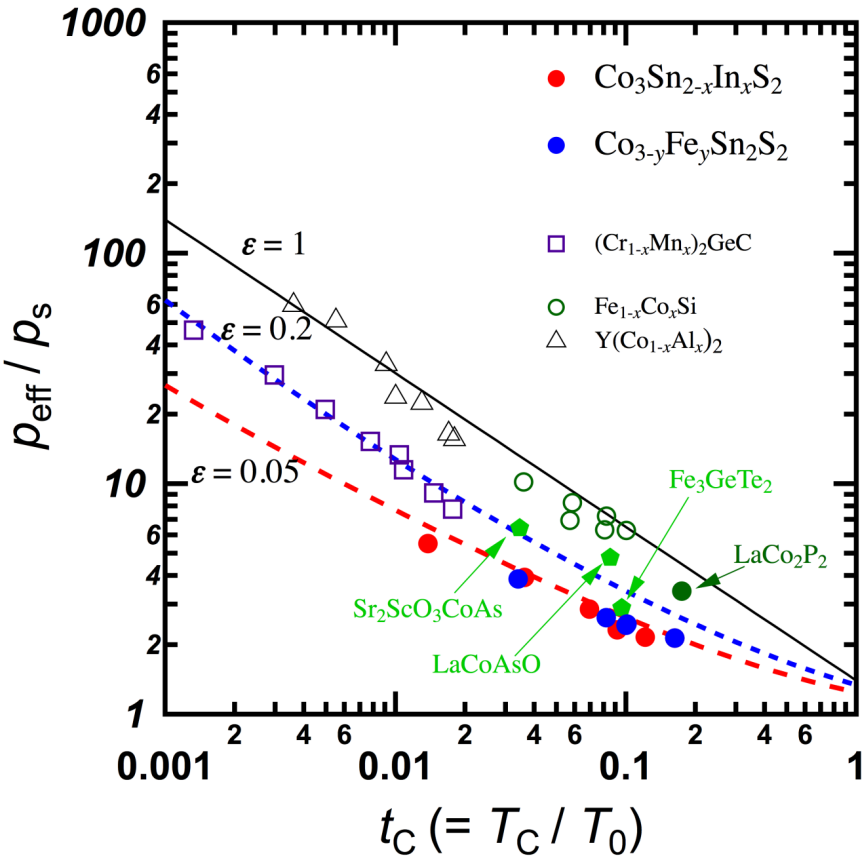

Figure 4.8: The generalized Rhodes–Wohlfarth plot, $p_{\mathrm{eff}}/p_{\mathrm{s}}$ versus t_{C} (= T_{C}/T_0), in a double logarithmic scale (Deguchi-Takahashi plot)[8]. The data of $Co_3Sn_{2-x}In_xS_2$ and $Co_{3-y}Fe_ySn_2S_2$ are plotted together with data of typical reported itinerant electron magnets cited from ref. 8. Data of other reported Q2D-WIEFs, $(Cr_{1-x}Mn_x)_2GeC$[146] and Sr_2ScO_3CoAs[147], LaCoAsO[148] and Fe_3GeTe_2[149] are also included for comparison. The solid line represents the universal curve in the ideal 3D systems of eq. (4.6) (or eq. (4.7) with $\varepsilon = 1$). Dashed lines are the numerical calculated results of eq. (4.7) with the Q2D parameters $\varepsilon = 0.2$ and 0.05.

Table 4.2. Spin fluctuation parameters of $Co_3Sn_{2-x}In_xS_2$ and $Co_{3-y}Fe_ySn_2S_2$ ferromagnets. The values of F_1were obtained from the slope of Arrot plot at 2 K.

x	F_1 (10^4 K)	T_A (10^4 K)	T_0 (10^3 K)	T_C/T_0	P_{eff}/P_s
0.00	11.16	2.27	1.23	0.142	2.14
0.14	10.57	2.46	1.52	0.106	2.16
0.34	17.55	3.22	1.57	0.081	2.33
0.52	22.24	3.5	1.47	0.060	2.86
0.65	27.12	3.71	1.35	0.030	3.93
0.72	40.72	5.21	1.78	0.012	5.51
y					
0.14	9.76	2.60	1.84	0.085	2.43
0.32	14.27	2.91	1.58	0.086	2.46
0.39	15.54	3.20	1.76	0.069	2.62
0.50	15.76	4.43	3.32	0.030	3.87

calculated results of the t_C-dependence of p_{eff}/p_s with several non-unity ε are shown in Fig. 4.8. The experimental data of the Co-based shandites roughly coincide with the result with $\varepsilon = 0.05$. The small value of ε clearly indicates the highly inherent Q2D nature of the magnetism in the Co-based shandites.

4.4 Conclusion

We performed comprehensive magnetization measurements on the layered Co-based shandites $Co_3Sn_{2-x}In_xS_2$ ($0 \le x \le 2$) and $Co_{3-y}Fe_ySn_2S_2$ ($0 \le y \le 0.5$) using single crystals. Strong magnetic anisotropy, the easy axis magnetization is about one order of magnitude higher than that in the *ab* plane, is preserved in the ferromagnetic regime of $Co_3Sn_{2-x}In_xS_2$ and $Co_{3-y}Fe_ySn_2S_2$ solid solutions. The almost identical variations of the obtained magnetic parameters against the In- and Fe-concentrations indicate the significance of the electron count on the magnetism in the Co-based shandites. The ferromagnetic instability is found around x_c (or y_c) ~ 0.8. The divergent behavior of p_{eff}/p_s with approaching x_c indicates WIEF nature. Analysis based on the extended Q2D spin fluctuation theory reveals the high Q2D character of the ferromagnetism in the Co-based shandites due to their layered crystal structure.

CHAPTER 5

5 Magnetic Properties II: Topological Hall Effect in $Co_3Sn_{2-x}In_xS_2$ Ferromagnets

5.1 Motivations and Purpose

The chiral spin systems have recently attracted a large interest due to its exciting properties that could make them important ingredients for future data storage and spintronics applications[150]. As briefly introduced in chapter 1, subsec. 1.2.1, usually in magnetic crystals of frameworks appropriate for the relativistic spin-orbit Dzyaloshinskii-Moriya (DM) interactions[29,30] and/or the spin frustration the chiral spin order (CSO) becomes favored and hence the topological Hall effect (THE) emerges[33].

As one of the 2D-kagomé itinerant electron magnetic system, $Co_3Sn_{2-x}In_xS_2$, is a candidate of CSO and THE. The anomalously increased in-plane component of the magnetic moment above $x \sim 0.5$, as shown in Fig. 4.3(b) of chapter 4, indicates a spin canting from the ferromagnetic order of $Co_3Sn_{2-x}In_xS_2$ and presence of fluctuating in-plane-component of spins when approaching the magnetic instability. Moreover, cusp-anomalies observed at $T^* \sim 7 - 10$ K in the T-dependence of M_{ab} only for $x \gtrsim 0.5$ suggest that the fluctuating in-plane component of spins are fixed and a nontrivial spin structure is formed. To investigate for the THE induced by the possible nontrivial spin structure in $Co_3Sn_{2-x}In_xS_2$, a combined work of the magnetization and magneto-transport measurements have been performed using the grown single crystals. The Hall resistivity results are analyzed and discussed in this chapter.

5.2 Outline

The motivations of measuring the magneto-transport properties of $Co_3Sn_{2-x}In_xS_2$ single crystals to investigate for the THE is briefly introduced above in sect. 5.1. The strategy followed in the THE estimation from the experimental Hall resistivity data is described in sect. 5.3. The results of the Hall resistivity and the THE analyses are presented and discussed in sect. 5.4. Sect. 5.5 concludes the present chapter.

5.3 Estimation of Topological Hall Effect

According to the topological Hall effect[33], the Hall resistivity in the presence of a nontrivial spin texture with finite scalar chirality is given by:

$$\rho_{\mathrm{H}}(T,H) = R_0(T)\,H + R_{\mathrm{s}}(T,H)\,M(T,H) + \rho_{\mathrm{H}}^{\mathrm{top}}(T,H), \qquad (5.1)$$

where R_0 and R_S are the ordinary and anomalous Hall coefficients, respectively, and $\rho_H^{top}(T,H)$ is the topological Hall resistivity induced by the uniform scalar spin chirality $\chi_u^0 \approx \sum_{ijk}\chi_{ijk}$ as $\rho_H^{top}(T,H) \propto \chi_{ijk}$. Since the T- and H-dependences, and also whether presence or absence, of the topological Hall resistivity are unknown beforehand, the term of $\rho_H^{top}(T,H)$ can be experimentally estimated as a difference between the experimental Hall resistivity $\rho_H^{exp}(T,H)$ and the phenomenological Hall resistivity, of conventional magnetic systems,

$$\rho_H^{phe}(T,H) = R_0(T)\,H + R_s(T,H)\,M(T,H), \qquad (5.2)$$

which is the Hall resistivity without the THE term in eq. (5.1). The T- and H-dependences of $\rho_H^{phe}(T,H)$ are estimated by analyzing the experimental $\rho_H^{exp}(T,H)$ using measured magnetization data $M(T, H)$ and measured longitudinal resistivity $\rho_{xx}(T, H)$ because the anomalous Hall coefficient $R_s(T, H)$ is a function of $\rho_{xx}(T, H)$ expressed as,

$$R_s(T,H) = \alpha\,[\rho_{xx}(T,H)]^{\beta}, \qquad (5.3)$$

according to the theory of the anomalous Hall effect[33]. The exponent β varies from 1 to 2 corresponding to the clean and dirty limits, respectively[33]. In the paramagnetic region ($x > x_c \sim 0.8$ or $T > T_C$), an absence of the topological Hall effect is naturally expected and the experimental $\rho_H^{exp}(T,H)$ as a function of H can be fitted using eq. (5.2) by treating α, β and $R_0(T)$ as free parameters. After that, the validity of the assumption, the absence of the topological Hall effect, is checked by whether the fitting by eq. (5.2) well describes the experimental data. On the other hand, a possible existence of the topological Hall effect should be assumed in the ferromagnetic region as mentioned in sec. 5.1, and thus, ρ_H^{phe} should be estimated more carefully. At enough high field, the possible noncoplaner spin texture is generally expected to be closed and become collinear. Hence, a Hall resistivity at zero field extrapolated from high field data $\rho_H^{exp}(T,0)$ should contains only the spontaneous term of ρ_H^{phe}, $R_s(T, 0)\,M(T, 0)$, and the parameters α and β describing the ρ_{xx}-dependence, namely, T- and H-dependences of R_s can be estimated by fitting of $Rs(T,0) = \rho_H^{exp}(T,0)/M(T,0)$ at various temperatures as a function of $\rho_{xx}(T, 0)$ as,

$$R_s(T,0) = \alpha\,[\rho_{xx}(T,0)]^{\beta}. \qquad (5.4)$$

$R_0(T)$ is obtained by fitting $\rho_H^{exp}(T,H)$ at high fields as a function of H using estimated α, β and measured $\rho_{xx}(T, H)$. Now, the phenomenological transverse resistivity can be calculated in the whole range of H at all temperatures and thus $\rho_H^{top}(T,H) = \rho_H^{exp}(T,H) - \rho_H^{phe}(T,H)$ can be extracted.

5.4 Experimental Results

The transverse (Hall) and longitudinal resistivities of $Co_3Sn_{2-x}In_xS_2$ single crystals presented in this chapter were simultaneously measured via a Van der Pauw setting, which is described above in subsect. 2.3.5 of chapter 2, by applying magnetic fields (up to 5 T) along the *c*-axis and small currents in the *ab*-plane. The magnetization, $M(T,H)$, data required for analysis were measured for the same sample pieces by applying fields along *c*-direction. The magnetic field dependences of the measured $\rho_H(T, H)$, $\rho_{xx}(T,H)$ and $M(T,H)$ for $Co_3Sn_{2-x}In_xS_2$ single crystals of selected *x* are shown in Fig. 5.1. The experimental data of $\rho_H(T, H)$, $\rho_{xx}(T,H)$ and $M(T,H)$ of $x = 0.00$ are respectively shown in Figs. 5.1(a), (b) and (c) at the indicated temperatures and respectively shown at the measurement lowest temperature, 5 K, for selected

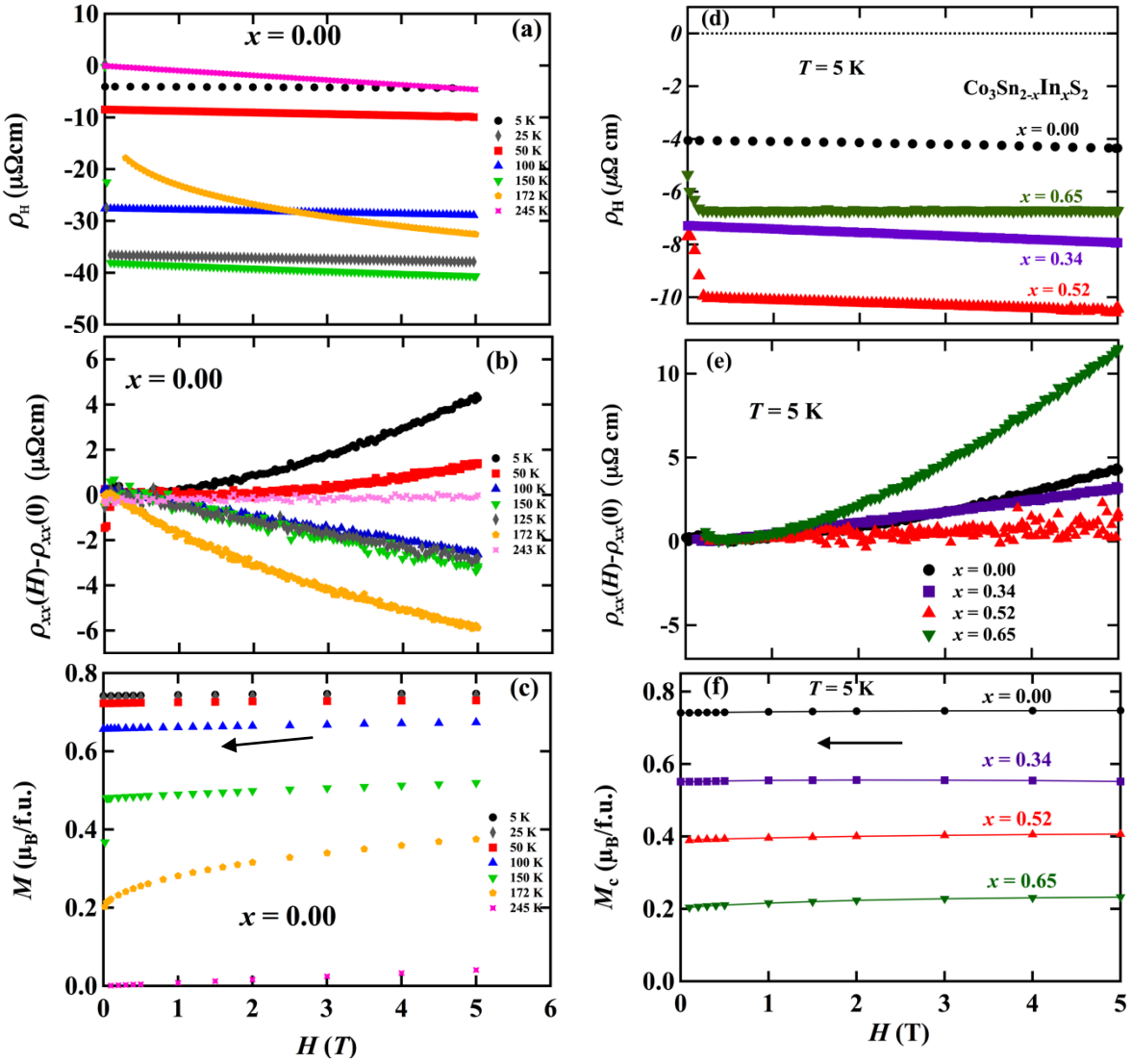

Figure 5.1: Field dependences of the experimentally observed transverse (Hall) resistivity, longitudinal resistivity and magnetization, respectively, in (a), (b) and (c) for $Co_3Sn_2S_2$ at selected temperatures and in (d), (e) and (f) for $Co_3Sn_{2-x}In_xS_2$, of indicated *x*, at 5 K.

crystals of $Co_3Sn_{2-x}In_xS_2$ in Figs. 5.1(d), (e) and (f). Fig. 5.2 shows the field dependences of $\rho_H(T, H)$ and $M(T, H)$ for the nonmagnetic concentrations of $Co_3Sn_{2-x}In_xS_2$. The Hall resistivity is negative in the ferromagneticlly ordered phase and paramagnetic region for $x < 1.0$ becomes

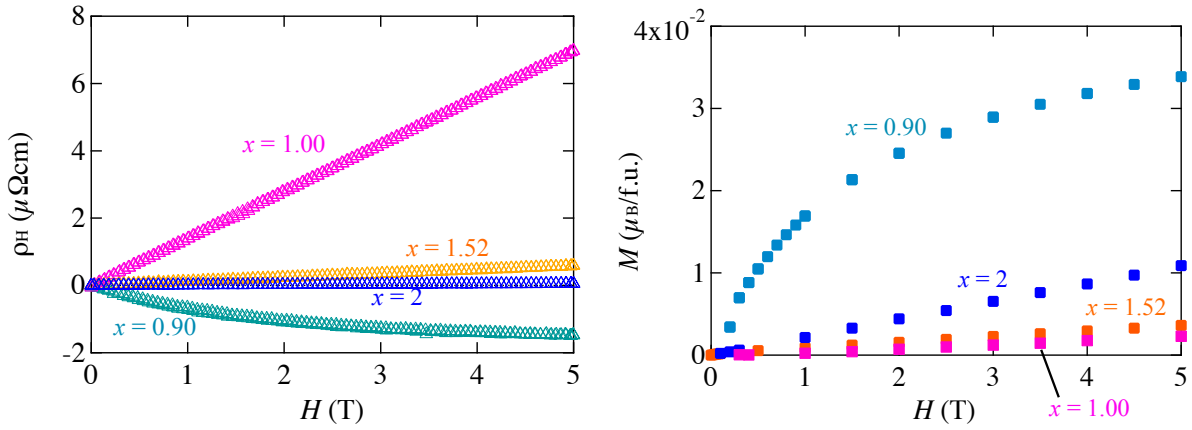

Figure 5.2: Field dependences of the experimentally observed (a) Hall resistivity and (b) magnetization of $Co_3Sn_{2-x}In_xS_2$, of $x \geq 0.90$, at 5 K.

positive only for $x \gtrsim 1.0$. Although the magnetization almost unchanged with reducing magnetic fields from 5 T down to zero in the whole ferromagnetic samples below T_C, the Hall resistivity does not for $0.5 \lesssim x < 0.8$ and shows deviations at low temperatures.

5.5 Analysis Results

Following the strategy described in sect. 5.3, the phenomenological Hall resistivity has been calculated. Figure 5.3(a) shows the field dependence of the measured (symbols) and calculated Hall resistivities (sold lines) of $Co_3Sn_2S_2$ and low ($x < 0.5$) In-substituted ferromagnets, while Figs. 5.3(b) shows those of the paramagnetic samples. The absence of the topological Hall effect in the nonmagnetic phase has been observed in $Co_3Sn_{2-x}In_xS_2$ for $x \geq 0.9$ by the complete coincidence of the experimental and phenomenological Hall resistivity in the whole range of T and H, see Figs. 5.3(b). In the ferromagnetic region, for $x = 0.0$ and low In concentrations, we found that the experimental data, $\rho_H^{exp}(T, H)$, are also well regenerated by the phenomenological expression of $\rho_H^{phe}(T, H)$ at all temperatures and in the whole region of H, see Figs. 5.3(a). The absence of topological Hall effect, $\rho_H^{top}(T, H) = 0$, indicates collinear ferromagnetic state at low In concentrations.

By approaching the QCP and typically above $x \sim 0.5$, a distinct $\rho_H^{top}(T, H)$ is observed at low H-regions far below the curie temperature T_C as shown in Figs. 5.4(a-c) for $x = 0.52$ at

various T and in Figs. 5.4(d-f) for $0.5 \lesssim x < 0.8$ at low temperatures. Large positive $\rho_H^{top}(T,H)$ for $0.5 \lesssim x < 0.8$ have been observed at fields below ~ 0.2 T and temperatures below $T^* = 7$ - 10 K, corresponding to the temperatures where the cusp anomalies in M_{ab} presented above in subsect. 4.2.1 of chapter 4.

Figures 5.5 and 5.6 show the temperature dependences of R_0 and R_S, respectively, for various In concentration in $Co_3Sn_{2-x}In_xS_2$. R_0 and R_S are negative in the ferromagnetic region. In consistence with previously reported data of the Seebeck coefficient[83,127], R_0 changes its sign from negative to positive at $x \sim 1.0$ indicating Fermi energy tuning from electron- to hole-like conduction bands. The electronic state of $Co_3Sn_{2-x}In_xS_2$ is studied by measuring the transport properties and is presented below in details in chapter 7.

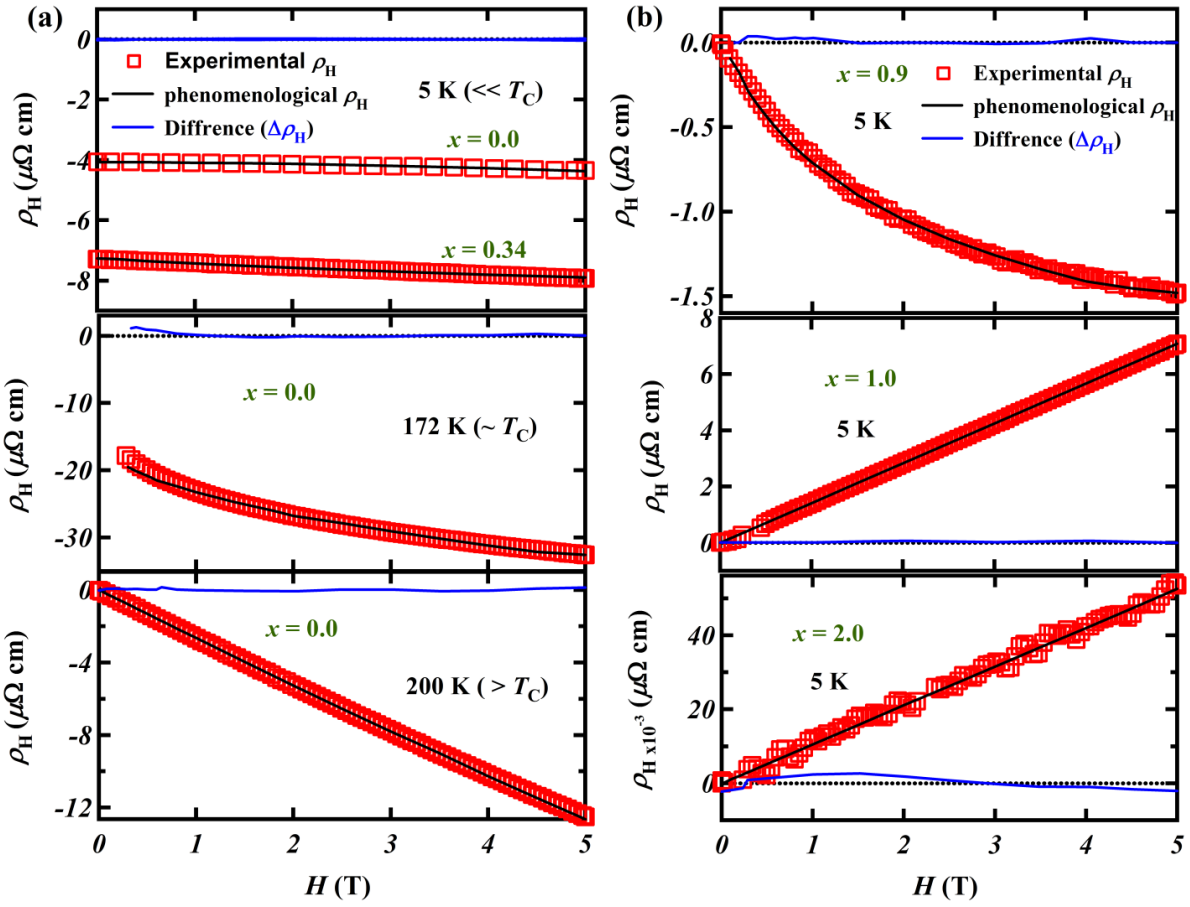

Figure 5.3: Field dependences of experimentally observed (symbols) and phenomenologically calculated (solid black lines) and the topological, simply obtained by subtraction, (solid blue lines) Hall resistivity of (a) ferromagnetic, $x < 0.5$, and (b) nonmagnetic, $x > 0.9$, $Co_3Sn_{2-x}In_xS_2$ at indicated temperatures.

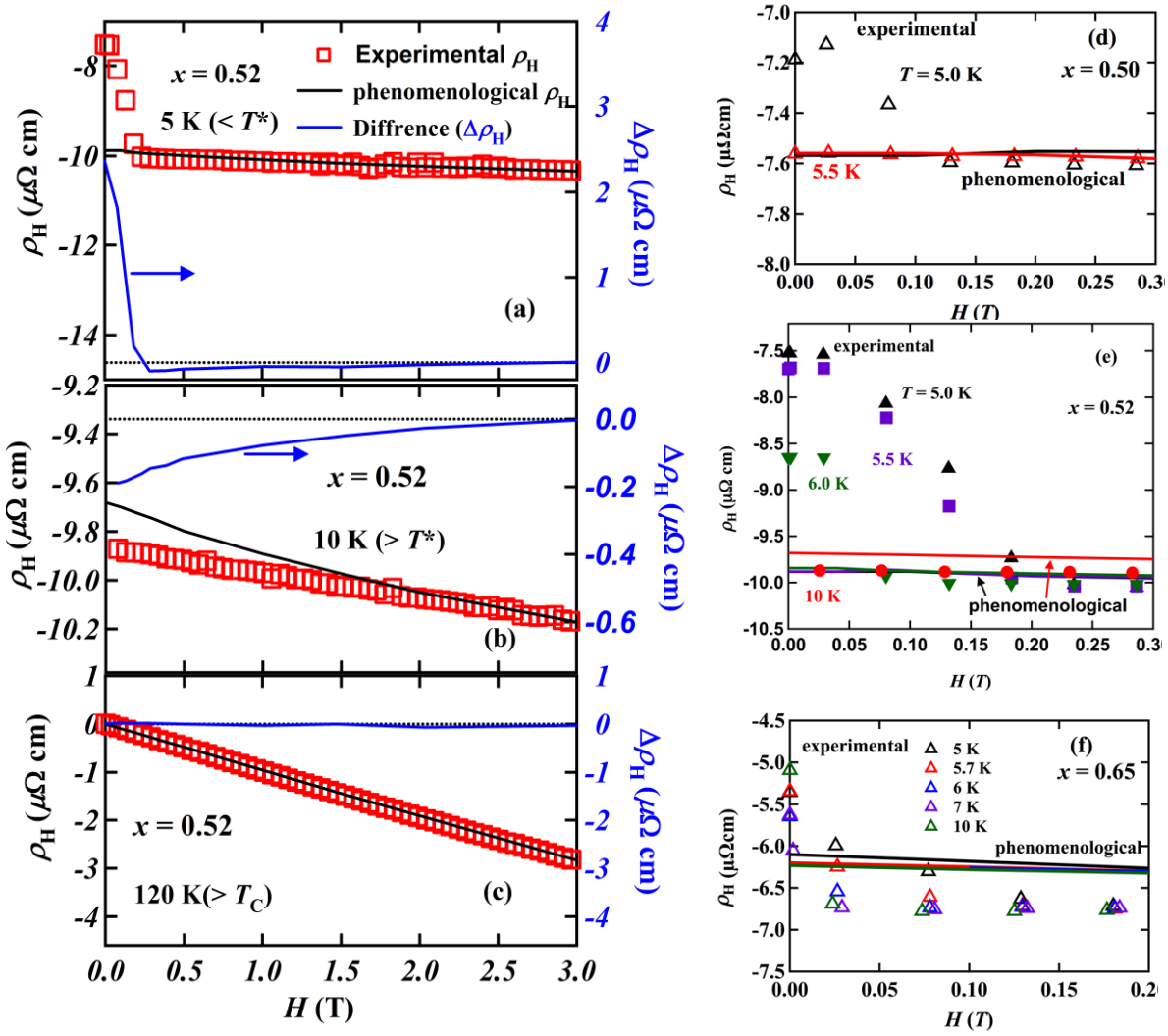

Figure 5.4: Field dependences Experimental (symbols), phenomenological (solid lines) and topological (blue solid lines) of Hall resistivity in for $0.5 \lesssim x < 0.8$: for $x = 0.52$ at (a) 5 K, below T^* and much below T_C, (b) 10 K, above T^* and below T_C, and (c)120 k, above T_C. At low magnetic fileds and low temperatures for (d) $x = 0.50$, (e) $x = 0.52$ and (f) $x = 0.65$.

Following the strategy described in sect. 5.3, the THE has been quantitatively estimated. For instance, typical $\rho_H^{top} \sim 2.36$ $\mu\Omega$ cm was observed at 5 K for $x = 0.52$ ($T^* = 7$ K). Small negative $\rho_H^{top}(T,H)$is observed for $0.5 \lesssim x < 0.8$ at $T > T^*$ that extends up to T_C. The negative $\rho_H^{top}(T,H)$ above T^* is sufficiently robust against H up to ~ 2 T. Figure 5.7 shows the T-dependence of the THE of $Co_3Sn_{2-x}In_xS_2$, $0.5 \lesssim x < 0.8$.

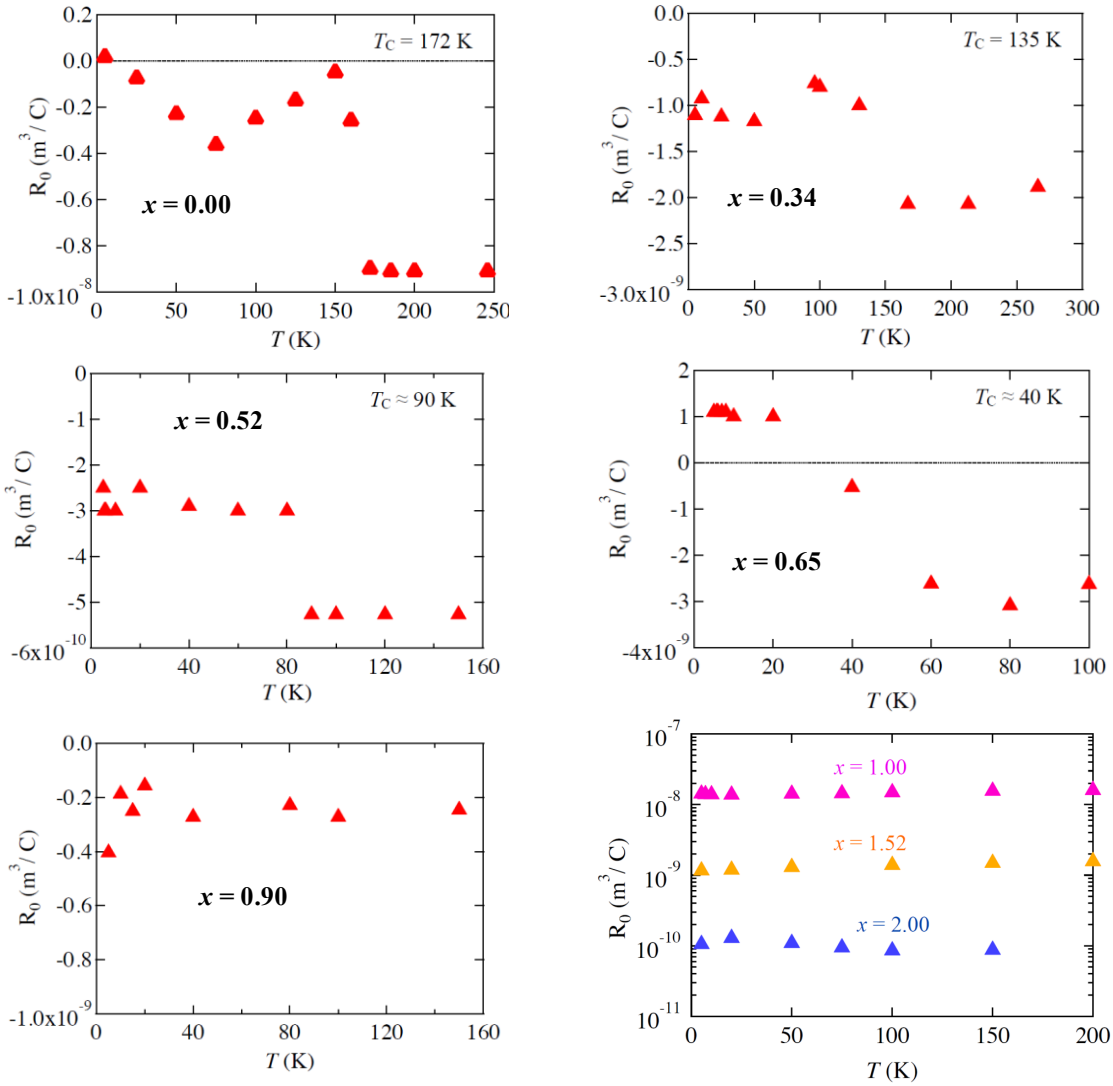

Figure 5.5: The temperature dependences of the ordinary Hall coefficient, R_0, for various In concentration in $Co_3Sn_{2-x}In_xS_2$, the negative R_0 indicates dominant charge chariers of electrons below x = 1.00 which is changed to holes for $x \geq 1.00$, Fermi level tuning.

5.6 Discussion

Here we discuss about the estimated THE $\rho_H^{top}(T,H)$ of varying quantity and sign at low and finite temperatures. The large positive $\rho_H^{top}(T,H)$ observed for $0.5 \lesssim x < 0.8$ at low temperatures below T^* is considered to be due to a static CSO with finite uniform chirality given by $\chi_u^0 = \sum_{ijk} \boldsymbol{S}_i.(\boldsymbol{S}_j \times \boldsymbol{S}_k)$ as a consequence of the emergent in-plane magnetic order[151], induced by the inherent DM-interaction and/or highly spin-frustarated effect in the Co- kagomé sublattice associated with enhancing of spin-fluctuations when approaching ferromagnetic QCP, as described in sec. 5.1. The non-coplanar spin structure anticipated below T^* in this composition region is shown in Fig.5.8(a) while Fig. 5.8(b) shows three Co atoms of spins $\boldsymbol{S}_i$, $\boldsymbol{S}_j$, $\boldsymbol{S}_k$ on one Co-triangle in an in-plane 2D-kagomé sublattice of $Co_3Sn_{2-x}In_xS_2$. The fictitious

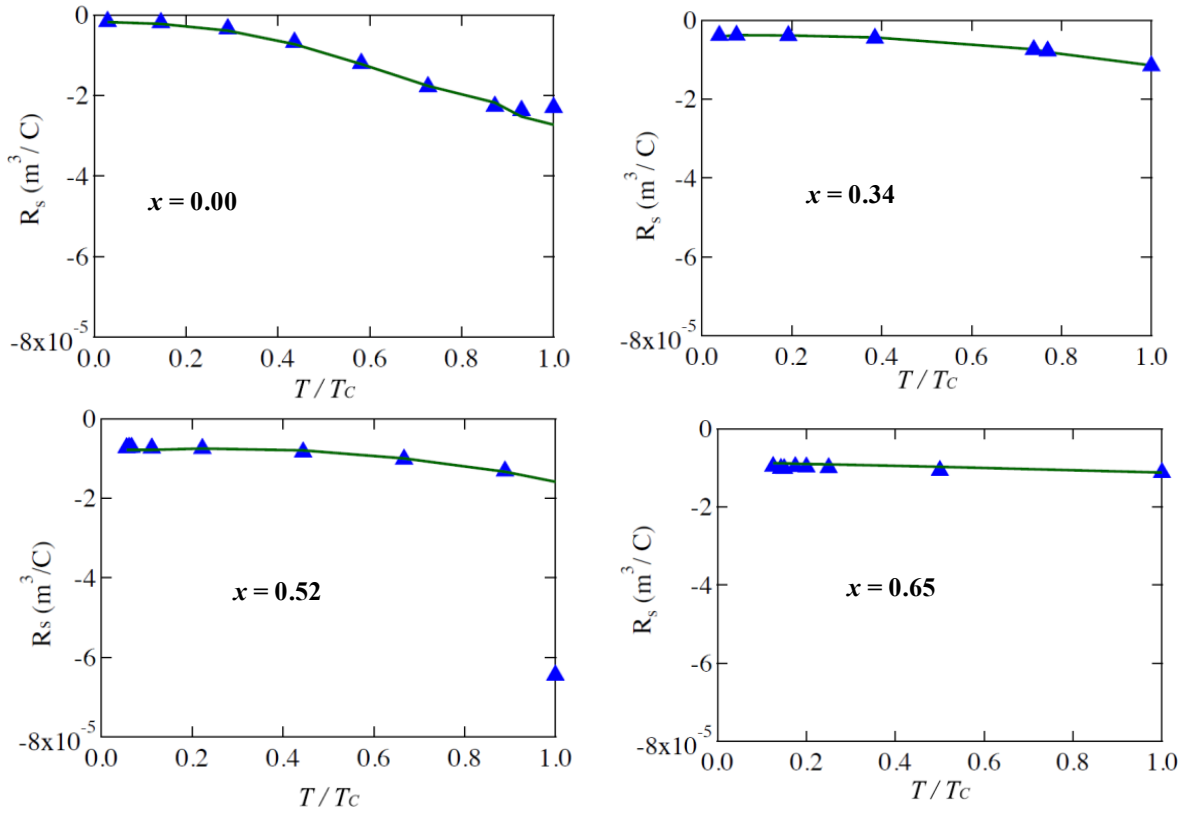

Figure 5.6: The temperature dependences of the anomalous Hall coefficient, R_s, at $H \rightarrow 0$ for various In concentration in $Co_3Sn_{2-x}In_xS_2$, R_S is negative at all In concentrations. Solid lines are the calculated R_S using zero-field resistivity as $R_s(T,0) = \alpha\,[\rho_{xx}(T,0)]^{\beta}$.

magnetic field, b_{eff}^{z}, generated by the nontrivial spin textures that can be approximated as, $\rho_{\text{H}}^{\text{top}}(T,H) = |PR_0 b_{\text{eff}}^{z}|$, where P is the electrons local spin polarization. The reported half-metallic ferromagnetic state in the magnetically ordered Co-based shandites [83,100,117,120], implies also $P = 1$ in our case. For $x = 0.52$ at 5 K, $R_0 = -0.03\,\mu\Omega$ cm /G and $\rho_{\text{H}}^{\text{top}} = 2.25\,\mu\Omega$ cm at $H \sim 800$ G, the estimated b_{eff}^{z} is about 750 kG (as large as 10^3 of the applied field). The large $\rho_{\text{H}}^{\text{top}}$ and the extremely high b_{eff}^{z} indicate large THE in $Co_3Sn_{2-x}In_xS_2$ compared to other chiral magnets[33,152,153].

The small negative THE of $Co_3Sn_{2-x}In_xS_2$ ($0.5 \lesssim x < 0.8$) observed at finite temperatures can be explained by a magnetization-induced uniform chirality in the para-chiral state given by $\chi_{\text{u}}^{T} = -\lambda\, M$, where λ is proportional to the spin-orbit coupling constant. In both weak coupling and strong coupling theories of THE[151,154], the spin-orbit energy is approximately given by $E_{\text{SO}} = -\chi_{\text{u}}\, M$, indicating that the magnetization M is a conjugate field of the uniform chirality. THE recently observed at high temperatures in some manganites has been explained by a uniform chirality induced by a strong Hund-coupling between the conduction electrons and local spins in the presence of uniform magnetization[42,151,154–156]. In case of $Co_3Sn_{2-x}In_xS_2$, large

spontaneous magnetization for $T^* < T < T_C$ can induce the unifrom chirality, that is observed robust against applied fields up to 2 T, if strong chiral fluctuation remains even at $T > T^*$.

Fig. 5.9 shows the magnetic phase diagram of $Co_3Sn_{2-x}In_xS_2$ established here based on the magnetization and Hall resistivity results. A stabilized finite static chiral order at low temperatures below T^* and emergent chiral fluctuations at higher temperatures up to the Curie temperature are observed only for ferromagnets of $0.5 \lesssim x < 0.8$. Further experimental

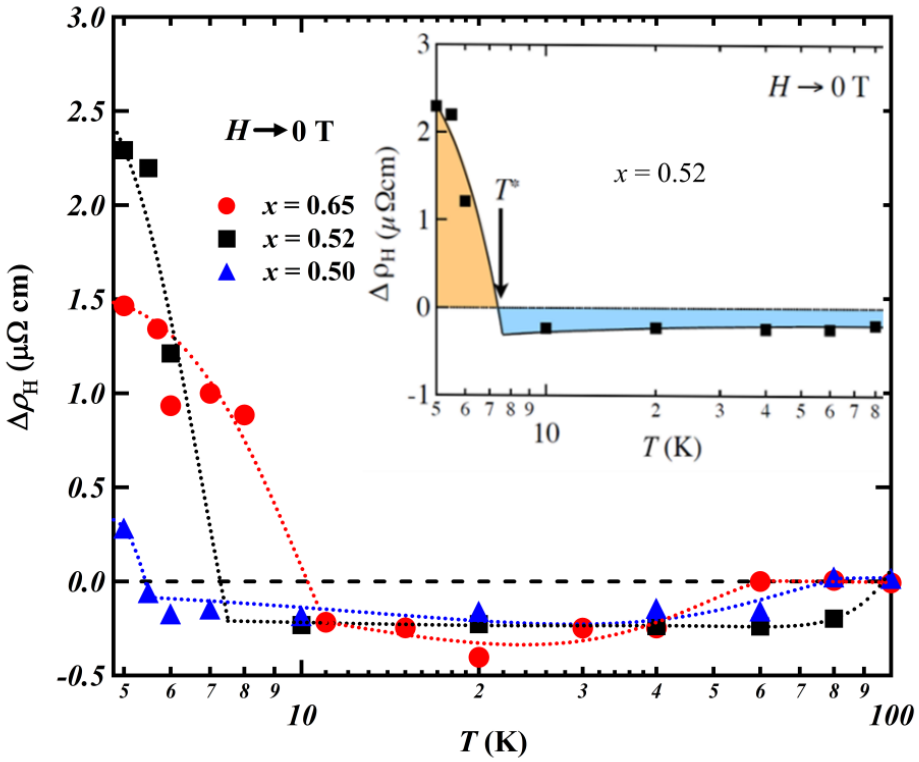

Figure 5.7: The temperature dependence of topologically driven Hall effect $\Delta\rho_H(T, H)$ of $x = 0.5$, 0.52 and 0.65. Inset shows the data of $x = 0.52$.

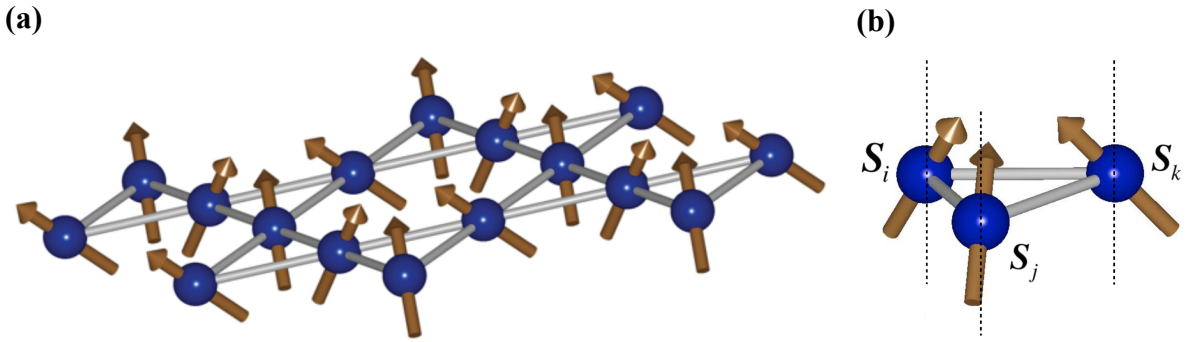

Figure 5.8: The anticipated non-collinear spin structure of $Co_3Sn_{2-x}In_xS_2$, $0.5 \lesssim x < 0.8$ at low temperatures shown for (a) one Co-kagomé sub-lattice and (b) Co-triangle of spins $\mathbf{S}_i$, $\mathbf{S}_j$ and $\mathbf{S}_k$ resulting in a scalar spin chirality of $\boldsymbol{\chi}_{ijk} = \boldsymbol{S}_i . (\boldsymbol{S}_j \times \boldsymbol{S}_k)$.

investigations for the static chiral state and its dynamics at finite temperatures using elastic and inelastic neutron scattering experiments are strongly required. The emergent chiral spin state is directly related to the drastic decrease of the magnetic anisotropy as approaching a QCP in $Co_3Sn_{2-x}In_xS_2$. The observed THE shown in Fig. 5.7 is proportional to the M_{ab} component shown in the inset of Fig. 4.1(b) of chapter 4. The present results initiate a question if the chiral spin states (non-coplanar spin textures) ubiquitously emerge near a QCP in the spin-frustrated itinerant ferromagnets, which may be answered by future experimental and theoretical studies in this topic.

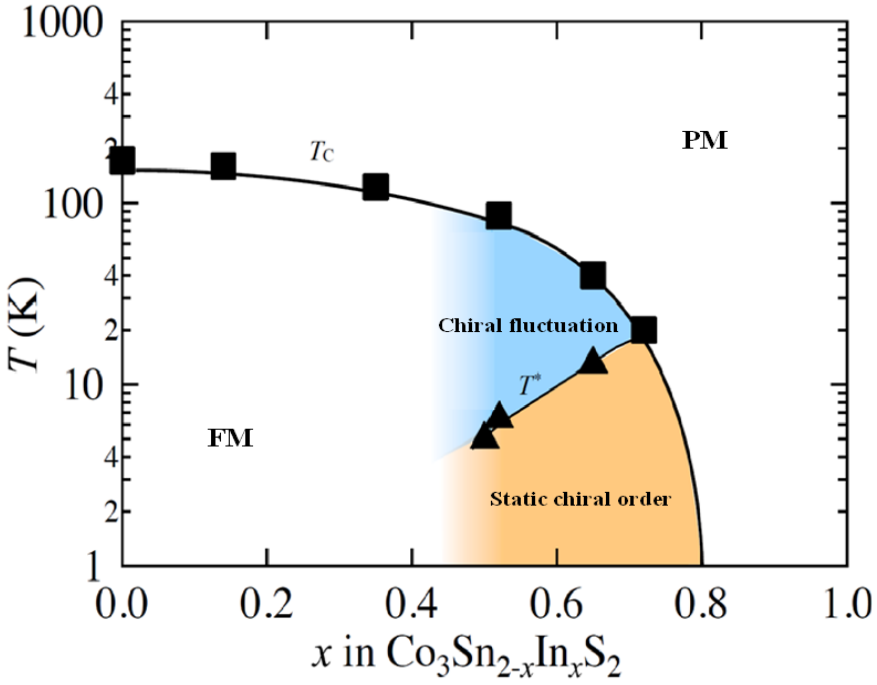

Figure 5.9: Magnetic phase diagram of $Co_3Sn_{2-x}In_xS_2$ showing the ferromagnetic, FM, static and fluctuating chiral state respectively below and above temperatures T^*, corresponding to an anomaly in the *ab*-magnetization and the paramagnetic order, PM, above the Curie temperature, T_C and for $x > 0.8$.

5.7 Conclusion

A chiral spin state in the kagomé-lattice ferromagnet $Co_3Sn_{2-x}In_xS_2$ was observed in the vicinity of the QCP ($0.5 \lesssim x < 0.8$) through a combined work of the magnetization and magneto-transport measurements. A distinct positive topological Hall effect (ρ_H^{top}) was observed at temperatures below 7 - 10 K and magnetic fields below 0.2 T. The observed chiral spin phase corresponds the anomalies observed in the *ab*-magnetization. Finite temperature Hall resistivity of topological nature and small negative contributions extending to Curie temperatures was also observed and attributed to chiral fluctuations of a magnetization-induced uniform chirality.

CHAPTER 6

6 Magnetic Properties III: Low-field Magnetic Phase Diagram of $Co_3Sn_2S_2$ Inferred from Magnetization and ac Susceptibility

6.1 Motivations and Purpose

Topologically protected spin textures are recently of great interest as introduced in sect. 1.3 of chapter 1. These particle-like nanometric vortices, magnetic skyrmions, arise by the asymmetric DM interactions and/or other mechanisms such as the frustrated exchanges[56], the four-spin exchange interactions or the dipolar interactions[57]. The magnetic phase diagrams of the non-centrosymmetric skyrmions-materials has been approached via systematic measurements of magnetization M and ac susceptibility χ_{ac}[157–161]. At the boarders of an A-phase of skyrmions 2D-triangular lattice, characteristic relaxation process with long relaxation times were observed in chiral B20 magnets[158–161]. With considering the possible DM interaction in the kagomé network of magnetic atoms, $Co_3Sn_2S_2$ of Co-kagomé sublattices may be a candidate of these topologically-protected spin textures stabilized, by the DM interaction, from the fluctuating spins in the vicinity of the Curie temperature, T_C. Anomalous magnetic transitions observed at low magnetic fields just below T_C of $Co_3Sn_2S_2$ have prompted us for further investigations by M and χ_{ac} measurements following the ZFC and FC schemes described in subsect. 2.3.4 of chapter 2 and the low-fields magnetic phase diagrams are targeted.

6.2 Outline

The motivating features for further investigation of $Co_3Sn_2S_2$ magnetic ground state via low-field magnetization and ac susceptibility are introduced above in sect. 6.1. The low-field magnetization data are presented and discussed in the subsect. 6.3.1. Subsect. 6.3.2 is devoted for the ac susceptibility results. Furthermore, the results of frequency dependence of the in- and out-of-phase susceptibilities and the magnetic relaxation analysis are presented in subsect. 6.3.3. The magnetic phase diagrams are approached by the experimental results and presented in subsect. 6.3.4. Sect. 6.4 briefly concludes this chapter.

6.3 Results and discussions

6.3.1 *Magnetization*

The magnetization of $Co_3Sn_2S_2$ below T_C ~174 K was found to saturate rapidly at low fields of ~ 800 Oe. In the previously reported studies of the magnetization process of $Co_3Sn_2S_2$

at applied fields of 1 kOe, or higher, no significant anomalies were observed while a strong uniaxial anisotropy in magnetization $M(T, H)$ was reported[118,119]. Here, clear anomalies observed just below T_C in both the axial and plane components of $M(T, H)$ measured precisely at low magmatic fields are presented. The temperature dependences of the ZFC and FC $M(T, H)$ of $Co_3Sn_2S_2$ single crystal measured by applying various low magnetic fields are shown in Figs. 6.1. The magnetic transition temperature, T_C, of $Co_3Sn_2S_2$ shows a field- dependence. A magnetic transition abruptly appears at $T_C \sim 172$ K for magnetic fields below ~ 1 kOe applied along and perpendicular to the *c*-axis, as shown in Figs. 6.1(a) and (b), respectively. Curie-Weiss-like magnetization that merges after FC and ZFC regimes was observed above T_C by applying fields along or perpendicular to the *c*-direction.

In the axial magnetization, M_c (T, H), shown in Fig. 6.1(a), a hump-anomaly was observed in the FC M_c (T, H) at temperature $T_A \sim 126$ K for $H = 5$ Oe in *c* direction. The anomaly temperature T_A little increases by increasing H. The ZFC M_c (T, H) separates from the FC magnetization below T_C and show a significant dip-like anomaly at low magnetic fields in the intermediate temperature range between T_A and T_C. Both the hump-anomaly in FC M_c (T, H) and the minimum in the ZFC M_c (T, H) disappear at $H \geq 400$ Oe. The anomalous magnetization process is reproducible for crystals synthesized by the flux method or the modified Bridgeman method. One can note that the anomalies are observed at fields below the saturating fields of $Co_3Sn_2S_2$[113].

The magnetization in the *ab*-plane, $M_{ab}(T, H)$, displayed in Fig. 6.1(b), shows a similar hump-anomaly at T_A that is 126 K for 5 Oe and again shifts to higher temperatures by increasing H in the FC regime. On the other hand, the ZFC $M_{ab}(T, H)$ shows a broad minimum below T_C with a clear magnetic transition at T_A observed only at very low fields (below 150 Oe), as seen in the magnified ZFC behaviors in the inset of Fig. 6.1(b). The ZFC $M_{ab}(T, H)$ minimum broadness little decreases with increasing the magnetic field and still appears above 400 Oe. As the saturating field in the hard plane is higher than that along the easy axis, the anomaly is robust against higher magnetic fields up to ~ 1 kOe.

The chemical substitution by Fe for Co or In for Sn in $Co_{3-y}Fe_ySn_2S_2$ and $Co_3Sn_{2-x}In_xS_2$, respectively, preserves the anomalous transitions below T_C for y (or x) $\lesssim 0.8$, as clearly seen in Fig. 6.2. However, the hump anomaly in the FC $M_c(T)$ is hardly observed in $Co_{2.5}Fe_{0.5}Sn_2S_2$ single crystal.

6.3.2 *ac susceptibility of $Co_3Sn_2S_2$*

For more precise investigation of the exotic magnetic transitions observed just below the Curie temperature of $Co_3Sn_2S_2$, we have carefully measured the temperature-, field- and frequency-dependences of the ac susceptibility, χ_{ac}, after ZFC and FC in a wide range of frequencies f from 0.01 to 1000 Hz. An ac driving field H_{ac} = 1 Oe superimposed on dc fields H_{dc} of 0, 150 and 600 Oe were applied along [001]. Figure 6.3 shows the temperature evolution

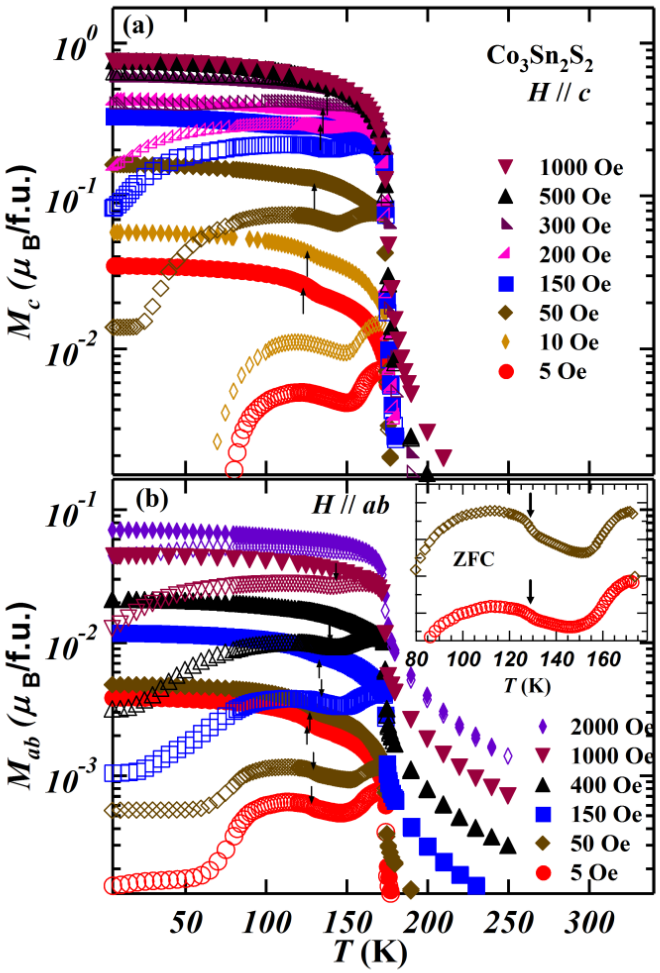

Figure 6.1: The temperature evolution of ZFC and FC magnetization, $M(T)$, of $Co_3Sn_2S_2$ flux-grown single crystal measured at the indicated low magnetic fields applied (a) along the c-axis and (b) perpendicular to the c-axis. The vertical arrows indicate the transition temperature T_A (see text). The inset of (a) shows the reproducible behavior of $M(T)$ of crystals grown from Sn-flux and by the modified Bridgeman method (see text). The inset of (b) shows a magnification of the ZFC $M(T)$ measured at very low fields.

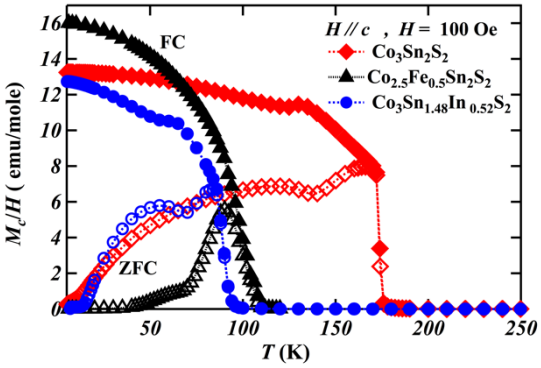

Figure 6.2: The temperature evolution of ZFC and FC magnetization, $M(T)$, of $Co_3Sn_2S_2$, $Co_3Sn_{1.48}In_{0.52}S_2$ and $Co_{2.5}Fe_{0.5}Sn_2S_2$ single crystals at a magnetic field of 100 Oe applied along c-axis.

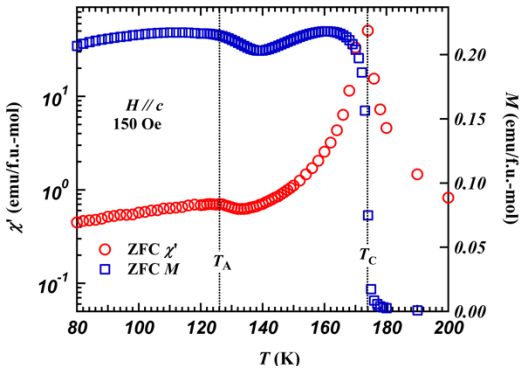

Figure 6.3: Temperature dependences of ZFC χ' (at f = 1 Hz, on left axis) and M (on right axis) of $Co_3Sn_2S_2$ at 150 Oe applied along the c-axis. The vertical doted lines indicate T_A (see text) and T_C.

of the ZFC in-phase ac susceptibility, $\chi'(T)$, of $Co_3Sn_2S_2$ single crystal measured at a frequency of 1 Hz and H_{dc} = 150 Oe applied along [001]. The $\chi'(T)$ behavior is compared (on a log-scale) to that of $M_c(T)$ measured at the same conditions. χ' shows two maxima separated by a minimum, one is a sharp peak at T_C and the other is located exactly at T_A.

In analogy to magnetic orders of multi-q state, the minimum exhibited by χ', as well as the magnetization, is a characteristic for the A-phase reported for the B20 chiral magnets just below T_C[159–162]. Due to the non-coplanar spin structure of skyrmions of antiparallel spins to the magnetic field at the core and curled spins in between the core and the peripheral, M and χ' show a minimum in the A-phase.

Figure 6.4 shows the temperature dependence of the ZFC and FC real and imaginary parts of the ac susceptibility, $\chi'(T, H)$ and $\chi''(T, H)$, at f = 1, 10, 100 and 1000 Hz for fields applied along [001]. $\chi'(T, 0)$ and $\chi''(T, 0)$ are shown on a log-scale in Figs. 6.4(a) and (b), respectively. A sharp peak in both χ' and χ'' was observed at T_C at all frequencies. The discontinues increase of χ'' at T_C again indicates unusual magnetic transition at low fields. Similarly to the dc magnetization shown above, a clear hump-anomaly in χ' is observed at T_A at all frequencies and coincide for ZFC and FC regimes. The out-of-phase susceptibility, χ'', exhibits anomalies at T_A only at 1 Hz and is more pronounced after ZFC, implying frequency dependence at the A-phase boundary. We found that the baseline of χ' (and χ'') is slightly higher at 1000 Hz by about 0.1 cm^3/f.u.-mole, which is likely due to an external effect of eddy currents that is significant at high f in metallic systems.

The sharp peak in both χ' and χ'' observed at T_C is maintained for low dc fields, as shown in Figs. 6.4(c) and (d) for 150 Oe. We observed that at 150 Oe the hump-anomalies in both χ' and χ'' at T_A is suppressed by increasing f. Although the peak of χ' at T_C is preserved at higher fields, χ'' peak at T_C almost disappears for H_{dc} higher than the critical field of the A-phase stabilization, as seen in Figs. 6.4(e) and (f) for H_{dc} = 600 Oe. However, the peak at T_A disappears in both χ' and χ'' at 600 Oe. These results indicate that the zero- and low-field state just below T_C is not the conventional ferromagnetic. $\chi'(T)$ and $\chi''(T)$ of similar characteristics have been observed in skyrmoins-hosting materials such as the B20 chiral magnets[159–161], indicating that the A-pashe observed for $Co_3Sn_2S_2$ is probably of a nontrivial magnetic structure (multiple q-state).

6.3.3 *Relaxation phenomena and frequency dependence of χ' and χ''.*

The existence of a non-zero χ'' of $Co_3Sn_2S_2$ particularly at T_C and T_A, as shown by the results presented in Fig. 6.4, implies a frequency dependence for both χ' and χ''. It was observed in the pure MnSi[160] and Cu_2OSeO_3[159], and doped $Fe_{0.7}Co_{0.3}Si$[161], chiral magnets that χ' (and χ'') is frequency-dependent only at the boundaries of the A-phase and its minimum in the A-phase does not depend on *f*. The influence of the frequency on the ac susceptibility of $Co_3Sn_2S_2$ is shown in details in Fig. 6.5 at temperatures far, inside and around the *A*-phase. Both ZFC χ' and χ'' displayed in Figs. 6.5(a) and (d) for H_{dc} = 150 Oe at temperatures inside and below the A-phase are weakly frequency-dependent. The increased value of χ'', below T^*, at high *f* can be ascribed as indication of *f*-dependence at higher *f*, that was found only in the MHz range in ferromagnetic materials[163], or likely is extrinsic due to the onset of eddy currents at low temperatures in this metallic system. While the frequency dependence at the FM to A-phase boundary is not detectable, the distinguishable χ' shows an increase around $T_A \sim 126$ K. At $T \sim 135$ K, corresponding to the minimum of χ' and χ'' inside the *A*-phase, χ'' is almost zero indicating stable spin structure that is quite robust against the small dynamic field.

Above the minimum and as approaching the high-temperature boarder of the A-phase, χ' and χ'' clearly decrease as *f* increases. Figs. 6.5(b) and (e) display the *f*-dependence of χ' and χ'' around the boundary temperature (T_C = 172 K) for H_{dc} = 150 Oe and the *f*-dependence exactly at T_C for different magnetic fields is shown in Figs. 6.5(c) and (f). χ' decreases monotonically with increasing frequency around the A-phase to paramagnetic boundary for low magnetic fields. Figs. 6.5(e) and (f) reveals a broad bell-shaped frequency dependence of χ'' at $\sim T_C$, which clearly reflects a distribution of the spin relaxation times averaged at the characteristic relaxation time $\tau_0 = 1/2\pi f_0$. Similar behaviors were observed in Cu_2OSeO_3[158,159]and $Fe_{0.7}Co_{0.3}Si$[161].

An overview of the relaxation processes beyond this kind of frequency dependence can quantitatively be revealed by employing the modified Cole-Cole formalism that includes a distribution of spin relaxation times[164,165]:

$$\chi(\omega) = \chi(\infty) + \frac{A_0}{1 + (i\omega\tau_0)^{1-\alpha}}\ , \qquad (6.1)$$

with $A_0 = \chi(0) - \chi(\infty)$, where $\chi(0)$ and $\chi(\infty)$ are the isothermal and adiabatic susceptibilities, $\omega = 2\pi f$ is the angular frequency and α is a parameter that provides a measure of the width of the relaxation frequencies distribution. $\alpha = 0$ reverts Eq. (6.1) to Debye model formalism with a

single relaxation time and $\alpha = 1$ gives an infinite width of the distribution. The real and imaginary parts of χ_{ac} can be extracted from Eq. (6.1) as[159,164,165]:

$$\chi'(\omega) = \chi(\infty) + \frac{A_0\,[1 + (\omega\tau_0)^{1-\alpha}\sin(\pi\alpha/2)]}{1 + 2(\omega\tau_0)^{1-\alpha}\sin\left(\frac{\pi\alpha}{2}\right) + (\omega\tau_0)^{2(1-\alpha)}}, \tag{6.2}$$

$$\chi''(\omega) = \frac{A_0\,(\omega\tau_0)^{1-\alpha}\cos(\pi\alpha/2)}{1 + 2(\omega\tau_0)^{1-\alpha}\sin\left(\frac{\pi\alpha}{2}\right) + (\omega\tau 0)^{2(1-\alpha)}}, \tag{6.3}$$

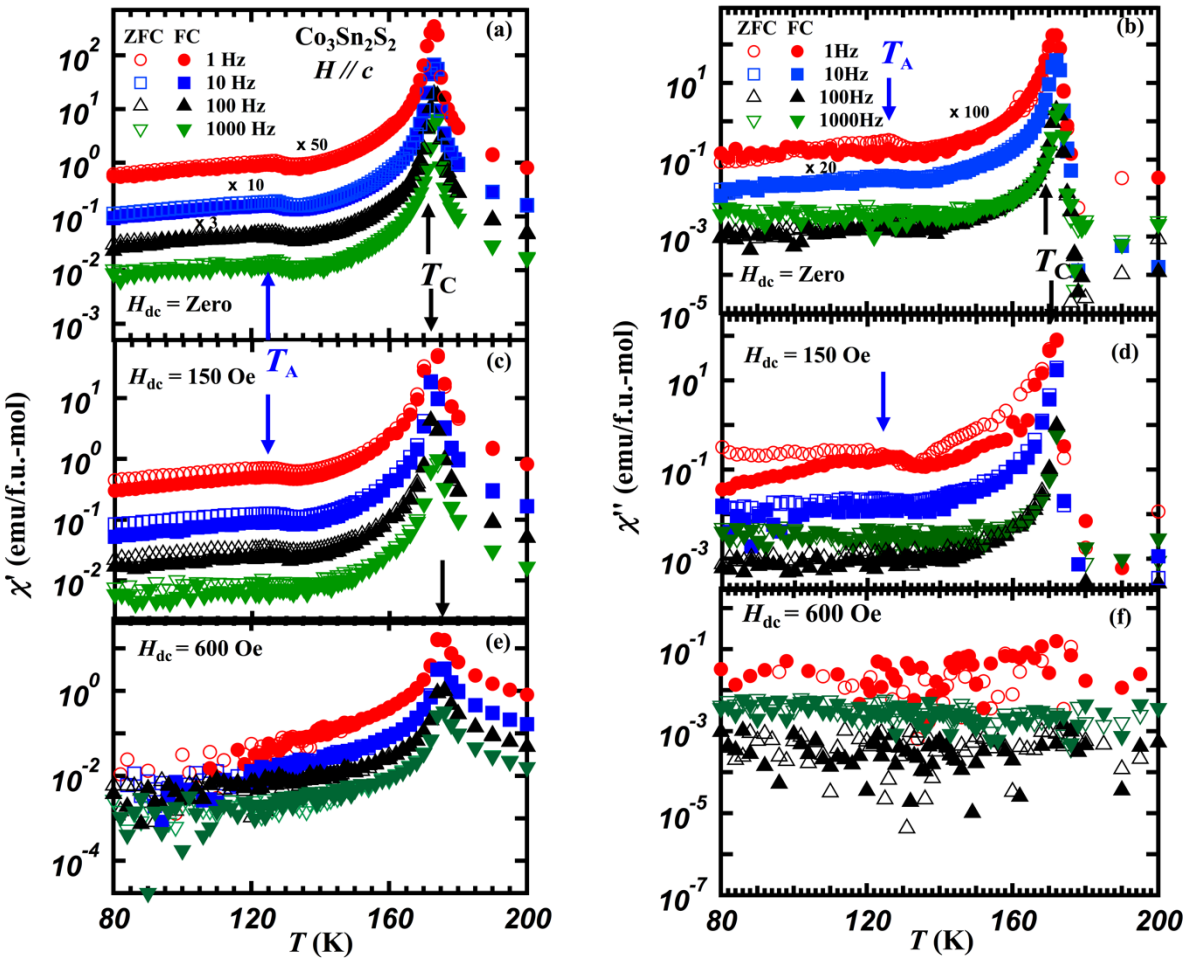

Figure 6.4: Thermal variation of FC and ZFC χ' and χ'' of $Co_3Sn_2S_2$ measured at different frequencies from 1 to 1000 Hz and for magnetic fields H_{dc} of zero (a),(b); 150 Oe (c),(d) and 600 Oe (e),(f), respectively, applied along [001]. The vertical arrows indicate T_C and T_A (see text). For clarity purpose, the curves for some frequencies have been shifted vertically with respect to the base line by multiplying their data to the number indicated next to each of them.

and subsequently their interrelation (the so-called Cole-Cole formalism) can be deduced as:

$$\chi''(\omega) = A_0\frac{\tan\left(\frac{\pi\alpha}{2}\right)}{2} + \left[{A_0}^2\frac{\tan^2\left(\frac{\pi\alpha}{2}\right)}{4} + \left(\chi'(\omega) - \chi(\infty)\right)\left(A_0 + \chi(\infty) - \chi'(\omega)\right)\right]^{\frac{1}{2}} \tag{6.4}$$

The fitting results to Eqs. (6.2), (6.3) and (6.4) around and at T_C are shown as solid lines in Figs. 6.5 (b),(c) and (e),(f) and Fig. 6.6, respectively. The fitting parameters are shown as

functions of temperature and field in Fig. 6.7. An estimated α varying around 0.6 at the PM to A-phase transition indicates a distribution of relaxation times.

A characteristic frequency-dependence particularly for χ" with drastically changed characteristic frequency, f_0, is observed around the paramagnetic to A-phase transition. Just above T_C, e.g. at T = 173 K in Fig. 6.5(e), ZFC χ' and χ" shows a frequency-dependence only at high f and remains almost constant below 10 Hz. This behavior is due to the rapid relaxation of the paramagnetic state. χ" exhibits f_0 much higher than the range of measurement at $T > T_C$, typically ~ 58 kHz at 173 K for 150 Oe. With decreasing temperature, f_0 decreases and can be observed within the range of measurement at T_C, ~ 25Hz at 172 K. Below T_C, lower f_0 was observed, ~ 0.1 Hz at 171 K. Such narrow temperature window at the A-phase to PM boundary where the characteristic frequency is around the middle of such an experiment frequency range have been observed in Cu_2OSeO_3[158]. The slow relaxation just below T_C indicates freezed-like moments in a highly irreversible and stable state within the A-phase in $Co_3Sn_2S_2$ which is the case of skyrmions phase in Cu_2OSeO_3[158,159]. On the other hand, the parameter α is weakly changed and almost constant against temperature.

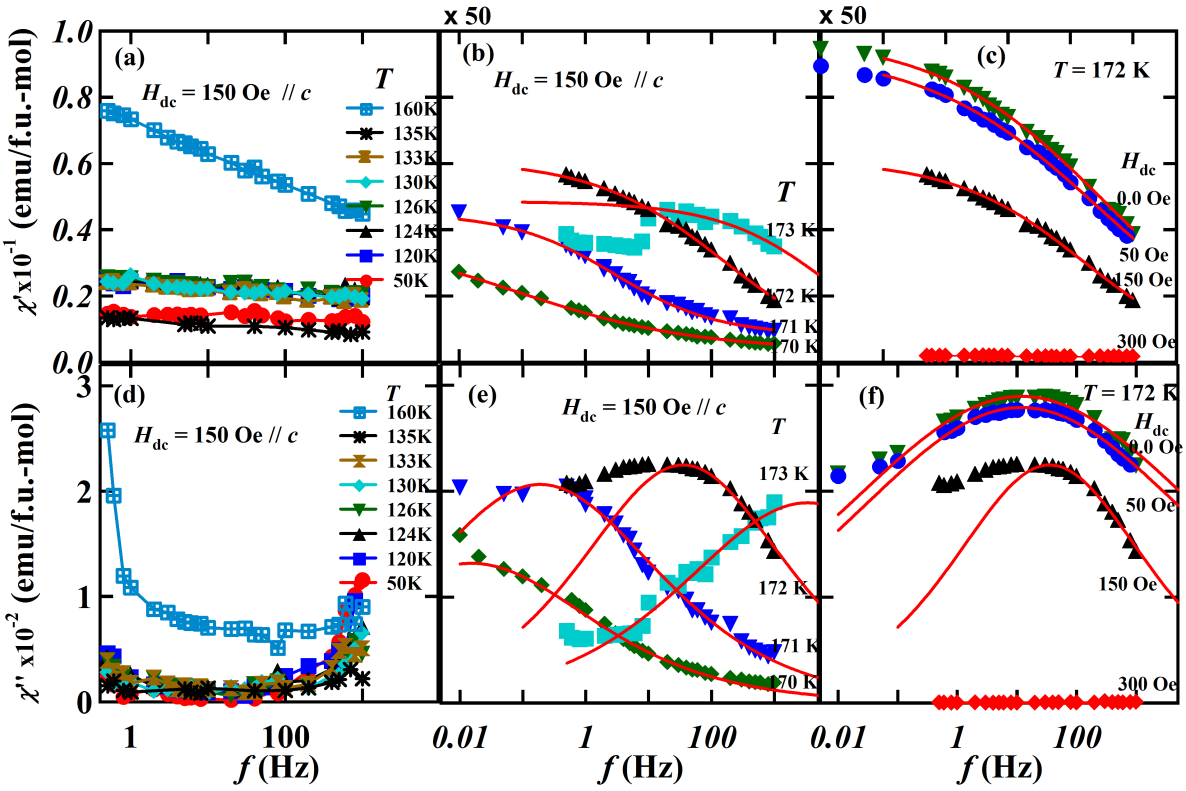

Figure 6.5: Frequency dependence of ZFC (a-c) χ' and (d-f) χ" of $Co_3Sn_2S_2$ at indicated temperatures (around and far from T_A) and around 172 K (T_C) for a magnetic field of 150 Oe applied along [001].

Actually an asymmetric bell-shaped f-dependence of χ" was observed at 172 K for H_{dc} = 150 Oe. However, we observed that the dependence becomes more symmetric around f_0 without dc bias field or at very low applied fields, as seen in Figs. 6.5 (f) show the f-dependences of χ" at 172 K for different magnetic fields. The spins at the PM to A-phase transition exhibit a distribution of relaxation processes of times that is averaged around a characteristic time τ_0 of about 13 ms ($f_0 \sim$ 12 Hz) as indicated by the zero-field relaxation and relaxation at very low fields. As the applied field increases approaching the triple boundary of the PM, FM and A-phase states, the relaxation time becomes asymmetrically distributed and averaged at lower τ_0. At the PM to FM transition, as shown at 172 K for 300 Oe, χ' becomes almost independent on f and χ" vanishes in the experiment frequency range. The results indicate a zero- and low-field transition to nontrivial spin structure just below T_C that remains at low magnetic fields.

The same characteristics at temperatures around T_C are inferred from the Cole-Cole variation of χ" versus χ' shown in Fig. 6.6. In contrast to the semicircle plot in case of the Debye relaxation process of one relaxation time, the Cole-Cole plot due to a distribution of relaxation times is an arc centered at χ' corresponding to f_0[163]. The central angle of the arc is equal to $(1-\alpha)\pi$. The χ" versus χ' plots of $Co_3Sn_2S_2$ are parts of arcs at temperatures below T_C and an asymmetric arc at T_C for H_{dc} =150 Oe. The arc plot becomes more symmetric at zero and lower magnetic fields. Fitting the data to Eq. (6.4) can again conduct quantitative insight beyond the relaxation process resulting in parameters such as the relaxation time distribution width indicated by α.

The spin relaxation of $Co_3Sn_2S_2$ at the high temperature boundary of the A-phase shows a parameter $\alpha > 0$ that is almost invariant against temperature and magnetic field as shown in Fig. 6.7(a). Fitting the data of χ" and χ' vs. f gives values averaged around 0.65 and 0.6, respectively, and the Cole-Cole plots fitting gives averaged α of 0.5. Fig. 6.7(b) shows the temperature variation of the characteristic frequency (log f_0 vs. $1/T$) around T_C, where f_0 increases rapidly with T. As magnetic moments are coupled to the crystal lattice through the spin-orbit interaction, the spins exchange energy with lattice via phonons and magnons and the relaxation time decreases with temperature. In simple cases the relaxation process is thermally activated and can be described by an Arrhenius law $f_0 = A \exp(-\Delta/T)$, Δ is the energy barrier. As seen in Fig. 6.7(b), the temperature dependence of f_0 in $Co_3Sn_2S_2$ spin relaxation around T_C does not exactly follow the Arrhenius law. Even the linear fit of log(f_0) vs. $1/T$ above 170 K gives a very large and unphysical value of Δ of 10^5 K. Thus the relaxation at low-fields

magnetic transition of $Co_3Sn_2S_2$ is not a simple spin-lattice relaxation and much complex to be described by a thermal activation picture. The relaxation time is little changed by increasing the applied field as shown in the inset of Fig. 6.7(b).

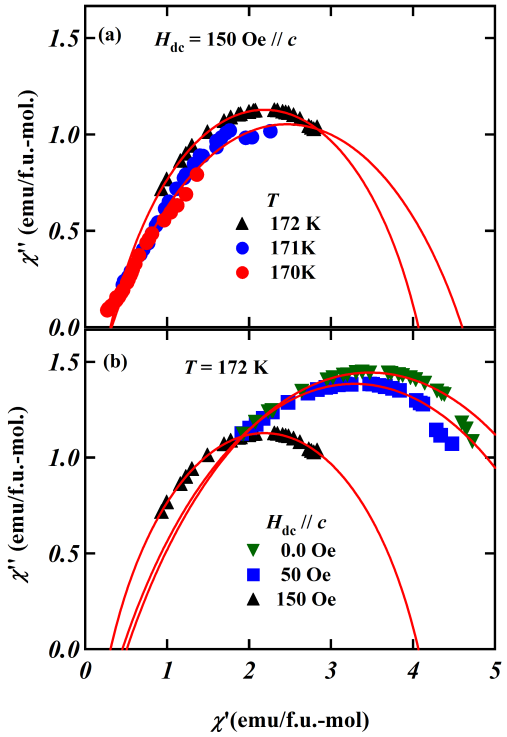

Figure 6.6: Cole-Cole plots of $Co_3Sn_2S_2$ (a) for 150 Oe applied along *c*-axis at temperatures close to T_C and (b) for various magnetic fields at T_C. The solid lines represent the fits of the experimental data to Eq. (6.4).

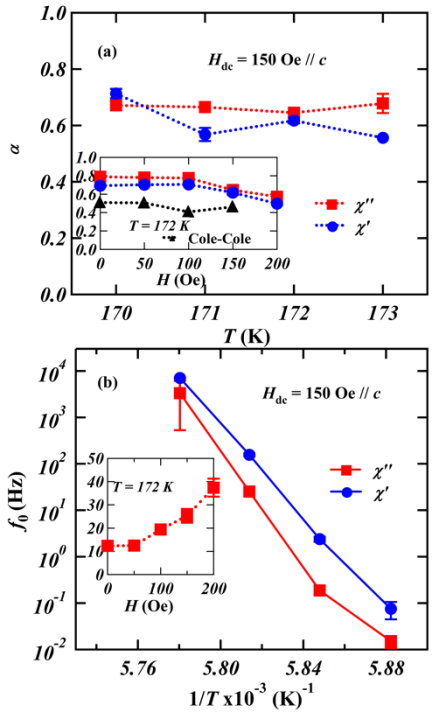

Figure 6.7: The temperature dependences of (a) the distribution width parameter of relaxation times, α, and (b) the characteristic frequency, f_0, of $Co_3Sn_2S_2$ for 150 Oe. The field dependences of α and f_0 at 172 K are shown in the insets of (a) and (b), respectively.

6.3.4 *Magnetic phase diagrams*

Here we present the magnetic phase diagrams of $Co_3Sn_2S_2$ based on the above magnetization and ac susceptibility data. Figures 6.8(a - c) illustrate the H vs. T phase diagrams in the case of applied magnetic fields along and perpendicular to the *c*-axis, respectively. The A-phase of possible skyrmions extends to a wide temperature range (50 K) below T_C in $Co_3Sn_2S_2$. In contrast to the zero-field stabilized helical and cycloidal orders, as a result of the balance between a strong ferromagnetic and a weaker DM interactions, in skyrmions-hosting chiral and polar magnets[32,52], respectively, the A-phase in $Co_3Sn_2S_2$ is stabilized at zero field. The magnetic phase diagram of $Co_3Sn_2S_2$ may indicate strong DM interactions which is inherent in the Co-kagomé sublattices. Moreover, our results indicate an equilibrium state of

the possible skyrmions in $Co_3Sn_2S_2$, in contrast to the stabilized metastable skyrmion phase recently observed at zero field in β-Mn type Co-Zn-Mn chiral magnets only after FC via the equilibrium skyrmion state[166]. Magnetic fields exceeding the saturating field applied in *c*-direction just below T_C overcome the DM interactions and induce a field-polarized FM state, as seen in Fig. 6.8(b) and magnetization and ac susceptibility results in Figs. 6.1 and 6.4.

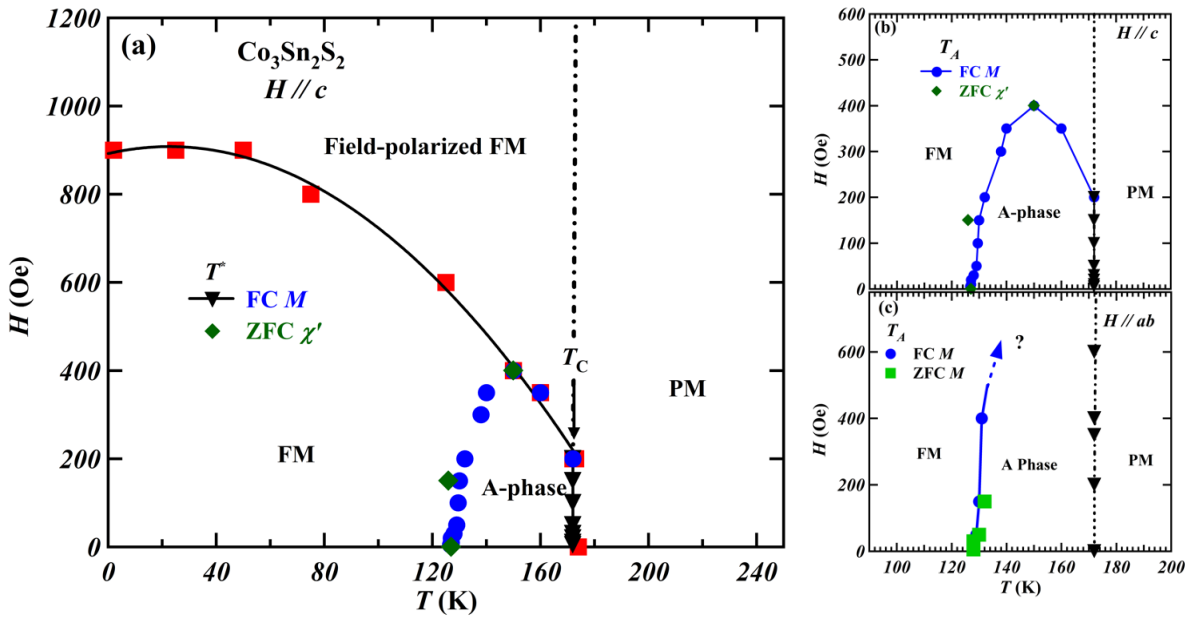

Figure 6.8: Magnetic phase diagrams as a function of the temperature and applied magnetic field along the *c*-axis (a). The spin-polarizing field is indicated by the red solid squares and the eye-guiding solid line. The A-phase is bounded by the T_C at 172 K and the below T_A obtained from the FC M_c (shown by blue circles) and the χ' anomalies (green marks). Dashed line indicates T_C at higher magnetic fields. (b) magnification of the phase diagram of $H \parallel c$. (c) the magnetic phase diagram obtained by applying magnetic field in the *ab*-plane. Squares are the low-temperature A-phase boundary obtained from the FC M_{ab} and green marks from the ZFC transitions. Lines are for eye guidance. T_C is again indicated by the dashed line.

The A-phase in $Co_3Sn_2S_2$ observed by applying fields in *ab*-plane survives in a wider range of magnetic field as seen in Fig. 6.8(c) and the dip-like anomalies in ZFC $M_{ab}(T, H)$ appear at fields higher than 400 Oe in Fig. 6.1. The extended A-phase for $H \perp c$ is due to the much weaker ferromagnetic exchange against the DM interaction in the *ab*-plane. The low temperature boundary of the A-phase is shown at low fields in Fig. 6.8(c) based on the emergent transitions in both FC and ZFC $M_{ab}(T, H)$ seen in Fig. 6.1.

The stability of skyrmion lattices over an extended temperature and field below T_C has been realized in ultrathin films of the non-centrosymmetric chiral magnets FeGe[49] and MnSi[167]. However the A-phase of skyrmions was observed in small areas of the *H*-*T* diagram for bulk

chiral magnets[32]. Largely extended A-phase phase has recently been observed in centrosymmetric hexagonal magnets hosting biskyrmions[55]. Beyond the possible individual skyrmions stabilization by the competing DM interaction, the large area of the A-phase in the *H-T* diagram as well as the centrosymmetric crystal structure support likely biskyrmion textures in $Co_3Sn_2S_2$. To address these expectations, further small-angle neutron scattering (SANS) experiments or at least spin-polarized scan tunneling microscopy (STM) or Lorentz TEM microscopy are needed to shed light on the bulk nature of the magnetic structures of $Co_3Sn_2S_2$.

6.4 Conclusion

The precise measurement of the low-field magnetization process of $Co_3Sn_2S_2$ provides a quantitative approach to the *H-T* phase diagram. Magnetic transitions at the boarders of an anomalous pocket, A-phase, as indicated by the dc magnetization and the ac susceptibility were observed just below the magnetic order temperature, T_C. The disappearance of the anomalous transitions at higher fields suggests unconventional spin textures different from the ferromagnetic state in the A-phase, probably of magnetic skyrmions. Frequency-distributed spin relaxation process of characteristic relaxation times reaches 10 seconds have been observed around the *A*-phase boundary (PM to *A*-phase transition).

CHAPTER 7

7 Transport Properties of Co-shandites: Emergent Unconventional Electronic State of $Co_3Sn_{2-x}In_xS_2$

7.1 Motivations and Purpose

Quasi-two-dimensional (Q2D) strongly correlated electron systems often exhibit unusual electronic properties due to the strongly enhanced thermal and quantum fluctuations[10,168]. For instance, superconductivity in layered cuprates and iron-based superconductors[12–16], quantum-criticality of two dimensional fluctuations origin in heavy fermion systems[17,18], successive phase transitions and electronic instabilities in Layered transition metal dichalcogenides[19–21] and tunable Fermi surface topology and Lifshitz transition in Q2D electronic states[169–172] are reported. On the other hand, and as described in chapter 1, subsect. 1.3.4, the extraordinary 2D Dirac materials, graphene and its resembling materials, show fascinating physical properties of massless Dirac fermions [22–24,173–175]

Beside the lattice distortions, an unusual electronic state can emerge by the band-filling in Q2D systems. For example, electronic structure variations with high thermoelectric properties are induced by band-filling in $YBa_2Cu_3O_{7-\delta}$[176] and $SrTiO_3$[177] ceramics and the τ-type organic conductors[178,179]. Moreover, a dramatic Lifshitz transition occurs in Na_xCoO_2 in a narrow range of $0.620 < x < 0.621$[169] as well as in the electron-doped iron arsenic superconductors at the boarder of the superconducting phase[172]. Furthermore, competing topological electronic states may be tuned by carriers adding to a parent layered compound. A Dirac cone dispersion with the cone apex locates at the Fermi level was revealed below a spin-density-wave temperature in the electronic structure of $BaFe_2As_2$, the parent compound of 122 iron-pnictide high-temperature superconductors[180]. Tunable band gap and anisotropic Dirac semimetallic state has also been observed in the K-doped black phosphorus of few layers[181,182]. The search for new materials with the structure of weakly-coupled layers has a lot of interest to observe unconventional electronic states exhibiting exotic phenomena.

The $Co_3Sn_2S_2$ shandite has recently been introduced as a promising Q2D material exhibiting interesting physical properties upon band filling[101,114,115,117,127]. The crystal structure of stacked metallic layers, the monotonic increase of c/a by In-substitution, the highly Q2D character of magnetism reported here in chapter 4, and the tunable Fermi energy previously reported by the thermopower sign change around $x \sim 1.0$[83,127] and supported by the sign change

of the Hall coefficient presented in chapter 5; all imply an unconventional Q2D electronic state of Co-shadites. However, the electronic state of Co-shandite solid solutions has never been studied using single crystals. In order to shed light on the electronic structure of $Co_3Sn_{2-x}In_xS_2$ solid solution, systematic measurements of the temperature variations of the in- and out-of-plane electrical resistivity $\rho(T)$ as well as the heat capacity $c_p(T)$ of $Co_3Sn_{2-x}In_xS_2$ single crystals ($0 < x \leq 2$) have been performed. The results are presented and discussed in this chapter.

7.2 Outline

The interest of the Q2D electronic states of the layered materials and the rich physics emerges by band filling in some compound, that promoted the study of $Co_3Sn_{2-x}In_xS_2$ electronic state using single crystals, are described above in sec 7.1. The experimental results of the anisotropic electrical resistivity and the specific heat measured systematically for $Co_3Sn_{2-x}In_xS_2$ ($0 < x \leq 2$), at zero magnetic field, are presented in subsects. 7.3.1 and 7.3.2, respectively. All the results are extensively discussed in sect. 7.4. A conclusion of this chapter is given in sect. 7.5.

7.3 Experimental Results

7.3.1 Electrical resistivity

The previously reported transport properties observed above 100 K using polycrystalline samples of $Co_3Sn_{2-x}In_xS_2$, was emphasized in the current study first by using polycrystalline samples in a further extended temperature range down to 4 K, prior to the detailed study using single crystals of $Co_3Sn_{2-x}In_xS_2$ ($0 < x \leq 2$). The temperature dependences of the electrical resistivity ρ (T) of polycrystalline samples of $Co_3Sn_{2-x}In_xS_2$ is shown at indicated x in Fig. 7.1. The largely enhanced resistivity of semimetallic-like behaviors around $x = 1.0$ is clearly observed.

The temperature dependences of the absolute in- and out-of-plane electrical resistivity, $\rho_{ab}(T)$ and $\rho_c(T)$, of $Co_3Sn_{2-x}In_xS_2$ with various indicated x measured in zero magnetic field are shown in Figs. 7.2 and 7.3. The parent compound, $Co_3Sn_2S_2$, exhibits a metallic behavior in both in- and out-of-plane with a relatively large residual resistivity, ~ 0.13 mΩ cm in ab-plane. A kink is pronounced around 174 K in $\rho(T)$, as well as in the polycrystalline samples, and shifts systematically to low temperatures by In-substitution. This kink-like anomaly is attributed to the reduced spin disorder scattering below the Curie temperature in the ferromagnetic compounds. $\rho(T)$ is little reduced first for x up to 0.34 then it turns to increase drastically for $0.51 \leq x \leq 0.9$ and show clear semimetalic behavior in a narrow region of $0.9 \leq x \leq 1$. Instead

of the predicted conventional thermally activated semiconducting behavior[114], a nonmetallic logarithmic divergence of $\rho(T)$ of $x = 0.97$ is observed as T decreases, see the inset of Fig. 7.3, which indicates that no gap opens at $x \sim 1.0$. A largely anisotropic resistivity is observed for $x = 0.97$ as shown in Fig. 7.3. The metallic electronic state is restored again and much enhanced for higher indium concentrations. The end member, $Co_3In_2S_2$, exhibits a higher

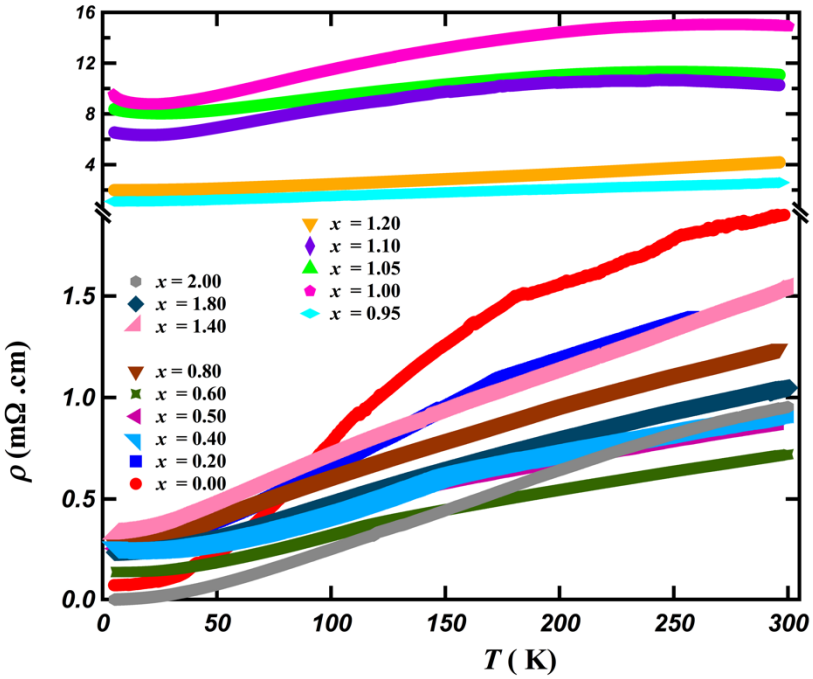

Figure 7.1: The T-dependence of the absolute resistivity, ρ, of $Co_3Sn_{2-x}In_xS_2$ polycrystalline of various In concentration x.

metallic conduction than $Co_3Sn_2S_2$ at all temperatures in both directions with in-plane residual resistivity of ~ 0.0015 mΩ cm.

In Fermi liquid (FL) metals, the electrical resistivity at low temperatures obeys $\rho(T) = \rho_0 + A\,T^2$, where ρ_0 is the residual resistivity and A is a constant related to the scattering due to electron-electron interaction. Fig. 7.4 shows the in-plane electrical resistivity of $Co_3Sn_{2-x}In_xS_2$ as a function of T^2 at low temperatures. A good linear fit at low temperatures indicates the FL state which is maintained at low and high In concentrations. An expected deviation from the quadratic variation of $\rho(T)$ in the semimetallic phase around $x = 1.0$ is observed with upturns at low temperatures. The obtained values of A with applying the electric current in the ab-plane, A_{ab}, and c-direction, A_c, of the metallic phases of $Co_3Sn_{2-x}In_xS_2$ are presented in table 7.1. A large increase of A is observed approaching $x = 0.8$ which indicates mass enhancement of the charge carriers as a result of the increased many-body interactions in the vicinity of the QCP. While the in- and out-of-plane resistivities of $Co_3Sn_{2-x}In_xS_2$ show qualitatively similar

behaviors against temperature, a quantitatively enhanced anisotropy, ρ_c/ρ_{ab}, by In-substitution is seen in Figs. 7.2 and 7.3. ρ_c/ρ_{ab} shown below against In-substitution in Fig. 7.6(b) exhibits a general increase as In increases. The pure Sn compound, $Co_3Sn_2S_2$, shows ρ_c/ρ_{ab} of ~ 2.7 at 5 K with higher out-of-plane resistivity at all temperatures. On the other hand, the counterpart, $Co_3In_2S_2$, shows ρ_c/ρ_{ab} ~ 42 at 5 K. The large anisotropic conductivity in $Co_3In_2S_2$ has been

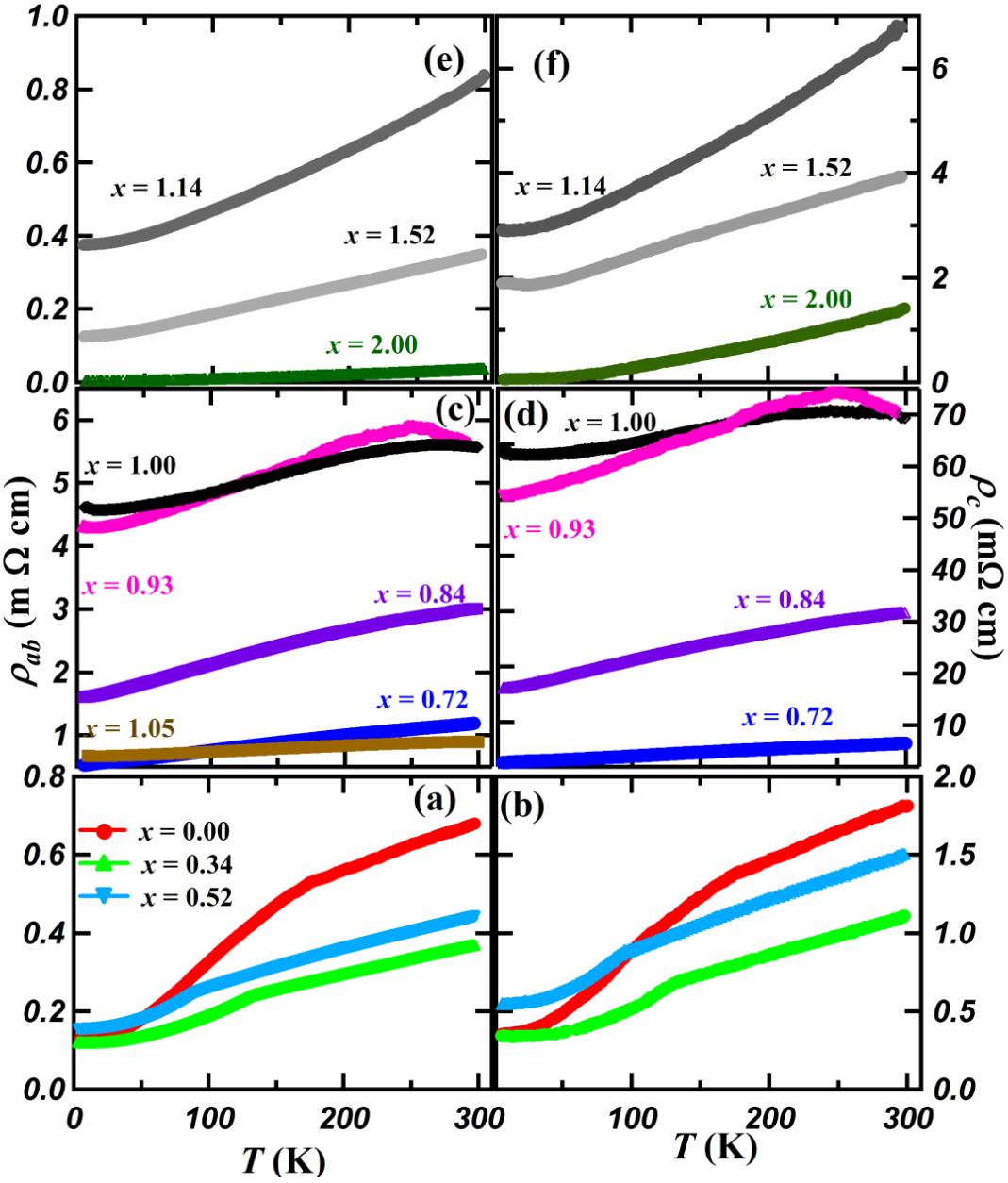

Figure 7.2: The *T*-dependence of the absolute (a), (c) and (e) in-plane resistivity, ρ_{ab}, and (b), (d) and (f) out-of-plane resistivity, ρ_c, of $Co_3Sn_{2-x}In_xS_2$ single crystals of various In concentration *x*.

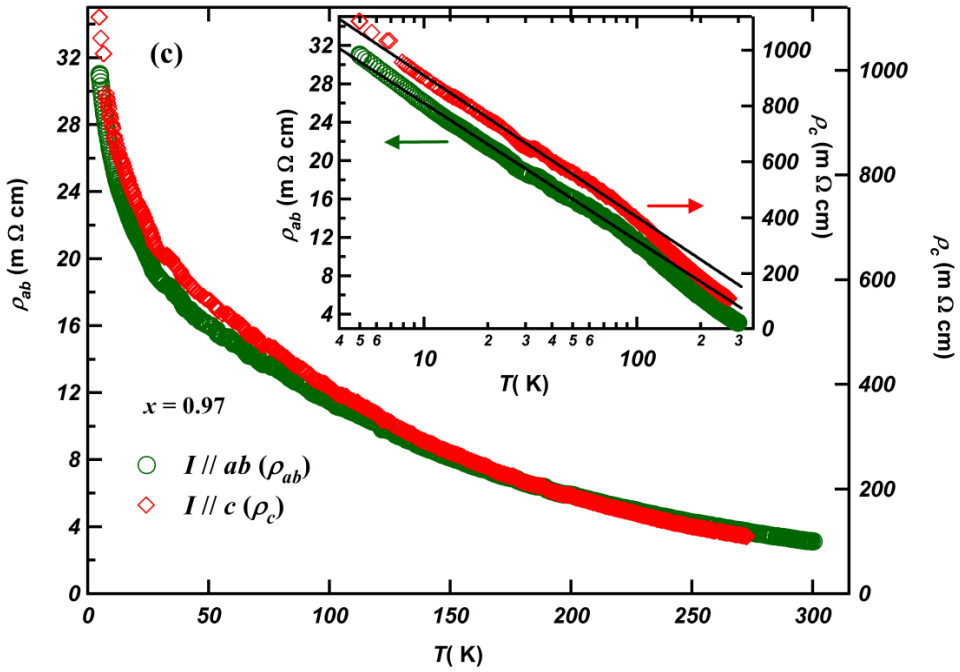

Figure 7.3: The temperature evolution of the in- and out-of-plane resistivity, ρ_c and ρ_{ab}, of $Co_3Sn_{1.03}In_{0.97}S_2$ single crystal exhibiting logarithmic divergence as the temperature, T, decreases. The inset shows ρ_c and ρ_{ab} vs log T, symbols are the experimental data and solid lines are linear fits.

predicted based on recent band structure calculations[117]. The general enhancement of the anisotropy of $\rho(T)$ by the In-substitution clearly indicates a change of the electronic state of the Co-shandite $Co_3Sn_{2-x}In_xS_2$ from 3-dimensional to 2-dimensional-like one, i.e. enhancement of the Q2D electronic state. The observed enhanced Q-2D electronic state is directly related to the structural distortions in $Co_3Sn_{2-x}In_xS_2$ caused by In-substitution due to the M1-5p$_z$ orbitals exhibiting weaker bonds to Co-3d in case of In than those of Sn[117].

A pronounced peak in the x-dependence of ρ_{ab} and ρ_c resistivity measured at 5 K and the anisotropy in the electrical resistivity, ρ_c/ρ_{ab}, is observed in a narrow region at $x \sim 1.0$ as shown in Figs. 7.6(a) and (b). Its known that the resistivity in metallic solid solutions usually exhibits some enhancements at very low temperatures in high doping levels due to the additional defects and impurities in the crystal structure. Distinctly, the resistivity of $Co_3Sn_{2-x}In_xS_2$ almost diverge very close to $x = 0.97$ at low and high temperatures indicates nonmetallic electronic state. Moreover, its drastic increases in a narrow region indicates an unusual electronic state.

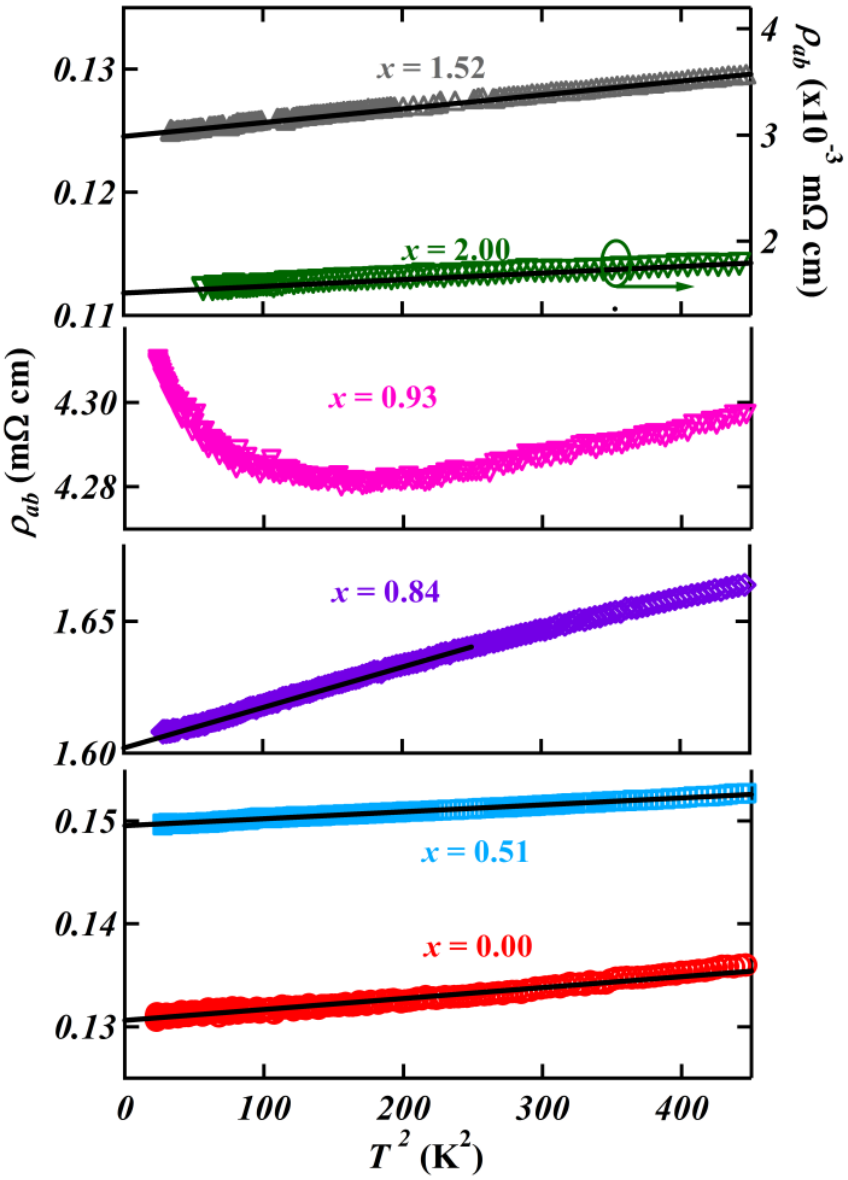

Figure 7.4: In-plane electrical resistivity of $Co_3Sn_{2-x}In_xS_2$ of indicated In concentrations at low temperatures as a function of T^2. solid lines are the linear fit to $\rho(T) = \rho_0 + A T^2$ at low temperatures (see text).

7.3.2 Specific heat

The behavior of the heat capacity $c_p(T)$ of $Co_3Sn_{2-x}In_xS_2$ single crystals in zero magnetic field is shown at low temperatures in Fig. 7.5(a) in the manner of $c_p(T)/T$ vs. T^2, shown data are in the ferromagnetic ($0.0 \leq x \leq 0.8$) and paramagnetic ($x \geq 0.84$) regions. Our results of $c_p(T)$ for $x \geq 0.84$ do not show any anomaly in the temperature range of measurement indicating

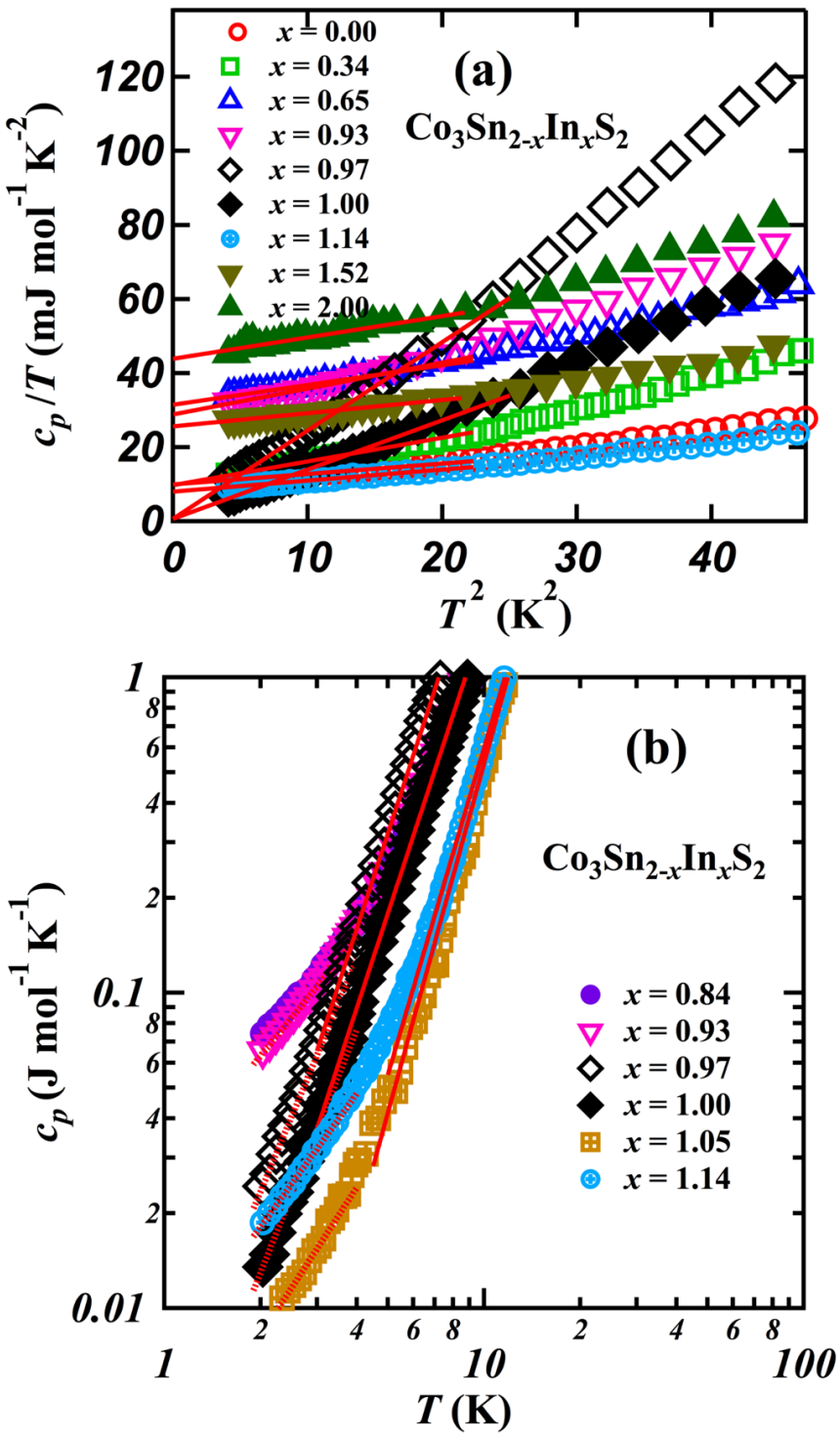

Figure 7.5: (a) Temperature behavior of the molar heat capacity $c_p(T)$ of single crystalline solid solution $Co_3Sn_{2-x}In_xS_2$ in zero magnetic field in the form c_p/T vs T^2 at low temperatures. The solid lines are the linear fits, see text. (b) log c_p vs log T around x = 1.0. Dashed and solid lines are the linear fits at low and high temperature, respectively.

no transitions occur below 20 K. The total specific heat of the FL metals is given by: $c_p(T) = \gamma T + \beta T^3$, where γ is the Sommerfeld coefficient of the electronic linear term and β is a fitting

coefficient for the phononic Debye T^3 term. Fitting the data up to 6 K yields γ = 9.8 mJ mol^{-1} K^{-2} and β of 0.305 mJ mol^{-1} K^{-4} for $Co_3Sn_2S_2$ that correspond to DOS(ε_F) of 2.369 ×10^6 states /(eV f.u.) and an initial Debye temperature, θ_D, of 355 K. The counterpart $Co_3In_2S_2$ exhibits γ = 44.5 mJ mol^{-1} K^{-2} and β of 0.534 mJ mol^{-1} K^{-4} corresponding to DOS(ε_F) of 2.369 ×10^6 states /(eV f.u.) and θ_D of 300 K. The fitting results of $Co_3Sn_2S_2$ and $Co_3In_2S_2$ satisfactorily agree with the recently reported data using single crystal of $Co_3Sn_2S_2$ and polycrystalline sample of $Co_3In_2S_2$[119]. Except for x = 0.97 and 1.0, samples of other indium concentrations exhibit an obvious value of γ and a comparable lattice contribution to the specific heat indicated by the slope at low temperatures, β. In a very narrow region at x ~ 1.0, the slope drastically increases and the intersection with the vertical axis becomes almost zero, as seen below in Figs. 7.6(c) and (d).

Enhancements of γ and hence DOS(ε_F) are observed in the metallic regions as approaching x = 0.84 and x = 2.0, Fig. 7.6(d). The former is simply due to the strong spin fluctuations in the vicinity of the QCP while the enhanced effective mass of electrons approaching the latter is little argumentative as $Co_3In_2S_2$ is a paramagnet. However, a weak magnetic instability of $Co_3In_2S_2$ has been predicted in recent theoretical calculations[117]. In consistence with these calculations, an enhanced temperature-independent susceptibility, χ_0, with broad anomaly at ~ 50 K observed for $Co_3In_2S_2$[111] may explains the strong electron correlation of this compound. For this purpose, the enhanced mass of electrons in highly strong correlated electron systems can be compared to χ_0 by the well-known Wilson ratio, WR = $\left(\frac{\pi^2 k_B^2}{3\mu_B^2}\right)\frac{\chi_0}{\gamma}$, where μ_B and k_B are the Bohr magneton and Boltzmann constant and χ_0 and γ are expressed in emu/mol and erg /K^2 mol, respectively. WR increases from unity for free electron gas to 2 for strongly correlated electron systems[183]. Figure 7.7 shows χ_0 against γ on a log-log scale for the paramagnetic metals of $Co_3Sn_{2-x}In_xS_2$ with x > 1.0 compared to the data of other highly strong correlated compounds[184]. The data of In-rich $Co_3Sn_{2-x}In_xS_2$ exhibits values of RW close to 2 (solid line) rather than 1 (broken line). The observed WR in $Co_3Sn_{2-x}In_xS_2$ suggests again highly strong correlation effects.

The phononic specific heat coefficient, β, shown in Fig. 7.6(c) is almost constant and averaged around 0.38 mJ/(mol K^4) in the metallic regions of low and high In concentrations. However, the estimated coefficient of the T^3-term drastically increases in the anomalously nonmetallic region at x ~ 1.0 indicating either significant lattice contribution or other emergent T^3-dependent contribution to the specific heat at low temperatures. On the other hand, the linear

dependence coefficient γ shows a drastic decrease in the nonmetallic region of $Co_3Sn_{2-x}In_xS_2$ and almost vanishes at $x \sim 1.0$, as seen in Fig. 7.6(d).

Fitting the specific heat data to a general expression, $c_p(T) = \delta T^{\alpha}$, may help to identify the temperature exponent at low temperatures. Fig. 7.5(b) shows the $c_p(T)$ data of $Co_3Sn_{2-x}In_xS_2$ on a log-log scale. Whereas, $Co_3Sn_{2-x}In_xS_2$ of various x have a slope of $\alpha \simeq 3$ at high temperatures indicating phonons-contributed specific heat, the slope of $\alpha \simeq 1$ below 4 K that indicates the dominant electronic contribution at low temperatures is changed to $\alpha \geq 2$ for $x \sim 1.0$. The fitting results for different x in $Co_3Sn_{2-x}In_xS_2$ are listed in table 7.1.

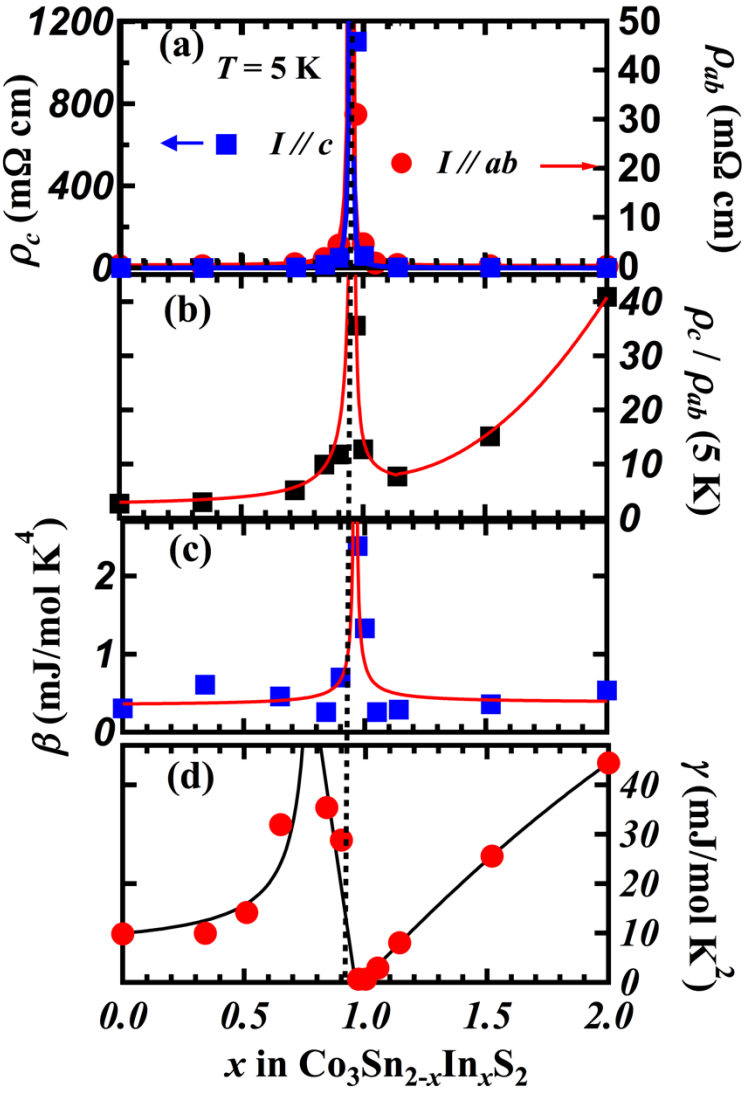

Figure 7.6: In concentration dependences of (a) electrical resistivity ρ at 5 K, (b) the anisotropy in resistivity at 5 K, ρ_c / ρ_{ab} [5 K] , (c) the phononic specific heat coefficient and (d) Somerfeld's coefficient, γ. Solid lines are for eye guidance. The dashed vertical line indicates the highly nonmetallic In concentration expected to locate at a Dirac point, see text.

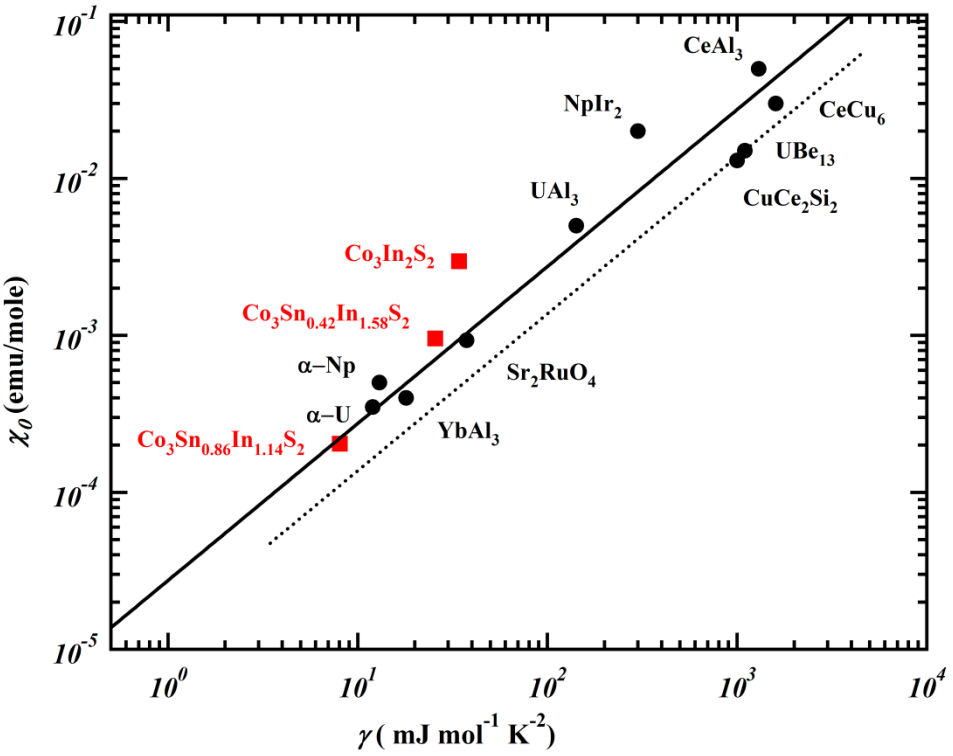

Figure 7.7: The T-independent paramagnetic susceptibility, χ_0, presented against somerfeld coefficient, γ, (Wilson plot) for highly strong correlated compounds[184] including the In-rich compounds of $Co_3Sn_{2-x}In_xS_2$ on a log-log scale. Solid and broken lines correspond to Wilson ratios of 2×10^{-4} and 1×10^{-4}, respectively, (see text).

7.4 Discussion

The transport properties of $Co_3Sn_{2-x}In_xS_2$ provide an experimental evidence of the Q2D metallic state that is conventionally enhanced by the increased crystal structural distortion. However, the increased resistivity with logarithmic divergence as T decreases and its high anisotropy at $x \sim 1.0$ may be attributed to an electronic effect of In. Semiconducting gap opening, that is experimentally only approximated, was predicted for $x = 1.0$ based on DFT calculations and attributed to an electronic sink formed by bonds of the degenerated In2-5p$_{x,y}$ orbitals[117]. The highly 2D-like semimetallic state associated with dramatic decrease of DOS(ε_F) and the emergent T^{α}-dependent $C_p(T)$ with $2 \leq \alpha \leq 3$ at low temperatures in a narrow region at $x \sim 1.0$, seen in Fig. 7.6, is quite unconventional.

Actually, the logarithmically divergent resistivity with decreasing temperature has been observed in the normal state of some doped superconductors[185–187] and in the hydrogen deficient $YH_{3-\delta}$[188] and has been explained based on the conventional 2D weak localization or

the Kondo scattering model[189,190]. However, the Kondo scattering at local magnetic moments can be excluded in our case as $Co_3Sn_{1.03}In_{0.97}S_2$ does not show a magnetic instability. Furthermore, the 2D localization scattering that occurs in disordered electronic systems, manifests itself in case of weak spin-orbit coupling as a positive correction to the resistivity at low temperatures, has been observed in a wide range of doping[186–188]. Here we found the logarithmic behavior in a very narrow region just below $x = 1.0$. Moreover, the interpretation in terms of weak localization and Kondo scattering requires the presence of a significant DOS(ε_F) which is not the case of $Co_3Sn_{1.03}In_{0.97}S_2$ as indicated below by the specific heat data.

The dramatic change of the susceptibility from Curie-Weiss-like behavior to Pauli paramagnetic one observed at $x = 1.00$[111] as well as the drastic change in the transport reported here suggests at least a topology change in the Fermi surface, i.e. Lifshitz transition[169]. However, the emergent almost T^3-dependence of $C_p(T)$ at low temperatures at $x \sim 1.0$ indicates not only modified but also drastically diminished Fermi surface. As no significant change was observed in the lattice structure[111,117,127], this anomalous nonmetallic state may originate from the Fermi energy tuning through a Dirac point in the electronic structure of $Co_3Sn_{2-x}In_xS_2$.

Simply due to the linear energy dispersion in DMs, one can consider the electronic specific heat, $C_{el}(T)$, of d-dimensional DM obeys the universal relation: $C_{el}/T \propto T^{d-1}$ at low temperatures, where d (or α in subsec. 3.2) varies from 2 to 3 for Dirac fermions of 2D and 3D character, respectively[191]. This means that both the electronic and phononic terms in $C_p(T)$ of 3D-DMs show simultaneously cubic dependence, while in 2D-DMs $C_{el}(T)$ shows a quadratic dependence at low temperatures. This universal and characteristic behavior for clean DMs only accounts for the band structure effects and can easily be masked by the T-dependent electron–electron interactions[191]. Recently, quadratic T-dependence of $C_p(T)$ at low T, suggesting massless Dirac dispersion, inthe multilayered α-(BEDT-TTF)2I3 was observed under pressure[192]. The specific heat of $x = 0.97$ exhibits $d = 2.44$ and that of $x = 1.0$ exhibits $d = 2.56$ at temperatures below 4 K, see table 7.1. A picture of massless Q-2D Dirac fermions in $Co_3Sn_{2-x}In_xS_2$ very close to $x = 1.0$ is suggested by the observed T-dependence of $C_p(T)$ at low temperatures. The low-energy Q-2D fermionic excitations around a nodal point in the electronic structure explains the high value of β at $x \sim 1.0$, estimated in subsec. 3.2.

Table 7.1: The electronic parameters: Somerfeld coefficient, γ; the phononic specific heat coefficient, β; Debye temperature, θ_D; the density of states at Fermi level, DOS(ε_F); the temperature exponent of $c_p(T)$, α; and the in- and out-of-plane scattering coefficient due to electron-electron interaction, A_{ab} and A_c; respectively, of $Co_3Sn_{2-x}In_xS_2$ obtained by analyzing the specific heat and electrical resistivity data.

x	γ (mJ.mol^{-1}.K^{-2})	β (mJ.mol^{-1}.K^{-4})	θ_D (K)	DOS(ε_F)×10^6 (eV^{-1} f.u.$^{-1}$)	α (below 4 K)	A_{ab}×10^{-6} (mΩ.cm/K^2)	A_c×10^{-5} (mΩ.cm/K^2)
0.00	9.8235	0.305	355	2.369	1.31	8.916	5.69
0.34	9.9445	0.608	282	2.398	1.55	6.967	2.10
0.65	31.94	0.459	310	7.702	1.15	90.78	-
0.84	35.423	0.257	375	8.542	1.05	148	150
0.93	28.828	0.70268	281	6.7	1.24	-	-
0.97	0.67638	2.3868	-	0.163	2.44	-	-
1.00	0.67355	1.3314	-	0.162	2.56	-	-
1.05	2.9145	0.25971	374	0.703	1.55	-	-
1.14	8.0496	0.289	361	1.941	1.40	10.16	88.7
1.52	25.599	0.359	336	6.173	1.15	11.24	66.7
2.00	44.5	0.534	300	8.258	1.14	0.701	23.3

As a 2D electron gas, 2D-DMs experience interactions effect that manifests itself as a decrease in conductivity with logarithmically decreasing of temperature[193–196]. We attribute the logarithmic divergence of the resistivity of x = 0.97 to electrons interactions effect that is dominant to a topological delocalization, which suppresses the resistivity. An unconventional nonmetallic ground states with logarithmic divergence of resistance at low temperatures has been recently observed in transport experiments on thin films of the topological insulators Bi_2Se_3 and Bi_2Te_3 and introduced as a signature of strong electron interaction effect that competes with the topological delocalization[194–196]. The interaction effect in $Co_3Sn_{2-x}In_xS_2$ can

be identified by transport measurements in sufficiently high magnetic fields as other effects which may also exhibit logarithmic temperature divergence such as weak localization or weak antilocalization are suppressed. Moreover, strong insulating tendency, indicated by the slope of $\rho(T)$ vs. log T and the temperature to which the logarithmic behavior extends, was observed in thinner films down to one quintuple layer of Bi_2Se_3 topological insulators[194]. In consistence with the observed large anisotropy in resistivity, the logarithmic divergence of $\rho(T)$ extending to high temperatures above 100 K indicates highly Q2D character of the electronic state in $Co_3Sn_{1.03}In_{0.97}S_2$.

The results of the normal Hall coefficient, R_0, presented previously in chapter 5, as well as the reported thermopower[83,127] introduced in subsect 1.4.4 of chapter 1, drastically change the sign around $x \sim 1.0$. Figure 7.8 shows the x-dependence of R_0 of $Co_3Sn_{2-x}In_xS_2$ and the corresponding charge-carriers density at 100 K. Fermi level tuning by In-substitution from the electron conduction band for low In concentrations to the hole conduction band at high In concentrations is clearly indicated. However, a discontinuous change to large positive Hall coefficient in a very narrow region $x \sim 1.0$ (R_0 diverges at $x \sim 0.97$ corresponding to a collapsed charge-carriers density as seen in the inset) indicates the anomalous electronic state.

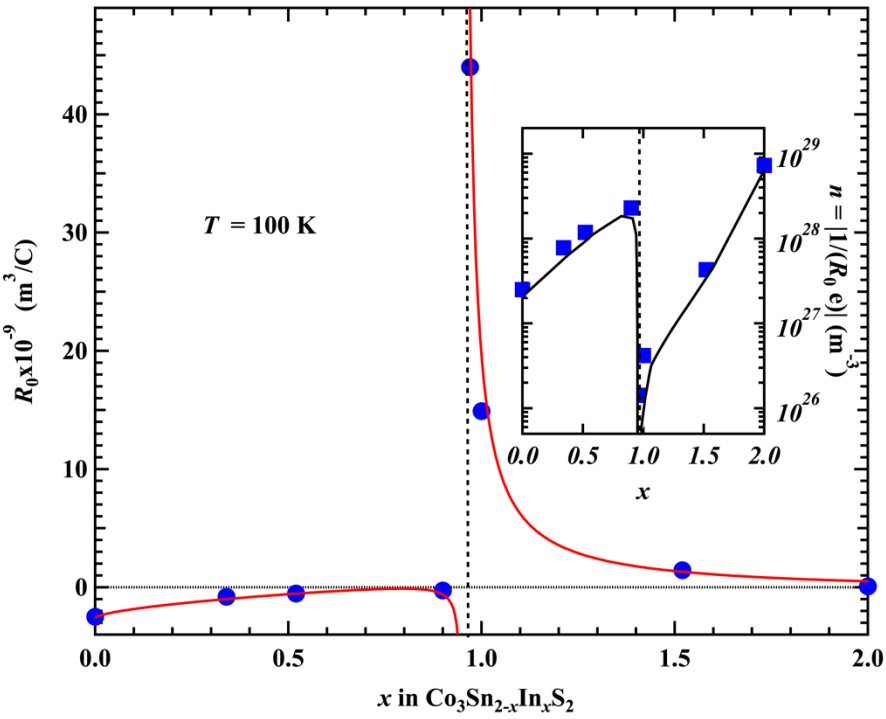

Figure 7.8: The In concentration dependence of the Hall coefficient R_0 of $Co_3Sn_{2-x}In_xS_2$ at 100 K. The inset shows the x-dependence of the charge carriers density in $Co_3Sn_{2-x}In_xS_2$. The solid lines are for the eye-guidance and dash horizontal line is the zero-base of R_0.

The observed transport and thermodynamic properties of $Co_3Sn_{2-x}In_xS_2$ suggest Dirac-cone dispersions in Co_3SnInS_2 semimetal that can be tuned by In-substitution. Figure 7.9 presents a schematic configuration of the suggested linear dispersion of energy in the *k*-space of massless Dirac fermions in the band structure of $Co_3Sn_{2-x}In_xS_2$ very close to $x \sim 1.0$, Fig. 7.9(a). The suggested Dirac cone picture is compared to a quadratic dispersion with the band gap that was theoretically predicted to open at ε_F for $x = 1.0$, Fig. 7.9(b). In view of the reported thermopower data[127], our results indicates Femi level tuning by In-substitution in barely touched conduction- and valance-bands of Dirac cone electronic structure. Spectroscopic evidence such as angle resolved photoemission and further magnetotransport measurements in high magnetic fields using single crystals should be conducted.

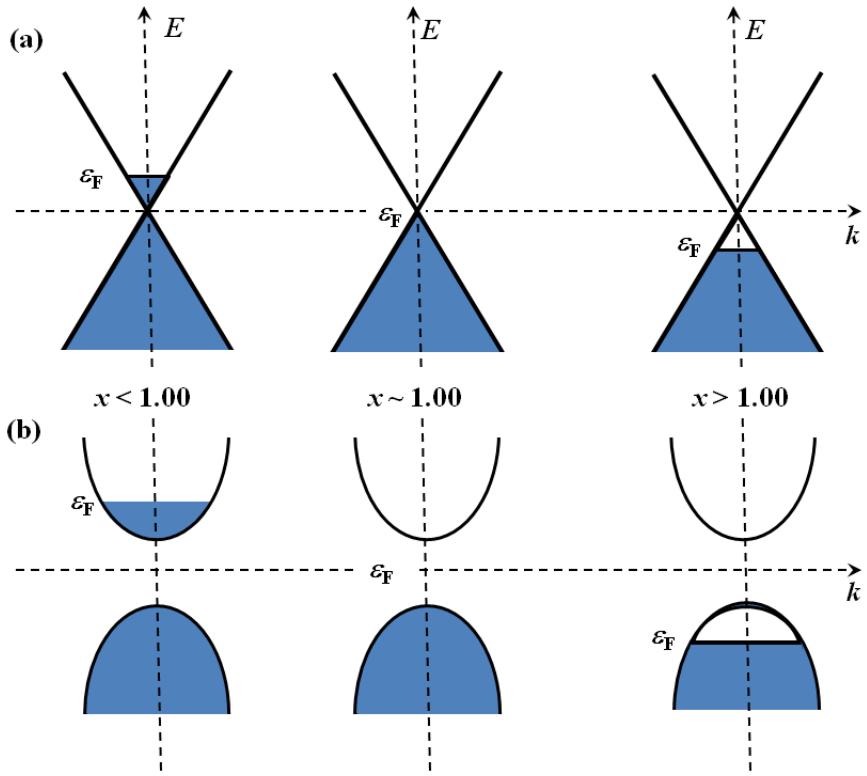

Figure 7.9: Schematic representation of the band structure of $Co_3Sn_{2-x}In_xS_2$ with $x < 1.00$, $x \sim 1.00$ and $x > 1.00$ in case of (a) the linear energy, *E*, dispersion in the wave number, *k*, space with massless Dirac fermions at $x \sim 1.00$ suggested by the experimentally observed transport properties, and in a case of (b) quadratic dispersion with the theoretically predicted gap that opens at the Fermi energy, ε_F, for $x = 1.00$.

7.5 Conclusion

The electronic properties of $Co_3Sn_{2-x}In_xS_2$ ($0.0 \leq x \leq 2.0$) were studied via the resistivity and heat capacity measurements using single crystals. In-substitution enhances the Q2D character of the electronic state of $Co_3Sn_{2-x}In_xS_2$, with anomalously drastic enhancement at $x \sim 1.0$, as clearly indicated by the enhanced anisotropy in the resistivity. An observed logarithmic divergence of resistivity of $x = 0.97$ as the temperature decreases indicates no band gap opens. The highly 2D-like nonmetallic ground state accompanied by the absence of linear T-dependence of the specific heat, and a strongly enhanced T^3-term instead, around $x \sim 1.0$ indicate an anomalous electronic state with small Fermi surface. The T-dependence of the specific heat at low temperatures suggests the emerge of low-energy massless Q2D Dirac fermions at $x \sim 1.0$.

CHAPTER 8

8 Concluding Remarks

Single crystals of Co-shandite solid solutions have been successfully grown by a flux-method and a modified Bridgeman technique. Using the flux-method, sufficiently large hexagonal plate-shaped single crystals (about 7 mm in zise and 1-2 mm in thickness) were obtained. $Co_3Sn_{2-x}In_xS_2$ ($0 < x \leq 2$) single crystals were grown out of stoichiometric Sn and In self-flux and/or Pb flux while $Co_{3-y}Fe_ySn_2S_2$ ($0 < y \leq 0.5$) crystals were grown out of the Sn self-flux. Much larger single crystals of $Co_3Sn_{2-x}In_xS_2$ (~ 5 cm in length and 1 cm in diameter) were grown by using a modified Bridgeman method of slow cooling of vacuum-sealed polycrystalline powders in a virtical temperature-gradient furnace. The shandite structure with $R\bar{3}m$ symmetry was confirmed by powder x-ray diffraction and the crystal structure parameters were refined by the Rietveld analysis. Wavelength-dispersive x-ray spectroscopy indicated the successful growth of $Co_3Sn_{2-x}In_xS_2$ in the whole range of x and the growth of $Co_{3-y}Fe_ySn_2S_2$ up to $y = 0.5$. The employed Laue x-ray camera to orient the crystals indicated high-quality crystals.

Comprehensive magnetization measurements were performed using the grown single crystals of Co-based shandites. In consistence with literature, $Co_3Sn_2S_2$ exhibits a ferromagnetic transition at Curie temperature T_C ~173 K with a large axial anisotropy. The ferromagnetic order is suppressed by In- and Fe-substitutions and the ferromagnetic-nonmagnetic quantum phase transition, quantum critical point (QCP), was found around x_c (y_c) ~ 0.8. The magnetic parameters of both systems; the Curie temperature T_C, effective moment p_{eff} and spontaneous moment p_s; exhibit almost identical variations against the In- and Fe-concentrations, indicating significance of the electron count on the magnetism in the Co-based shandite. Analysis based on the extended Q2D spin fluctuation theory clearly revealed the highly Q2D itinerant electron character of the magnetism of Co-based shandites. Furthermore, stirring anomalies for $0.5 \lesssim x < 0.8$ were solely observed in the *ab*-magnetization behavior, abruptly decreased magnetic anisotropy and cusp-like anomalies at 7 - 10 K, indicating spin canting.

A chiral spin state in the kagomé-lattice $Co_3Sn_{2-x}In_xS_2$ was observed in the vicinity of the QCP ($0.5 \lesssim x < 0.8$) through a combined work of the magnetization and magneto-transport measurements. A distinct positive topological Hall effect (THE) was observed at temperatures below 7 - 10 K and magnetic fields below 0.2 T. The observed chiral spin phase corresponds the anomalies observed in the *ab*-magnetization. Finite temperature Hall resistivity of topological nature and small negative contributions extending to Curie temperatures was also observed and attributed to chiral fluctuations of a magnetization-induced uniform chirality in a "para-chiral state" of $Co_3Sn_{2-x}In_xS_2$ ($0.5 \lesssim x < 0.8$).

Precise magnetization and ac susceptibility measurements at very low magnetic fields (below the saturating field of ~ 1kOe) showed anomalously indicative magnetic transitions just below T_C (130 K $\leq T \leq$ 172 K). We found anomalous magnetic transitions and slow magnetic response to the applied magnetic field in and perpendicular to the *c*-direction. Our results suggest competing magnetic orders and the emergence of non-coplanar magnetic orderings of possible vortex-like textures (skyrmions), due to the Dzyaloshinskii-Moriya interactions inherent in the geometrically frustrated Co-kagomé sublattice. The magnetization data shows preservation of these anomalies as well as the strong magnetic anisotropy in the ferromagnetic phase of $Co_3Sn_{2-x}In_xS_2$ and $Co_{3-y}Fe_ySn_2S_2$. The magnetic relaxation process studied in frequencies covering five orders of magnitude from 0.01 Hz to 1 kHz indicates characteristic relaxation times of several milliseconds at the boarders of a suggested skyrmion lattice A-phase. Based on these transitions, the magnetic phase diagrams of $Co_3Sn_2S_2$ with applied fields in different crystallographic directions were approached.

Exotically anisotropic transport properties of the layered shandites, $Co_3Sn_{2-x}In_xS_2$ ($0 \leq x \leq 2$) observed by resistivity and heat capacity measurements using single crystals were presented and discussed in details. Fermi level tuning by In-substitution, semimetallic behavior in a narrow *x*-region at $x \sim 1.0$, logarithmic divergence of resistivity of $x = 0.97$ as the temperature decreases and strongly enhanced T^3-term of the specific heat instead of the linear *T*-term of the specific heat at low temperatures, all indicate an unconventional electronic state with anomalously small Fermi surface very close to $x \sim 1.0$, i.e. linear dispersive electron state and an emergent Dirac electron state in this layered kagomé system. With a large additional enhancement in the anomalous semimetallic region, the observed increased anisotropy of the resistivity indicates an enhanced Q2D electronic state in $Co_3Sn_{2-x}In_xS_2$.

References:

[1] E.C. Stoner, Proc. R. Soc. A **165**, 372 (1938).

[2] P. Mohn, *Magnetism in the Solid State An Introduction* (Springer, Berlin, 2006).

[3] T. Moriya and A. Kawabata, J. Phys. Soc. Jpn. **34**, 639 (1973).

[4] T. Moriya and A. Kawabata, J. Phys. Soc. Jpn. **35**, 669 (1973).

[5] T. Moriya and Y. Takahashi, J. Phys. Soc. Jpn. **45**, 397 (1978).

[6] T. Moriya, *Spin Fluctuations in Itinerant Electron Magnetism* (Springer-Verlag, New York, 1985).

[7] Y. Takahashi, J. Phys. Soc. Jpn. **55**, 3553 (1986).

[8] Y. Takahashi, *Spin Fluctuation Theory of Itinerant Electron Magnetism* (Springer, Berlin, 2013).

[9] Y. Takahashi, J. Phys. Condens. Matter **9**, 10359 (1997).

[10] S. Sachdev, Science **288**, 475 (2000).

[11] R.E. Peierls, *Quantum Theory of Solids* (Oxford Univ. Press, London, 1955).

[12] F.L. Ning, K. Ahilan, T. Imai, A.S. Sefat, M.A. McGuire, B.C. Sales, D. Mandrus, P. Cheng, B. Shen, and H.-H. Wen, Phys. Rev. Lett. **104**, 37001 (2010).

[13] E. Dagotto, Rev. Mod. Phys. **66**, 763 (1994).

[14] C. de la Cruz, Q. Huang, J.W. Lynn, J. Li, W.R. Ii, J.L. Zarestky, H. a. Mook, G.F. Chen, J.L. Luo, N.L. Wang, and P. Dai, Nature **453**, 899 (2008).

[15] C.C. Torardi, M.A. Subramanian, J.C. Calabrese, J. Gopalakrishnan, K.J. Morrissey, T.R. Askew, R.B. Flippen, U. Chowdhry, and A.W. Sleight, Science **240**, 631 (1988).

[16] W.E. Pickett, Rev. Mod. Phys. **61**, 433 (1989).

[17] O. Stockert, H. v. Löhneysen, A. Rosch, N. Pyka, and M. Loewenhaupt, Phys. Rev. Lett. **80**, 5627 (1998).

[18] P. Gegenwart, Q. Si, and F. Steglich, Nat. Phys. **4**, 186 (2008).

[19] S. Kobayashi, H. Ueda, D. Nishio-Hamane, C. Michioka, and K. Yoshimura, Phys. Rev. B **89**, 54413 (2014).

[20] F.J. Di Salvo, D.E. Moncton, and J. V. Waszczak, Phys. Rev. B **14**, 4321 (1976).

[21] C.F. van Bruggen, R.J. Haange, G.A. Wiegers, and D.K.G. de Boer, Phys. B+C **99**, 166 (1980).

[22] K.S. Novoselov, A.K. Geim, S. V Morozov, D. Jiang, M.I. Katsnelson, I. V Grigorieva, and S. V Dubonos, Nature **438**, 197 (2005).

[23] Y. Zhang, Y.-W. Tan, H.L. Stormer, and P. Kim, Nature **438**, 201 (2005).

[24] A.H. Castro Neto, N.M.R. Peres, K.S. Novoselov, and A.K. Geim, Rev. Mod. Phys. **81**, 109 (2009).

[25] J.M.D. Coey, *Magnetism and Magnetic Materials* (Cambridge University Press, 2010).

[26] M. Shiga, K. Fujisawa, and H. Wada, J. Phys. Soc. Jpn. **62**, 1329 (1993).

[27] S. Kondo, D.C. Johnston, C.A. Swenson, F. Borsa, A. V. Mahajan, L.L. Miller, T. Gu, A.I. Goldman, M.B. Maple, D.A. Gajewski, E.J. Freeman, N.R. Dilley, R.P. Dickey, J. Merrin, K. Kojima, G.M. Luke, Y.J. Uemura, O. Chmaissem, and J.D. Jorgensen, Phys. Rev. Lett. **78**, 3729 (1997).

[28] T. Miyasato, N. Abe, T. Fujii, A. Asamitsu, S. Onoda, Y. Onose, N. Nagaosa, and Y. Tokura, Phys. Rev. Lett. **99**, 86602 (2007).

[29] I. Dzyaloshinsky, J. Phys. Chem. Solids **4**, 241 (1958).

[30] T. Moriya, Phys. Rev. **120**, 91 (1960).

[31] U.K. Rössler, A.N. Bogdanov, and C. Pfleiderer, Nature **442**, 797 (2006).

[32] N. Nagaosa and Y. Tokura, Nat. Nanotechnol. **8**, 899 (2013).

[33] N. Nagaosa, J. Sinova, S. Onoda, A.H. MacDonald, and N.P. Ong, Rev. Mod. Phys. **82**, 1539 (2010).

[34] Y. Tokura and S. Seki, Adv. Mater. **22**, 1554 (2010).

[35] A.P. Ramirez, in *Handb. Magn. Mater.*, Busch, K. (Elsevier Science, Amsterdam, 2001), pp. 423–520.

[36] J.T. Chalker, P.C.W. Holdsworth, and E.F. Shender, Phys. Rev. Lett. **68**, 855 (1992).

[37] S. Sachdev, Phys. Rev. B **45**, 12377 (1992).

[38] A.B. Harris, C. Kallin, and A.J. Berlinsky, Phys. Rev. B **45**, 2899 (1992).

[39] D. Grohol, K. Matan, J.-H. Cho, S.-H. Lee, J.W. Lynn, D.G. Nocera, and Y.S. Lee, Nat. Mater. **4**, 323 (2005).

[40] Y. Togawa, T. Koyama, K. Takayanagi, S. Mori, Y. Kousaka, J. Akimitsu, S. Nishihara, K. Inoue, A.S. Ovchinnikov, and J. Kishine, Phys. Rev. Lett. **108**, 107202 (2012).

[41] P.A. Lee, N. Nagaosa, and X.-G. Wen, Rev. Mod. Phys. **78**, 17 (2006).

[42] Y. Taguchi, Y. Oohara, H. Yoshizawa, N. Nagaosa, and Y. Tokura, Science **291**, 2573 (2001).

[43] Y. Machida, S. Nakatsuji, S. Onoda, T. Tayama, and T. Sakakibara, Nature **463**, 210 (2010).

[44] T. Taniguchi, K. Yamanaka, H. Sumioka, T. Yamazaki, Y. Tabata, and S. Kawarazaki, Phys. Rev. Lett. **93**, 246605 (2004).

[45] P. Pureur, F.W. Fabris, J. Schaf, and I.A. Campbell, Europhys. Lett. **67**, 123 (2004).

[46] J. Iwasaki, M. Mochizuki, and N. Nagaosa, Nat. Commun. **4**, 1463 (2013).

[47] S. Mühlbauer, B. Binz, F. Jonietz, C. Pfleiderer, A. Rosch, A. Neubauer, R. Georgii, and P. Böni, Science **323**, 915 (2009).

[48] W. Münzer, A. Neubauer, T. Adams, S. Mühlbauer, C. Franz, F. Jonietz, R. Georgii, P. Böni, B. Pedersen, M. Schmidt, A. Rosch, and C. Pfleiderer, Phys. Rev. B **81**, 1 (2010).

[49] X.Z. Yu, N. Kanazawa, Y. Onose, K. Kimoto, W.Z. Zhang, S. Ishiwata, Y. Matsui, and Y. Tokura, Nat. Mater. **10**, 106 (2011).

[50] S. Seki, X.Z. Yu, S. Ishiwata, and Y. Tokura, Science **336**, 198 (2012).

[51] Y. Tokunaga, X.Z. Yu, J.S. White, H.M. Rønnow, D. Morikawa, Y. Taguchi, and Y. Tokura, Nat. Commun. **6**, 7638 (2015).

[52] I. Kézsmárki, S. Bordács, P. Milde, E. Neuber, L.M. Eng, J.S. White, H.M. Rønnow, C.D. Dewhurst, M. Mochizuki, K. Yanai, H. Nakamura, D. Ehlers, V. Tsurkan, and A. Loidl, Nat. Mater. **14**, 1116 (2015).

[53] X. Yu, M. Mostovoy, Y. Tokunaga, W. Zhang, K. Kimoto, Y. Matsui, Y. Kaneko, N. Nagaosa, and Y. Tokura, Proc. Natl. Acad. Sci. **109**, 8856 (2012).

[54] X.Z. Yu, Y. Tokunaga, Y. Kaneko, W.Z. Zhang, K. Kimoto, Y. Matsui, Y. Taguchi, and Y. Tokura, Nat. Commun. **5**, 3198 (2014).

[55] W. Wang, Y. Zhang, G. Xu, L. Peng, B. Ding, Y. Wang, Z. Hou, X. Zhang, X. Li, E. Liu, S. Wang, J. Cai, F. Wang, J. Li, F. Hu, G. Wu, B. Shen, and X.X. Zhang, Adv. Mater. 6887 (2016).

[56] T. Okubo, S. Chung, and H. Kawamura, Phys. Rev. Lett. **108**, 17206 (2012).

[57] S. Heinze, K. von Bergmann, M. Menzel, J. Brede, A. Kubetzka, R. Wiesendanger, G. Bihlmayer,

and S. Blügel, Nat. Phys. **7**, 713 (2011).

[58] H. Weyl, Zeitschrift Fr Phys. Phys. **56**, 330 (1929).

[59] R. Suzuki, M. Sakano, Y.J. Zhang, R. Akashi, D. Morikawa, A. Harasawa, K. Yaji, K. Kuroda, K. Miyamoto, T. Okuda, K. Ishizaka, R. Arita, and Y. Iwasa, Nat. Nanotechnol. **9**, 611 (2014).

[60] D. Hsieh, D. Qian, L. Wray, Y. Xia, Y.S. Hor, R.J. Cava, and M.Z. Hasan, Nature **452**, 970 (2008).

[61] S. Tang and M.S. Dresselhaus, Nano Lett. **12**, 2021 (2012).

[62] Z. Wang, Y. Sun, X.-Q. Chen, C. Franchini, G. Xu, H. Weng, X. Dai, and Z. Fang, Phys. Rev. B **85**, 195320 (2012).

[63] S.M. Young, S. Zaheer, J.C.Y. Teo, C.L. Kane, E.J. Mele, and A.M. Rappe, Phys. Rev. Lett. **108**, 140405 (2012).

[64] Z. Wang, H. Weng, Q. Wu, X. Dai, and Z. Fang, Phys. Rev. B **88**, 125427 (2013).

[65] L.P. He, X.C. Hong, J.K. Dong, J. Pan, Z. Zhang, J. Zhang, and S.Y. Li, Phys. Rev. Lett. **113**, 1 (2014).

[66] J.A. Steinberg, S.M. Young, S. Zaheer, C.L. Kane, E.J. Mele, and A.M. Rappe, Phys. Rev. Lett. **112**, 36403 (2014).

[67] A.A. Abrikosov, Phys. Rev. B **58**, 2788 (1998).

[68] G.P. Mikitik and Y. V. Sharlai, Phys. Rev. Lett. **82**, 2147 (1999).

[69] L. Chen, S.-Q. Xia, and J.D. Corbett, Inorg. Chem. **44**, 3057 (2005).

[70] L. Chen and J.D. Corbett, Inorg. Chem. **41**, 2146 (2002).

[71] A. Simon, Angew. Chemie Int. Ed. English **20**, 1 (1981).

[72] A. Simon, Angew. Chemie Int. Ed. English **27**, 159 (1988).

[73] M.E. Fleet, Acta Crystallogr. Sect. C Cryst. Struct. Commun. **43**, 2255 (1987).

[74] F. Grønvold, A. Kjekshus, and F. Raaum, Acta Crystallogr. **14**, 930 (1961).

[75] L. Chen and J.D. Corbett, J. Am. Chem. Soc. **125**, 1170 (2003).

[76] P.A. Maggard and J.D. Corbett, J. Am. Chem. Soc. **122**, 838 (2000).

[77] A.I. Baranov, A.A. Isaeva, L. Kloo, and B.A. Popovkin, Inorg. Chem. **42**, 6667 (2003).

[78] P.S. Herle and J.D. Corbett, Inorg. Chem. **40**, 1858 (2001).

[79] B. Harbrecht and H.. Franzen, J. Less Common Met. **113**, 349 (1985).

[80] H. Xu, K.M. Kleinke, T. Holgate, H. Zhang, Z. Su, T.M. Tritt, and H. Kleinke, J. Appl. Phys. **105**, 53703 (2009).

[81] H. Zhang, J. He, B. Zhang, Z. Su, T.M. Tritt, N. Soheilnia, and H. Kleinke, J. Electron. Mater. **36**, 727 (2007).

[82] C.-S. Lee and H. Kleinke, Eur. J. Inorg. Chem. **2002**, 591 (2002).

[83] J. Corps, P. Vaqueiro, A. Aziz, R. Grau-Crespo, W. Kockelmann, J.-C. Jumas, and A. V. Powell, Chem. Mater. **27**, 3946 (2015).

[84] B. Li, Y. Xie, J. Huang, H. Su, and Y. Qian, J. Solid State Chem. **149**, 338 (2000).

[85] W.-Q. Hu, Y.-F. Shi, and L.-M. Wu, Cryst. Growth Des. **12**, 3458 (2012).

[86] B. Zhou, Y. Xing, S. Miao, M. Li, W.-H. Zhang, and C. Li, Chemistry **20**, 12426 (2014).

[87] S.H. Elder, S. Jobic, R. Brec, M. Gelabert, and F.J. DiSalvo, J. Alloys Compd. **235**, 135 (1996).

[88] P.A. Maggard and J.D. Corbett, Inorg. Chem. **39**, 4143 (2000).

[89] F. Meng and T. Hughbanks, Inorg. Chem. **40**, 2482 (2001).

[90] L. Chen and J.D. Corbett, Inorg. Chem. **43**, 3371 (2004).

[91] T.K. Reynolds, J.G. Bales, and F.J. DiSalvo, Chem. Mater. **14**, 4746 (2002).

[92] M. Zabel, S. Wandinger, K. Range, S. Prof, and D. Regensburg, Z. Naturforsch **34B**, 238 (1979).

[93] S. Natarajan, G.V.S. Rao, R. Baskaran, and T.S. Radhakrishnan, J. Less Common Met. **138**, 215 (1988).

[94] D.L. Scholtz, Trans. Geol. Soc. S. Africa **39**, 81 (1936).

[95] P. Ramdohr, Sitz. Berl. Akad. Wiss. Math.-Nat. Kl. VI **1**, (1949).

[96] R. Weihrich and I. Anusca, Z. Anorg. Allg. Chem. **632**, 335 (2006).

[97] E.Y. Zakharova, S.M. Kazakov, and A.N. Kuznetsov, J. Alloys Compd. **651**, 193 (2015).

[98] R. Weihrich, S.F. Matar, V. Eyert, F. Rau, M. Zabel, M. Andratschke, I. Anusca, and T. Bernert, Prog. Solid State Chem. **35**, 309 (2007).

[99] R. Weihrich, I. Anusca, and M. Zabel, Z. Anorg. Allg. Chem. **631**, 1463 (2005).

[100] R. Weihrich, I. Anusca, and M. Zabel, Z. Anorg. Allg. Chem. **630**, 1767 (2004).

[101] R. Weihrich and I. Anusca, Z. Anorg. Allg. Chem. **632**, 1531 (2006).

[102] K.-P. Martens and R. Hoppe, Zeitschrift Für Anorg. Und Allg. Chemier Anorg. Und Allg. Chemier Anorg. Und Allg. Chemie **437**, 116 (1977).

[103] R.M. Braun and R. Hoppe, Angew. Chemie **90**, 475 (1978).

[104] R. Hoppe and B. Nowitzki, Zeitschrift Für Anorg. Und Allg. Chemier Anorg. Und Allg. Chemie **509**, 145 (1984).

[105] S. Seidlmayer, F. Bachhuber, I. Anusca, J. Rothballer, M. Bräu, P. Peter, and R. Weihrich, Zeitschrift Für Krist. **225**, 371 (2010).

[106] R. Weihrich, S.F. Matar, I. Anusca, F. Pielnhofer, P. Peter, F. Bachhuber, and V. Eyert, J. Solid State Chem. **184**, 797 (2011).

[107] T. Sakamoto, M. Wakeshima, and Y. Hinatsu, J. Phys. Condens. Matter **18**, 4417 (2006).

[108] T. Sakamoto, M. Wakeshima, Y. Hinatsu, and K. Matsuhira, Phys. Rev. B **75**, 60 (2007).

[109] T. Sakamoto, M. Wakeshima, Y. Hinatsu, and K. Matsuhira, Phys. Rev. B **78**, 2 (2008).

[110] K. Momma and F. Izumi, J. Appl. Crystallogr. **41**, 653 (2008).

[111] M.A. Kassem, Y. Tabata, T. Waki, and H. Nakamura, J. Cryst. Growth **426**, 208 (2015).

[112] M.A. Kassem, Y. Tabata, T. Waki, and H. Nakamura, J. Solid State Chem. **233**, 8 (2016).

[113] M.A. Kassem, Y. Tabata, T. Waki, and H. Nakamura, J. Phys. Soc. Jpn. **85**, 64706 (2016).

[114] J. Rothballer, F. Bachhuber, F. Pielnhofer, F.M. Schappacher, R. Pöttgen, and R. Weihrich, Eur. J. Inorg. Chem. **2013**, 248 (2013).

[115] A. Umetani, E. Nagoshi, T. Kubodera, and M. Matoba, Phys. B Condens. Matter **403**, 1356 (2008).

[116] M. Fujioka, T. Shibuya, J. Nakai, K. Yoshiyasu, Y. Sakai, Y. Takano, Y. Kamihara, and M. Matoba, Solid State Commun. **199**, 56 (2014).

[117] F. Pielnhofer, J. Rothballer, P. Peter, W. Yan, F.M. Schappacher, R. Pöttgen, and R. Weihrich, Z. Anorg. Allg. Chem. **640**, 286 (2014).

[118] X. Lin, S.L. Bud'ko, and P.C. Canfield, Philos. Mag. **92**, 2436 (2012).

[119] W. Schnelle, A. Leithe-Jasper, H. Rosner, F.M. Schappacher, R. Pöttgen, F. Pielnhofer, and R.

Weihrich, Phys. Rev. B **88**, 144404 (2013).

[120] M. Holder, Y. Dedkov, A. Kade, H. Rosner, W. Schnelle, A. Leithe-Jasper, R. Weihrich, and S.L. Molodtsov, Phys. Rev. B **79**, 205116 (2009).

[121] J.M.D. Coey and S. Sanvito, J. Phys. D. Appl. Phys. **37**, 988 (2004).

[122] T. Kubodera, H. Okabe, Y. Kamihara, and M. Matoba, Phys. B Condens. Matter **378–380**, 1142 (2006).

[123] Y. Sakai, R. Tanakadate, M. Matoba, I. Yamada, and N. Nishiyama, J. Phys. Soc. Jpn. **84**, 44705 (2015).

[124] Y. Sakai, Y. Kamihara, and M. Matoba, Phys. Status Solidi **10**, 1130 (2013).

[125] R. Weihrich, W. Yan, J. Rothballer, P. Peter, S.M. Rommel, S. Haumann, F. Winter, C. Schwickert, and R. Poettgen, Dalt. Trans. **44**, 15855 (2015).

[126] F. Pielnhofer, A.S. Tragl, J. Rothballer, and R. Weihrich, Z. Naturforsch. **69B**, 55 (2014).

[127] J. Corps, P. Vaqueiro, and A. V. Powell, J. Mater. Chem. A **1**, 6553 (2013).

[128] Z. Fisk and J.P. Remeika, in *Handb. Phys. Chem. Rare Earths. Vol. 12*, edited by L. Gschneidner Jr, K.A. and Eyring (Elsevier, Amsterdam, 1989), pp. 53–70.

[129] Z. Canfield, Paul C. and Fisk, Philos. Mag. B **65**, 1117 (1992).

[130] P.C. Canfield and I.R. Fisher, J. Cryst. Growth **225**, 155 (2001).

[131] M.G. Kanatzidis, R. Pöttgen, and W. Jeitschko, Angew. Chemie - Int. Ed. **44**, 6996 (2005).

[132] P.C. Canfield, in *Prop. Appl. Complex Intermet.*, edited by E. Belin-Ferré (World Scientific, Singapore, 2010), pp. 93–111.

[133] R. Brower, W.; Praker, H.; Roth, Am. Miner. **59**, 296 (1974).

[134] I. Anusca, A. Schmid, P. Peter, J. Rothballer, F. Pielnhofer, and R. Weihrich, Z. Anorg. Allg. Chem. **635**, 2410 (2009).

[135] T.B. Massalski, H. Okamoto, and P.R. Subramanian, *Binary Alloy Phase Diagrams*, 2nd ed. (ASM International, Materials Park, OH, USA, 1990).

[136] L. Liu, C. Andersson, and J. Liu, J. Electron. Mater. **33**, 935 (2004).

[137] K. Izumi, F.; Momma, Solid State Phenom. **130**, 15 (2007).

[138] Bruker AXS (2008): TOPAS V4:, (n.d.).

[139] A.B. Greilinger, Zeitschrift Für Krist. - Cryst. Mater. **91**, (1935).

[140] L.J. van der Pauw, Philips Tech. Rev. **20**, 220 (1958).

[141] C.A.M. Dos Santos, A. De Campos, M.S. Da Luz, B.D. White, J.J. Neumeier, B.S. De Lima, and C.Y. Shigue, J. Appl. Phys. **110**, (2011).

[142] J. Rothballer, F. Bachhuber, S.M. Rommel, T. Söhnel, and R. Weihrich, RSC Adv. **4**, 42183 (2014).

[143] A. Arrott, Phys. Rev. **108**, 1394 (1957).

[144] K. Yoshimura, M. Takigawa, Y. Takahashi, H. Yasuoka, and Y. Nakamura, J. Phys. Soc. Jpn. **56**, 1138 (1987).

[145] K. Shimizu, H. Maruyama, H. Yamazaki, and H. Watanabe, J. Phys. Soc. Jpn. **59**, 305 (1990).

[146] Z. Liu, T. Waki, Y. Tabata, and H. Nakamura, Phys. Rev. B **89**, 54435 (2014).

[147] H. Ohta, D. Noguchi, K. Nabetani, and H.A. Katori, Phys. Rev. B **88**, 94441 (2013).

[148] H. Ohta and K. Yoshimura, Phys. Rev. B **79**, 184407 (2009).

[149] B. Chen, J. Yang, H. Wang, M. Imai, H. Ohta, C. Michioka, K. Yoshimura, and M. Fang, J. Phys. Soc. Jpn. **82**, 124711 (2013).

[150] C. Pappas, Physics (College. Park. Md). **5**, 28 (2012).

[151] G. Tatara and H. Kawamura, J. Phys. Soc. Jpn. **71**, 2613 (2002).

[152] K. Ueda, S. Iguchi, T. Suzuki, S. Ishiwata, Y. Taguchi, and Y. Tokura, Phys. Rev. Lett. **108**, 2 (2012).

[153] C. Sürgers, G. Fischer, P. Winkel, and H. V Löhneysen, Nat. Commun. **5**, 3400 (2014).

[154] J. Ye, Y.B. Kim, A.J. Millis, B.I. Shraiman, P. Majumdar, and Z. Teˇ, Phys. Rev. Lett. **83**, 3737 (1999).

[155] S.H. Chun, M.B. Salamon, P.M. Goldbart, and P.D. Han, Phys. Rev. Lett. **84**, 757 (2000).

[156] Y. Lyanda-Geller, S.H. Chun, M.B. Salamon, P.M. Goldbart, P.D. Han, Y. Tomioka, A. Asamitsu, and Y. Tokura, Phys. Rev. B **63**, 184426 (2001).

[157] H. Nakamura, R. Ikeno, G. Motoyama, T. Kohara, Y. Kajinami, and Y. Tabata, J. Phys. Conf. Ser. **145**, 12077 (2009).

[158] I. Levatić, V. Šurija, H. Berger, and I. Živković, Phys. Rev. B **90**, 1 (2014).

[159] F. Qian, H. Wilhelm, A. Aqeel, T.T.M. Palstra, A.J.E. Lefering, E.H. Brück, and C. Pappas, Phys. Rev. B **94**, 64418 (2016).

[160] A. Bauer and C. Pfleiderer, Phys. Rev. B **85**, 1 (2012).

[161] L.J. Bannenberg, A.L.E. Lefering, K. Kakerai, Y. Onose, Y. Endoh, Y. Tokura, and C. Pappas, arXiv:1608.00404 [Cond-Mat.mtrl-Sci] (2016).

[162] R. Viennois, C. Reibel, D. Ravot, R. Debord, and S. Pailhès, EPL **111**, 17008 (2015).

[163] M. Bałanda, Acta Phys. Pol. A **124**, 964 (2013).

[164] K.S. Cole and R.H. Cole, J. Chem. Phys. **9**, 341 (1941).

[165] C. Dekker, A.F.M. Arts, H.W. de Wijn, A.J. van Duyneveldt, and J.A. Mydosh, Phys. Rev. B **40**, 11243 (1989).

[166] K. Karube, J.S. White, N. Reynolds, J.L. Gavilano, H. Oike, A. Kikkawa, F. Kagawa, Y. Tokunaga, H.M. Rønnow, Y. Tokura, and Y. Taguchi, Nat. Mater. **15**, 1237 (2016).

[167] Y. Li, N. Kanazawa, X.Z. Yu, A. Tsukazaki, M. Kawasaki, M. Ichikawa, X.F. Jin, F. Kagawa, and Y. Tokura, Phys. Rev. Lett. **110**, 1 (2013).

[168] P. Delhaes and M. Drillon, editors , *Organic and Inorganic Low-Dimensional Crystalline Materials* (Springer US, Boston, MA, 1988).

[169] Y. Okamoto, A. Nishio, and Z. Hiroi, Phys. Rev. B **81**, 121102 R (2010).

[170] K. Chen, Z.Y. Meng, T. Pruschke, J. Moreno, and M. Jarrell, Phys. Rev. B **165136**, 1 (2012).

[171] Y. Lemonik, I.L. Aleiner, and C. Toke, Phys. Rev. B **82**, 201408_R_ (2010).

[172] C. Liu, T. Kondo, R.M. Fernandes, A.D. Palczewski, E.D. Mun, N. Ni, A.N. Thaler, A. Bostwick, E. Rotenberg, J. Schmalian, S.L. Bud, P.C. Canfield, and A. Kaminski, Nat. Phys. **6**, 419 (2010).

[173] H. Masuda, H. Sakai, M. Tokunaga, Y. Yamasaki, A. Miyake, J. Shiogai, S. Nakamura, S. Awaji, A. Tsukazaki, H. Nakao, Y. Murakami, T. -h. Arima, Y. Tokura, and S. Ishiwata, Sci. Adv. **2**, e1501117 (2016).

[174] S. Borisenko, D. Evtushinsky, Q. Gibson, A. Yaresko, T. Kim, M.N. Ali, B. Buechner, M. Hoesch, and R.J. Cava, (2015).

[175] Y.-Y. Wang, Q.-H. Yu, and T.-L. Xia, 4 (2016).

[176] A.P. Gonçalves, I.C. Santos, E.B. Lopes, R.T. Henriques, M. Almeida, and M.O. Figueiredo, Phys. Rev. B **37**, 7476 (1988).

[177] Y. Tokura, Y. Taguchi, Y. Okada, Y. Fujishima, T. Arima, K. Kumagai, and Y. Iye, Phys. Rev. Lett. **70**, 2126 (1993).

[178] H. Yoshino, K. Murata, T. Nakanishi, L. Li, E.S. Choi, D. Graf, J.S. Brooks, Y. Nogami, and G.C. Papavassiliou, J. Phys. Soc. Jpn. **74**, 417 (2005).

[179] H. Aizawa, K. Kuroki, H. Yoshino, and K. Murata, Phys. B Condens. Matter **405**, S27 (2010).

[180] P. Richard, K. Nakayama, T. Sato, M. Neupane, Y.M. Xu, J.H. Bowen, G.F. Chen, J.L. Luo, N.L. Wang, X. Dai, Z. Fang, H. Ding, and T. Takahashi, Phys. Rev. Lett. **104**, 2 (2010).

[181] J. Kim, S.S. Baik, S.H. Ryu, Y. Sohn, S. Park, B.-G. Park, J. Denlinger, Y. Yi, H.J. Choi, and K.S. Kim, Science **349**, 723 (2015).

[182] S.S. Baik, K.S. Kim, Y. Yi, and H.J. Choi, Nano Lett. **15**, 7788 (2015).

[183] K. Yamada, Prog. Theor. Phys. **53**, (1975).

[184] P.A. Lee, T.M. Rice, J. W.Serene, L.J. Sham, and J.W. Wilkins, Comm. Cond. Matt. Phys. **12**, 99 (1986).

[185] K. Wang, H. Ryu, E. Kampert, M. Uhlarz, J. Warren, J. Wosnitza, and C. Petrovic, Phys. Rev. X **4**, 1 (2014).

[186] Y. Ando, G. Boebinger, A. Passner, T. Kimura, and K. Kishio, Phys. Rev. Lett. **75**, 4662 (1995).

[187] Y. Ando, G.S. Boebinger, A. Passner, N.L. Wang, C. Geibel, F. Steglich, I.E. Trofimov, and F.F. Balakirev, Phys. Rev. B **56**, 4 (1997).

[188] J.N. Huiberts, R. Griessen, R.J. Wijngaarden, M. Kremers, and C. Van Haesendonck, Phys. Rev. Lett. **79**, 3724 (1997).

[189] T. Ando, A.B. Fowler, and F. Stern, Rev. Mod. Phys. **54**, 437 (1982).

[190] G. Gruner and A. Zawadowski, Reports Prog. Phys. **37**, 1497 (1974).

[191] T.O. Wehling, A.M. Black-Schaffer, and A.V. Balatsky, Adv. Phys. **63**, 1 (2014).

[192] T. Konoike, K. Uchida, and T. Osada, J. Phys. Soc. Jpn. **81**, 2 (2012).

[193] M. Kontani, H. Ido, H. Ando, T. Nishioka, and Y. Yamaguchi, J. Phys. Soc. Jpn. **63**, 1652 (1994).

[194] M. Liu, C.Z. Chang, Z. Zhang, Y. Zhang, W. Ruan, K. He, L.L. Wang, X. Chen, J.F. Jia, S.C. Zhang, Q.K. Xue, X. Ma, and Y. Wang, Phys. Rev. B **83**, 1 (2011).

[195] A.A. Taskin, S. Sasaki, K. Segawa, and Y. Ando, Phys. Rev. Lett. **109**, 1 (2012).

[196] H.C. Liu, H.Z. Lu, H.T. He, B. Li, S.G. Liu, Q.L. He, G. Wang, I.K. Sou, S.Q. Shen, and J. Wang, ACS Nano **8**, 9616 (2014).

List of publications

1- M. A. Kassem, Y. Tabata, T. Waki and H. Nakamura, **"**Single crystal growth and characterization of kagomé-lattice shandites $Co_3Sn_{2-x}In_xS_2$ **"**, ***J. Cryst. Growth*. 426**, 208 **(2015);**

2- M. A. Kassem Y. Tabata, T. Waki and H. Nakamura, "Structure and magnetic properties of flux grown single crystals of $Co_{3-x}Fe_xSn_2S_2$ shandites", ***J. Solid State Chem.* 233**, 8 **(2016);**

3- M. A. Kassem Y. Tabata, T. Waki and H. Nakamura, "Quasi-two-dimensional magnetism in Co-based shandites", ***J. phys. Soc.* Jpn. 85,** 064706 **(2016);**

4- M. A. Kassem, Y. Tabata, T. Waki and H. Nakamura, "Low-field magnetic phase diagram of $Co_3Sn_2S_2$ inferred from magnetization and ac susceptibility", to be submitted to **PRB**;

5- M.A. Kassem, K. Itou, Y. Tabata, T. Waki and H. Nakamura, "Chirality-driven Hall effect in a 2D-kagomé itinerant-electron ferromagnet", to be submitted to **PRL;**

6- M. A. Kassem, Y. Tabata, T. Waki, C. Michioka, K. Yoshimura and H. Nakamura, **"**Emergent unconventional quasi-two-dimensional electronic state in $Co_3Sn_{2-x}In_xS_2$", to be submitted**;**

7- M. A. Kassem, Y. Tabata, T. Waki and H. Nakamura, "Magneto-transport properties of $Co_{3-x}Fe_xSn_2S_2$ frustrated magnets", in preparation;

8- M. A. Kassem, Y. Tabata, T. Waki and H. Nakamura, "Structure, magnetic and transport properties of $Co_3Sn_{2-x}In_xS_2$ single crystals grown by a modified Bridgman method", in preparation;

Additional

9- M. A. Kassem, Y. Tabata, T. Waki and H. Nakamura, **"**Drastic effect of the Mn-substitution in the strongly correlated semiconductor $FeSb_2$**",** to appear in ***J. Phys. Conf. Ser.***

Conferences

1. M. A. Kassem, Y. Tabata, T. Waki and H. Nakamura, "Crystal Structure and Anisotropic Properties of Flux Grown $Co_3Sn_{2-x}In_xS_2$ Shandites", **poster** in **NASSCC 2015, Tallahassee, USA**;
2. **K. Itou**, M. A. Kassem, Y. Tabata, T. Waki, H. Nakamura, "Anomalous Hall effect in kagomé lattice magnet $Co_3Sn_{2-x}In_xS_2$", **oral** presentation in **JPS Fall 2015 meeting, Japan**;
3. M. A. Kassem, Y. Tabata, T. Waki, C. Michioka, K. Yoshimura and H. Nakamura, "Anomalous quasi-two-dimensional electronic state in $Co_3Sn_{2-x}In_xS_2$ shandites", **poster** in **LEES 2016, Shiga Biwaku, Japan**;
4. M. A. Kassem, K. Itou, Y. Tabata, T. Waki, C. Michioka, K. Yoshimura and H. Nakamura, "Emergent chiral spin structure and unconventional electronic states in the stacked-kagomé-layered $Co_3Sn_{2-x}In_xS_2$ shandites.", **oral** presentation in **SPSSM 2016, Nantes, France**;
5. M. A. Kassem, K. Itou, Y. Tabata, T. Waki and H. Nakamura, "Topological Hall effect in an itinerant-electron kagomé ferromagnet", **poster** in **HFM 2016, Taipei, Taiwan**.